

12-2018

# Damage Analysis of Aluminum Structure Repaired with A Composite Patch

Bozhi Heng

*University of Tennessee*, [bheng1@vols.utk.edu](mailto:bheng1@vols.utk.edu)

---

## Recommended Citation

Heng, Bozhi, "Damage Analysis of Aluminum Structure Repaired with A Composite Patch. " PhD diss., University of Tennessee, 2018.  
[https://trace.tennessee.edu/utk\\_graddiss/5306](https://trace.tennessee.edu/utk_graddiss/5306)

This Dissertation is brought to you for free and open access by the Graduate School at Trace: Tennessee Research and Creative Exchange. It has been accepted for inclusion in Doctoral Dissertations by an authorized administrator of Trace: Tennessee Research and Creative Exchange. For more information, please contact [trace@utk.edu](mailto:trace@utk.edu).

To the Graduate Council:

I am submitting herewith a dissertation written by Bozhi Heng entitled "Damage Analysis of Aluminum Structure Repaired with A Composite Patch." I have examined the final electronic copy of this dissertation for form and content and recommend that it be accepted in partial fulfillment of the requirements for the degree of Doctor of Philosophy, with a major in Mechanical Engineering.

Stephanie TerMaath, Major Professor

We have read this dissertation and recommend its acceptance:

Reza Abedi, Madhu S. Madhukar, Russell Zaretski

Accepted for the Council:

Carolyn R. Hodges

Vice Provost and Dean of the Graduate School

(Original signatures are on file with official student records.)

---

# **Damage Analysis of Aluminum Structure Repaired with A Composite Patch**

A Dissertation Presented for the  
Doctor of Philosophy  
Degree  
The University of Tennessee, Knoxville

Bozhi Heng  
December 2018

Copyright © 2018 by Bozhi Heng  
All rights reserved.

## ACKNOWLEDGMENTS

I would like to extend my sincerest thanks to my mentor, Dr. Stephanie TerMaath, for her continuously academically and financially support of my Ph.D. study, as well as for her patience, encouragement, and inspiration. Dr. TerMaath has guided me in molding my technical, research, and personal skills that would benefit my entire life. She has also provided me with many valuable opportunities and wise advice helping me developing in the career. I am forever grateful to her for her mentorship during those years and honored to be her first Ph.D. student.

I would also like to thank my committee members Dr. Reza Abedi, Dr. Madhu Madhukar and Dr. Russell Zaretski for the respected and highly regarded input towards this dissertation. I am grateful to Dr. Michael Shields and Dr. Jiaxin Zhang from Johns Hopkins University for their help with the sensitivity analysis. My sincere thanks to Dr. Daniel Hart from Naval Surface Warfare Center for his support on the composite patch fabrication and aluminum fracture testing. I am grateful to Dr. Lonnie Crosby from Oak Ridge National Lab (ORNL) for sharing his profound knowledge in material science. I would like to thank Dr. Uday Vaidya for sharing the composite lab space at the advanced Manufacture Demonstration Facilities (MDF). I appreciate my great friends, Mr. Douglas Fielden of Mechanical Systems Group, Mr. David Nuttall and Mr. Dylan Talley from ORNL, Mr. Stephen Sheriff from the Fibers and Composites Manufacturing

Facility, and all the staff of MABE department at UT for their valuable help in the past three years.

I feel lucky to get the chance to work with the senior researchers, Dr. Xianfeng Ma, Dr. Jason Clement, and Dr. Rajendra Timilsina, in our group for the past years. Their outstanding knowledge and great scientific enthusiasm inspired me in pursuing a professional career. I would also like to thank the graduate students in our group for constantly helping me and sharing happiness. They are Sofy Weisenberg, Elijah Stevens, Nathan Phelps, William Ferrell, Corey Arndt, Zach Bingham, and Kurt Smith.

## ABSTRACT

The interest in the application of high strength aluminum alloy in marine structures has been increasing in recent years due to its high strength-weight ratio and excellent corrosion resistance. However, those marine grade aluminum alloy unavoidably experience fatigue and stress corrosion cracking during their service life. Developing a reliable repair method is essential to address the damage problems. The composite patch has been demonstrated as a promising method to repair the damaged or reinforce the under-designed aluminum structures. This research focuses on creating a comprehensive understanding of damage mechanisms involved in the composite patch repaired structures. The compact tension testing of aluminum, four-point bend and fracture testing of composite repaired structures are employed to investigate the yielding and cracking in aluminum, fiber breakage, matrix cracking and delamination in the composite patch, and disbond of the bond line. The validated, high-fidelity 3D finite elements are developed to simulate those damage mechanisms. The sensitivity analysis coupling with the finite element simulations is then performed to study the effects of different damage modes and their interactions on the ability of the composite to restore the load capability of repaired structures. The most and least important factors affecting different damage modes are identified

to reduce the design space, which enables the improvement of the design efficiency of the composite patch.



# TABLE OF CONTENTS

Chapter I	Introduction .....	1
1.1	Cracking in Marine Aluminum Structure.....	1
1.2	Composite Repairing Method .....	3
1.3	Optimization of the Composite Patch.....	6
1.4	Objectives .....	13
Chapter II	Effect of Uncertainties on Numerical Prediction of Crack Propagation.....	17
2.1	Introduction .....	17
2.2	Experimental Work.....	19
2.3	Finite Element Analysis.....	23
2.4	Sensitivity Study.....	37
2.5	Results and Discussion.....	42
2.6	Conclusion .....	44
Chapter III	Progressive Damage in Composite.....	50
3.1	Introduction .....	50
3.2	Technical Approach .....	54
3.2.1	Experimental Testing .....	54
3.2.2	Finite Element Modeling .....	60
3.2.3	Sensitivity Analysis .....	69

3.3	Results and Discussions.....	77
3.3.1	Comparison Between Experimental Results and Computational Simulation.....	77
3.3.2	Distribution of the Energy Absorption .....	79
3.3.3	Sensitivity Analysis Results .....	84
3.4	Summary and Conclusion.....	92
Chapter IV	Crack propagation in Patched Structure .....	93
4.1	Introduction .....	93
4.2	Experimental Procedure .....	94
4.2.1	Materials .....	94
4.2.2	Testing Specimens .....	95
4.2.3	Testing Procedure .....	99
4.3	Results and Discussions.....	99
4.4	Conclusions .....	105
Chapter V	Conclusions and Future Work.....	109
5.1	Conclusions .....	109
5.2	Future Work.....	111
	List of References .....	113
	Vita.....	124

## LIST OF TABLES

Table 2. 1 Elastic and plastic properties of Al5456 .....	21
Table 2. 2 Geometry parameters and testing results of different CT specimens	21
Table 2. 3 Geometry parameters and testing results of different CT specimens, the value of different element size refers to Fig. 2.11 and 2.12. ....	35
Table 2. 4 The parameters of different assumed normal distributions assigned to the inputs, $\mu$ is the mean and $\sigma$ is the standard deviation.....	40
Table 2. 5 The effect of different parameters on the distribution of the output. ...	47
Table 3. 1 The data quality of the main parameters included in the FE model ...	74
Table 3. 2 The values of the FE model parameters considered in the sensitivity analysis.....	74
Table 3. 3 The ten most influential parameters for different damage mechanisms .....	88
Table 4. 1 Elastic and plastic properties of Al5456 (provided by the United States Naval Academy) .....	96
Table 4. 2 Mechanical properties of the E-glass/epoxy composite patch.....	98

## LIST OF FIGURES

Figure 1. 1 Examples of cracking in marine aluminum structures, a and b) fatigue cracking detected in the deck of a Royal Australian Navy frigate [3], c and d) stress corrosion cracking in US Navy vessels [4, 5]. .....	2
Figure 1. 2 Composite patches installed on marine aluminum structures [3, 4]. ...	4
Figure 1. 3 Cracked metal structure repaired with composite patches.....	7
Figure 1. 4 Comparison of the mode I and mode II SIF between the patch and unpatched crack in the mixed model [17]. .....	7
Figure 1. 5 The effect of adhesive thickness on the stress intensity factor on the repaired crack [20]. .....	9
Figure 1. 6 The stress intensity factor of crack repaired with composite patches with different shapes varies with the crack length in the repaired plate. ....	11
Figure 1. 7 Effect of the number of layers on fatigue life of repaired thin and thick plate [24]. .....	12
Figure 1. 8 Performance of composite patch with different fiber orientations, the crack is along the x-direction. ....	12
Figure 2. 1. The stress-strain curve is averaged from the tension testing results. ....	21
Figure 2. 2 Configurations of four CT specimens.....	22
Figure 2. 3 Crack surface of four CT testing specimens. ....	24

Figure 2. 4 The bilinear traction separation cohesive law. ....	26
Figure 2. 5 Mesh refinement at the crack tip and the roots of the side grooves in the XFEM model. ....	29
Figure 2. 6 The comparison of load-CMOD curves for specimen_1 obtained from experiment and different FE models. ....	29
Figure 2. 7 Comparison of load-CMOD curves from experimental and simulation results. ....	31
Figure 2. 8 The effect of the $n$ (plastic behavior) of aluminum on the load-CMOD curves. ....	31
Figure 2. 9 Comparison of the crack extension from experiments and simulations. The red elements in the crack surface of the XFEM model mean the elements are completely cracked. The light blue and green elements are partially cracked. The dark blue elements do not experience any crack. ....	34
Figure 2. 10 Crack surface of models with different mesh size and fixed aspect ratio of elements. The red elements above the red dash line represent the fully cracked area and the green and light blue elements between the red dash and light blue dash-dot line represent the partially cracked area. ....	34
Figure 2. 11 Load-CMOD Curves calculated from models with different size of cubelike elements. ....	35
Figure 2. 12 Load-CMOD curves calculated from models varying mesh size in different directions. ....	36

Figure 2. 13 Sobol indices of thirteen parameters including the material properties, geometry parameters, and damage modeling parameters. ....	45
Figure 2. 14 The normal distributions of the maximum load for different inputs distributions.....	46
Figure 3. 1 The three main challenges to evaluate the damage tolerance of structures repaired with composite patches and to identify the most influential parameters. ....	53
Figure 3. 2 The proposed approach integrates numerical modeling, experimental testing, and sensitivity analysis to produce validated numerical models and identify the most influential inputs based on the given model. ....	55
Figure 3. 3 Stacking sequence of E-glass/epoxy composite patch. ....	57
Figure 3. 4 Four different specimen configurations of the four-point bending test, all dimensions are in inches.....	59
Figure 3. 5 The laminae, the cohesive layers, the interface, and the aluminum are modeled individually in the finite element model of the patched structure. ..	61
Figure 3. 6 Damage variables used to model degradation of fabric reinforced laminae under different loading.....	65
Figure 3. 7 Triangular traction-separation law of the CZM.....	68

Figure 3. 8 Damage propagation of four-point bending specimens recorded with DIC, the white box indicates damage area and the corresponding simulation results at failure .....80

Figure 3. 9 Comparison between the displacement-load curve from simulation and experimental test for different specimen configurations.....81

Figure 3. 10 The final energy absorption distribution calculated from the models of different specimens for different mechanisms.....83

Figure 3. 11 The  $\mu^* - \sigma$  and  $\mu^* - \mu$  plot for the damage in the patch, aluminum and the whole structure. ....87

Figure 3. 12 The  $\mu^* - \sigma$  and  $\mu^* - \mu$  plot for the laminar plasticity, intralaminar fracture, delamination, and debond at the interface.....90

Figure 4. 1 Configuration of the eccentrically loaded single edge specimen, all in inches. ....96

Figure 4. 2 Configuration of the eccentrically loaded single edge specimen repaired with the composite patch, all in inches.....96

Figure 4. 3 Layup of the composite patch.....98

Figure 4. 4 The setup of the vacuum bagging system to fabricate the composite patch.....98

Figure 4. 5 The experimental setup for the cracking test of unrepaired specimen. .... 100

Figure 4. 6 The experimental setup for the cracking test of the unrepaired specimen. ....	100
Figure 4. 7 Crack initiation and propagation of the single edge crack specimen .....	102
Figure 4. 8 The definition of the crack angle. ....	102
Figure 4. 9 Fracture surface of the unrepaired specimen. ....	103
Figure 4. 10 Crack initiation and growth in composite patch repaired specimen. ....	104
Figure 4. 11 Zoom in pictures of the crack tips in repaired specimen right before (a) and after (b) the disbond at the bond line. ....	106
Figure 4. 12 The schematic diagram of the disbond area and the crack path...	106
Figure 4. 13 Comparison of the load-displacement curves of patched and unpatched specimens. ....	107



# CHAPTER I INTRODUCTION

## 1.1 Cracking in Marine Aluminum Structure

The continuing demand for ships with faster speeds, higher payloads and larger ranges, as well as the rapid development in aluminum technology, are promoting the resurgence of aluminum in ship manufacturing. In comparison with steel, which is the main building material of conventional ships, aluminum has a higher strength to weight ratio, better corrosion resistance, and weldability. Additionally, the high fuel efficiency, less painting cost, and good recyclability are driving the increase of the interest in aluminum structures [1, 2].

However, aluminum ship structures also inevitably experience different forms of damage such as cracking during their service life, as shown in Fig. 1.1. Aside from the fatigue load, corrosion is another main reason for assisting the cracking failure in marine structures. One of the most commonly used aluminum alloys in ship structures is 5xxx series, in which the concentration of magnesium is normally above 3 wt%. It can become susceptible to sensitization, which is characterized by the formation of  $Al_2Mg_3$   $\beta$ -phase along the crystal grain boundary when subjected to an elevated temperature over a prolonged period of time. Combined with a corrosive environment and tensile stress, sensitization can result in stress corrosion cracking (SSC). The dissolution of  $\beta$ -phase coupled

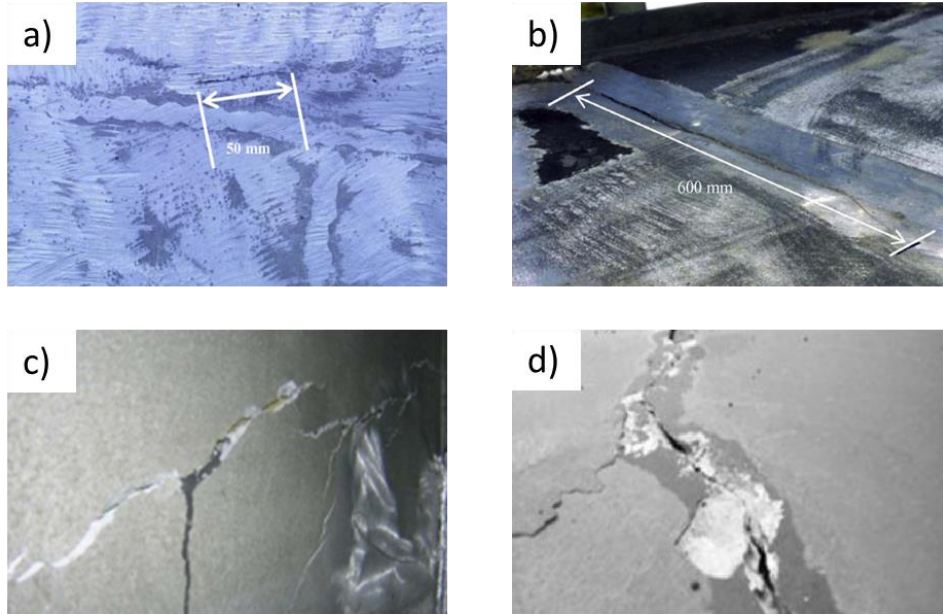


Figure 1. 1 Examples of cracking in marine aluminum structures, a and b) fatigue cracking detected in the deck of a Royal Australian Navy frigate [3], c and d) stress corrosion cracking in US Navy vessels [4, 5].

with the hydrogen embrittlement during SCC enables a much lower crack growth threshold.

## **1.2 Composite Repairing Method**

Serious concerns for restoring the load capability of cracked aluminum structures led to the development of different repairing methods. There are two conventional methods to restore the damage tolerance of cracked metal structures: localized welding of cracks and replacement repair. Localized welding is performed to mechanically excavate the cracked region after it has been detected, after which it is repaired with a full-penetration weld joint design. Replacement involves cutting off the damaged part and replacing it with an intact one by welding. However, this process may be time-consuming and difficult to apply for complex structures, or if a crack is identified during a deployment. Moreover, welding could introduce extra defects, which result in stress concentration issues.

An alternative repair method is the bonded fiber reinforced composite patch. The installation of composite patches is a demonstrated approach to reinforce or repair metallic structures in engineering fields such as aerospace [6-8], marine [3, 9], automotive [10, 11] and infrastructure [12, 13]. Composite patches, bonded to metallic structures by adhesive or co-cured bonding methods [8, 14], effectively reinforce under-designed regions and restore the load carrying



Figure 1. 2 Composite patches installed on marine aluminum structures [3, 4].

capacity to fatigue-cracked or corrosion-damaged parts. Uniform stress transfer, easy installation, customized stiffness, high specific strength, adaptability to complex substrates, and excellent corrosion resistance [8] make bonded composite repairs more attractive to the marine applications than traditional repair methods. More importantly, the composite patches enable reduced cost and repair time because their manufacturability is within the capability of ship's force.

Composite patches have been widely used by the aerospace industry in aircraft structures and skins for several decades, but their use on marine structures has been limited. Recently, the increasing interest of composite patch applications on marine structures has led to extensive research work. Figure 1.2 shows some examples of composite patches installed on the aluminum deck of Navy ships. Grabovac, et al. [3] reported that the carbon fiber composite patches implemented on a Royal Australian Navy frigate show its ability to restore the strength of the damaged structure and its durability, 15 years after it was first installed. Weitzenbock, et al. [15] showed examples of the successful use of bonded patch repair on floating production storage and offloading (FPSO) units. Also, a DNV Recommended Practice (RP) on bonded patch repair is established to summarize these experiences and the Joint Industry Project (JIP) results. Furthermore, it has been reported that 1300 sq. ft of composite patch repair

prototypes were implemented on 10 ships by US Navy and demonstrated their ability to restore the damage tolerance of marine structures from 2010 to 2014.

### **1.3 Optimization of the Composite Patch**

Due to the complex nature of the fiber reinforced composite patch as shown in Fig. 1.3, it is challenging to optimize the patch design considering so many factors. A thorough understanding of how those factors affect the patch performance is essential to overcome the design challenge. There is a considerable amount of prior research studying the influence of different design parameters on the cracking behavior of repaired structures, including aluminum plate thickness, loading conditions, adhesive shear modulus, adhesive disbond area, patch geometry, etc.

Regarding the damaged metal substrate, Mall and Conley [16] showed the difference between thin and thick plates repaired with a single-sided patch. While there was significant bending between the unpatched and patched faces of the repaired thick plate due to asymmetry, bending was almost negligible in repaired thin plates. Therefore, the composite patch presents a better performance on thin plates as the bending can reduce the life extension of repaired plates. Their study also showed that the composite patch with the same size and materials can extend the fatigue life of the thick plate by 4 times while extend that of the thin plate by 10 times. Bouiadjra, et al. [17] analyzed the stress intensity factor for

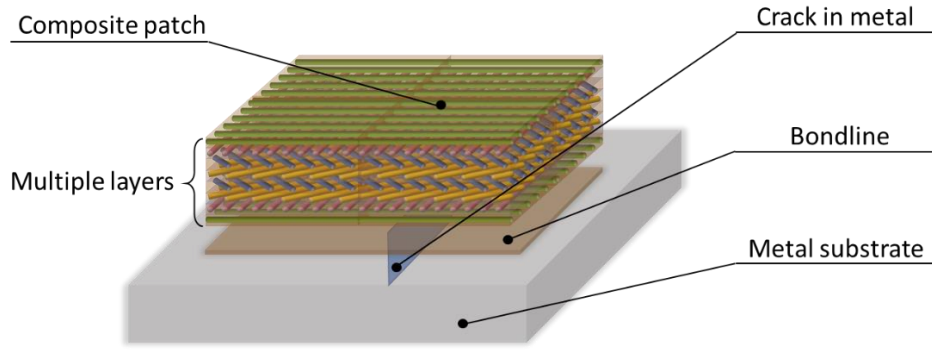


Figure 1. 3 Cracked metal structure repaired with composite patches.

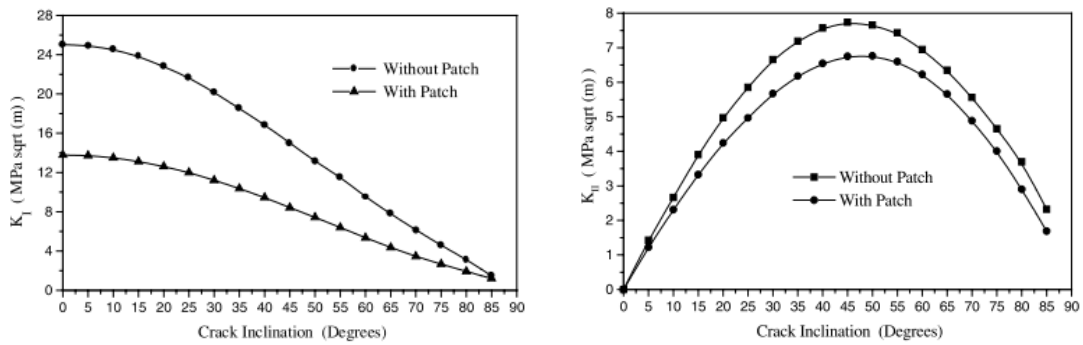


Figure 1. 4 Comparison of the mode I and mode II SIF between the patch and unpatched crack in the mixed model [17].

repaired cracks in mixed mode. They showed that the mode I stress intensity factor is more affected by the presence of the patch than that of mode II as shown in Fig. 1.4. Chung and Yang [18] studied the mixed mode fatigue crack growth in repaired aluminum plates. They observed that the composite patch obtained the maximum effect from the plate with a  $0^\circ$  inclined crack and relatively small effect for the  $30^\circ$  and  $45^\circ$  inclined crack cases.

The bond line is the most important part of the patch repair structure since it is the key to transferring stress from the cracked plate to the patch. Debond is a common problem of composite patch repair and has gained attention from researchers. Ouinas, et al. [19] studied the effect of disbond on the repair performance. They showed that the increase of disbond length in the direction perpendicular to the crack could result in a greater increase of the stress intensity factor at the crack tip than that in the direction along the crack. According to the results of Ouinas, the bond line with high shear modulus is more effective in reducing the stress intensity factor of the crack, while it is more vulnerable to failure. Moreover, bond line with a smaller thickness is less affected by the disbond than one with a larger thickness. Bouiadjra, et al. [20] concluded that the decrease in adhesive thickness is able to reduce the stress intensity factor more as shown in Fig. 1.5. Benyahia, et al. [21] analyzed the performance of aged bonded composite patch repair. They accelerated the aging process of the repair by immersion in water for 120 days and concluded that the humidity



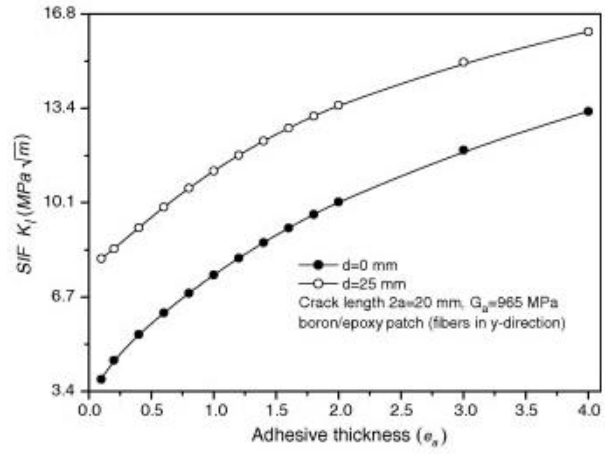
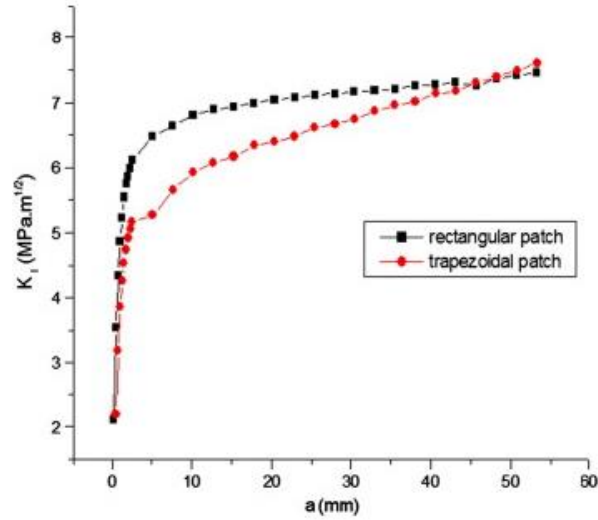


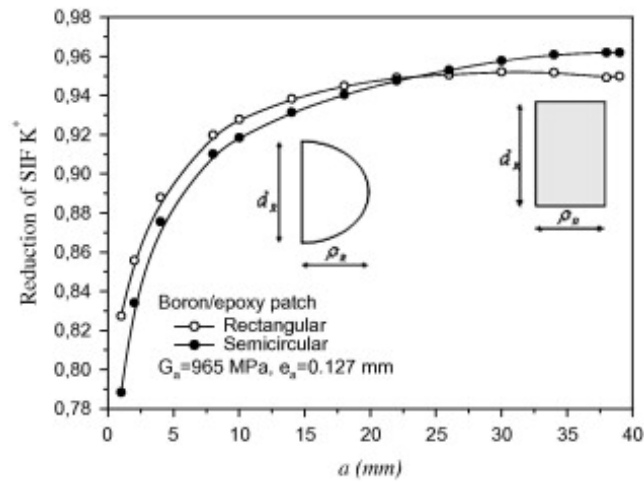
Figure 1. 5 The effect of adhesive thickness on the stress intensity factor on the repaired crack [20].

absorption could weaken the repair performance significantly, although it also decreased the bond line stress.

Fiber orientation, patch shape, and thickness are the most common parameters considered in implementing a composite patch repair. Ramji, et al. [22] studied the performance of patches with different shapes. They observed that the extended octagon patch obtain a better reduction of the stress intensity factor compared with circular, rectangular, square, and rotated elliptical patches. Bouiadjra, et al. [23] conducted a numerical analysis to compare rectangular patch with the trapezoidal patch. They concluded that the trapezoidal patch was lighter and more effective in reducing the adhesive stress than the rectangular patch when the crack length ranged from 5 to 20 mm as shown in Fig. 1.6(a). Ouinas, et al. [19] compared the performance of a semicircular and rectangular patch and showed the performance of different shapes varies with the crack length in the repaired structure. According to Fig. 1.6(b), it is clear that the rectangular patch reduces the SIF more than semicircular one when the crack is length is larger than 25 mm. But the semicircular patch reduces more when the crack is shorter than 25 mm. Toudeshky, et al. [24] performed numerical and experimental analysis of the effect of the number of patch layers on fatigue life of repaired aluminum plates. They showed that increasing the number of patch layers for the thin plate is much more effective to extend the fatigue life of



(a) Single sided rectangular and trapezoidal patch [23]



(b) Single sided semicircular and rectangular composite patch [19]

Figure 1. 6 The stress intensity factor of crack repaired with composite patches with different shapes varies with the crack length in the repaired plate.

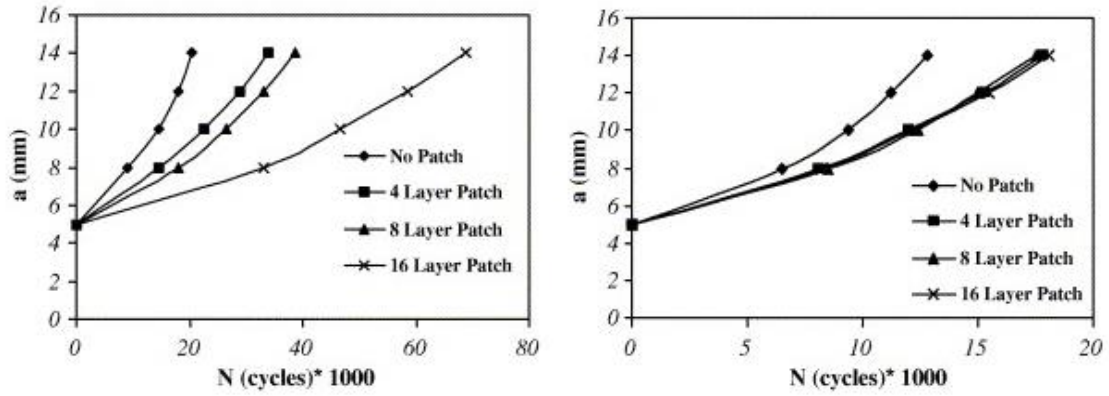


Figure 1. 7 Effect of the number of layers on fatigue life of repaired thin and thick plate [24].

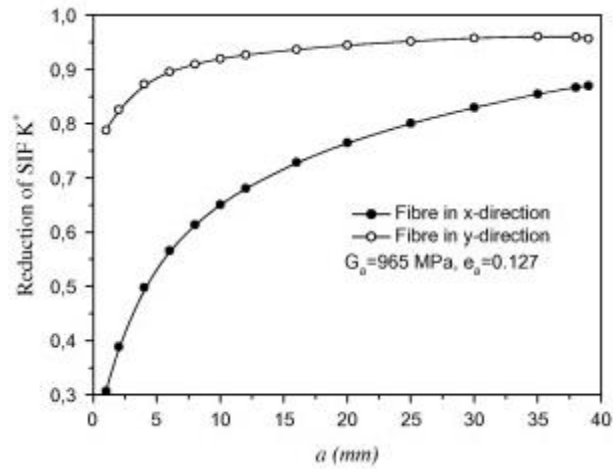


Figure 1. 8 Performance of composite patch with different fiber orientations, the crack is along the x-direction.

repaired plate compared to the thick plate as shown in Fig. 1.7. Ouinas, et al. [19] concluded that the composite patch obtained more reduction of stress intensity factor when the fiber orientation was perpendicular to the crack propagation as shown in Fig. 1.8.

## **1.4 Objectives**

Although considerable research has been performed to study the effect of different factors on the patch performance, most of these studies varied one factor a time with all other factors fixed to determine the influence of the factor on crack behavior, known as one-factor-at-a-time (OAT) sensitivity analysis. OAT is proven to be inadequate as a sensitivity analysis tool due to the limitation on estimating the global influences and interactions of inputs [25]. It is necessary to conduct a global sensitivity analysis considering the interactions between different factors to obtain a more reliable sensitivity information for the optimization of patch design. Iooss and Lematre [26] reviewed the distinction, advantages, cost, and application of a variety of available global sensitivity analysis techniques. The variance-based method (also known as Sobol indices) [27] and the elementary effect method (EEM) [28] are employed in this dissertation. The Sobol indices method is one of the most widely used sensitivity analysis methods that generally provides better information to indicate interactions between different parameters. However, it could be computationally expensive to obtain an accurate estimation of Sobol indices when many input

factors (generally more than 15 factors) are investigated. The EEM is an effective alternative to reduce the computational burden while offering comparable results. The Sobol indices and the EEM are used to perform the sensitivity analysis for two cases with 13 and 41 inputs respectively.

A high-fidelity model is essential to obtain an accurate estimation of the sensitivity information of the composite patch design. However, there are still some limitations of the patched structure models used in most of the research work published in the literature. Firstly, a majority of research conducted a numerical analysis of the hybrid structures by a 2D finite element model. Typically, damaged structures aboard vessels are repaired with single-sided patches, and the repaired metals are thick, greater than 0.25 inch, compared with that of aircrafts. The complex distribution of the stress intensity factor on the crack front cannot be captured by a 2D model in those cases. Secondly, a considerable amount of prior research on the damage analysis of composite patches focus on topics such as the fracture behavior of bonded metallic substrates [16, 19, 22-24] and disbond of adhesives [21, 29, 30]. Although progressive damage in composites has been widely investigated [31-37], few studies take into account the progressive failure of the entire hybrid (composite, bond line, and metal) structure, a necessary consideration when evaluating the structural performance of the patched structure. A primary concern when evaluating the progressive damage of bonded composite patches is non-visible

damage. Non-visible damage, located internally and often not identifiable without destructive inspection, can occur when the patch is subjected to general design loads or overloads during service, particularly bending stress [38-40] and low-velocity impact [41]. This non-visible damage can be present as disbond at the interface between the patch and the metal substrate, delamination within the patch, fiber fracture or local buckling, and matrix cracking. Such damage might initially be minor but then propagate under additional loading and degrade patch performance. It has been demonstrated that the damage within the composite patch can substantially reduce the efficiency of the reinforcement or repair [42, 43]. Jones [42] also indicated that multiple failure modes, including cracking in the adhesive or at the adhesive-metal interface, fiber fracture, and delamination, should be evaluated when performing damage tolerance assessment. Therefore, it is necessary to consider multiple damage mechanisms, including the progressive failure of the composite patch and the interactions between the damage mechanisms when predicting damage initiation and propagation in the patched structure.

This dissertation intends to cover the research gaps stated above and provide a better understanding of the effects of the aforementioned factors to improve the design efficiency of composite patches. To achieve those goals, the following tasks are performed,

1. predict the crack propagation in aluminum using compact tension test and FE modeling and determine the most influential parameters on the crack growth considering the effect of uncertainties,
2. evaluate the progressive damage of the composite patch with four-point bending test and FE modeling and identify the most influential parameters on damage tolerance,
3. study the shear band localization introduced mixed mode crack and the crack behavior in aluminum repaired with a composite patch.



# CHAPTER II EFFECT OF UNCERTAINTIES ON NUMERICAL PREDICTION OF CRACK PROPAGATION

## 2.1 Introduction

Fracture modeling is an efficient method to predict crack growth and estimate the damage tolerance in engineering structures. Different numerical analysis strategies have been developed for modeling crack propagation, such as cohesive fracture models [44-47], extended finite element methods (XFEM) [48-51] and meshfree methods [52-55]. The crack propagation in engineering structures is usually affected by uncertainties from many sources such as material properties, geometry, and boundary conditions. Understanding the effects of the uncertainties on crack growth and considering those uncertainties in modeling the crack growth are essential for an accurate and reliable fracture simulation [56, 57]. Many efforts have been devoted to investigating the uncertainties involved in fracture modeling [58-64]. However, crack prediction with high accuracy and reliability is still a challenging problem due to expensive computational requirements and a large number of uncertainties, especially for complex structures.

This chapter presents an integrated approach that combines experimental testing, computational simulation, and sensitivity analysis to efficiently explore

the effects of uncertainties on the numerical prediction of crack propagation. The experimental testing provides validation data and parameter characterization for the computational models that generate the required data for the sensitivity analysis. In return, the sensitivity analysis determines the influential parameters that need more comprehensive and rigorous characterization to improve the precision of experiment and simulation results and the noninfluential parameters that could be ignored to reduce the number of uncertainties demanding extensive attention.

Compact tension (CT) testing is one of the most commonly used standardized testings to estimate the fracture behavior of different engineering materials. The crack growth in CT specimens is selected as a demonstration problem in this study. Different uncertain factors of CT specimen have been investigated about their effects on the crack behavior. For example, side grooves applied on CT specimen for a uniform crack are confirmed by several authors to have effects on the crack behavior [65-68]. Ono et al. [69] conducted CT testing using four standard steel specimens of different sizes. They stated that the fracture toughness increased with the decreasing of the specimen thickness and the fracture toughness decreased when specimens were miniaturized at the same proportions. Plaza [70] summarized uncertainties might be involved in a CT testing and provided a series of mathematical formulae to calculate the uncertainties. Although considerable research has been performed to study the

effect of uncertainties on the crack growth of CT specimen, most of these studies varied one factor at a time with all other factors fixed to determine the influence of the factor on crack behavior, known as one-factor-at-a-time (OAT) sensitivity analysis. OAT is proven to be inadequate as a sensitivity analysis tool due to the limitation on estimating the global influences and interactions of inputs [25].

The Sobol indices method applied in this chapter for the sensitivity analysis is able to consider the effects of each individual factor and their interactions. The 3D XFEM model validated by experimental testing is developed. The surrogate model built on the XFEM simulation results are used to reduce the computational burden of generating the required data for the sensitivity analysis.

## **2.2 Experimental Work**

All the experimental testing data used in this chapter is provided by Dr. Rick Link from United States Naval Academy. CT specimens were manufactured from a 0.25-inch thick hot rolled Al 5456 plate. The hot rolling processing could result in anisotropic fracture properties of aluminum alloy [71]. Therefore fracture toughness of Al5456 in both rolling and transversal directions was measured experimentally. Two tensile tests were performed to obtain the elastic-plastic properties of the aluminum. The stress-strain curve averaged from two testing, as shown in Fig. 2.1, is used to estimate Young's modulus ( $E$ ), yield strength ( $\sigma_Y$ ), Poisson ratio ( $\nu$ ) and strain hardening, as shown in Table 2.1. The plastic

behavior of the aluminum was described by the Ludwik-Hollomon equation (Eq. 2.1) without considering the effect of strain rate and temperature since the CT testing is a quasi-static process with negligible temperature variation in this study.

$$\bar{\sigma} = A + C\bar{\epsilon}^n \quad (2.1)$$

where  $\bar{\sigma}$  is the equivalent plastic stress,  $\bar{\epsilon}$  is the equivalent plastic strain,  $A$ ,  $C$ ,  $n$  are material properties obtained via fitting the tested stress-strain curve.

Four CT specimens, as depicted in Fig. 2.2, were designed following the ASTM standard [6] and manufactured using the wire electrical discharge machining process. In Fig. 2.2(a),  $W$  is defined as specimen width,  $B$  is the thickness of the specimen,  $a_s$  is the length of machined initial notch,  $a_f$  is the length of fatigue pre-crack and  $a_0$  is the initial crack length. Side grooves, as shown in Fig. 2.2(b), were added after pre-cracking the specimen to reduce the low triaxiality zone near the outer specimen surface and ensure a clear measurement of crack initiation and extension [67]. Specimen\_1,2 were machined with a notch in T-L direction and specimen\_3, 4 were machined with a notch in the L-T direction as shown in Fig. 2.2(c). The configuration and tested fracture toughness,  $J$ , of four specimens are shown in table 2.2. Specimen\_1,2 shows larger fracture toughness than that of specimen\_3,4, indicating that the fracture toughness in the rolling direction is higher than that in the transversal

Table 2. 1 Elastic and plastic properties of Al5456

$E / Psi$	$\sigma_y / Psi$	$\nu$	$A$	$C$	$n$
1.0 E+07	2.2 E+04	0.3	2.2 E+04	7.2 E+04	0.34

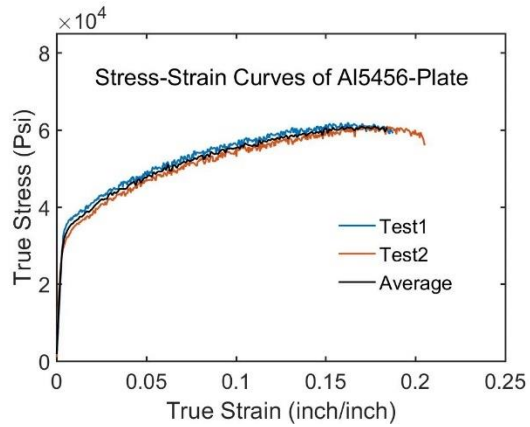
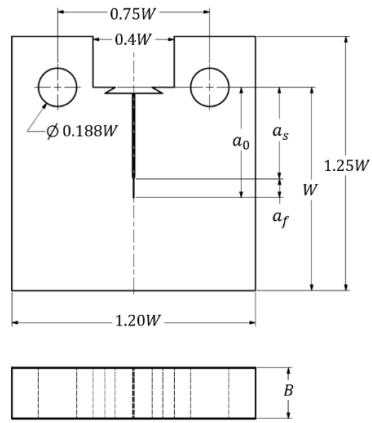


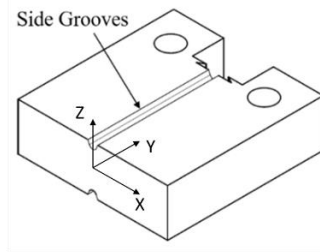
Figure 2. 1. The stress-strain curve is averaged from the tension testing results.

Table 2. 2 Geometry parameters and testing results of different CT specimens

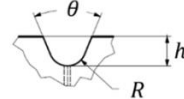
Specimen ID	Notch Orientation	$W, inch$	$B, inch$	$a_0, inch$	$h, inch$	$R, inch$	$\theta, rad$	$J, lbf \cdot inch^{-1}$
1	L-T	1	0.25	0.548	0.026	0.01	$\pi/4$	177
2	L-T	1	0.25	0.538	0.026	0.01	$\pi/4$	168
3	T-L	1	0.25	0.549	0.025	0.01	$\pi/4$	130
4	T-L	1	0.25	0.545	0.025	0.01	$\pi/4$	121



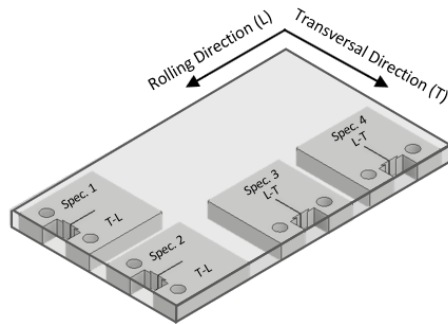
(a) Configuration before adding side grooves



Section View of Side Grooves



(b) Geometry features of side grooves



(c) Notch orientation of specimen\_1,2,3,4

Figure 2. 2 Configurations of four CT specimens.

direction. Fatigue load was applied to each specimen after the CT test to acquire a smooth crack surface which could be used to recognize the final crack front. All specimens were split into two pieces under tension load to observe the crack surface as shown in Fig. 2.3. The crack fronts of all specimens indicate that the crack grows relatively uniformly in the through-thickness direction due to the side grooves. In CT specimens without side grooves, the interior has a high stress triaxiality that leads to higher stresses in the plastic zone near the crack tip, which assists crack to grow faster than the crack near the outer edges with low stress triaxiality. The side grooves can increase the stress triaxiality at the outer edges to obtain a uniform crack growth in the through-thickness direction.

### **2.3 Finite Element Analysis**

Performing physical experiments to study the effects of various relevant factors on crack growth is time-consuming. Additionally, it is not feasible to control the experimental uncertainty to a high enough degree to capture every factor. Computational simulation is an alternative method to perform a comprehensive study to quantify the effects of all factors in a time and cost efficient manner once a physics-based baseline model is validated by experimental testing. The testing results of four CT specimens are used to validate the computational prediction of crack growth here.

The cohesive zone theory based XFEM is selected to predict crack growth behavior due to its advantage of mesh independence. The results of 2D and 3D

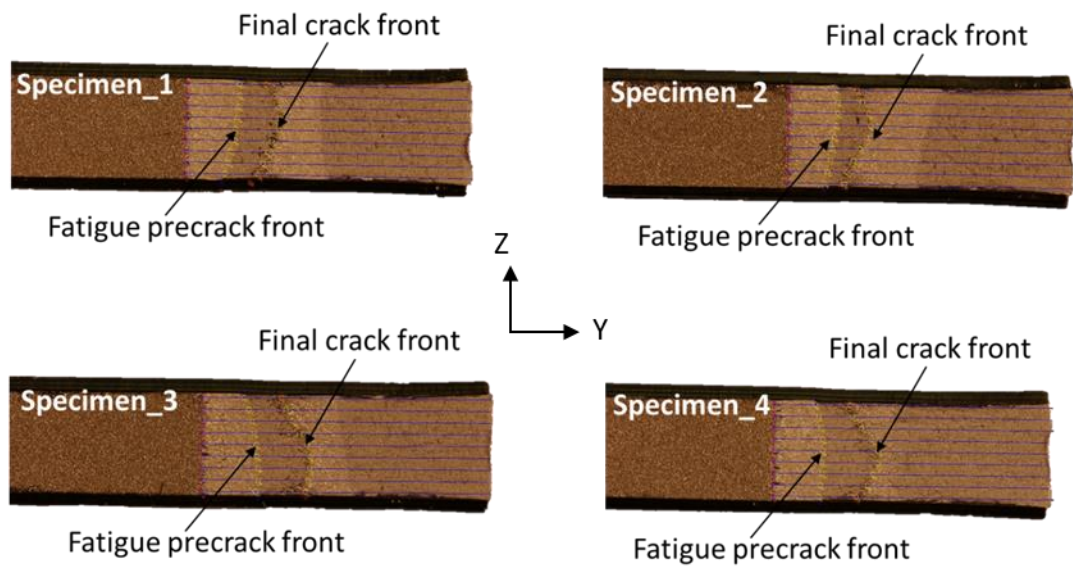


Figure 2. 3 Crack surface of four CT testing specimens.



XFEM models are compared in analyzing the fracture behavior of the CT specimens. A linear cohesive damage model, as shown in Fig. 2.4, was selected because of its simple constitutive equation (Eq. 2.2) and widespread use.

$$\begin{cases} t = K\delta, & t \leq t^0 \\ t = \frac{t^0(\delta - \delta^f)}{\delta^0 - \delta^f}, & t > t^0 \end{cases} \quad (2.2)$$

where  $t$  is the traction,  $\delta$  is the separation,  $K$  is the interface stiffness relating the traction and corresponding separation before the initiation of the damage,  $t^0$  is damage initiation stress,  $\delta^0$  is the separation where the damage initiates,  $\delta^f$  is the maximum separation where the element totally fails. The critical fracture energy  $J_c$  has the same value as the shaded area under the triangle in Fig. 2.4.  $J_c$  is directly measured from experiments and  $t^0$  is obtained by fitting the experiment data.

The triangular traction-separation law consists of a damage initiation criterion and a linear damage evolution law. The damage initiation is predicted using the maximum nominal stress criterion (Eq. 3),

$$\begin{cases} \left(\frac{t_I}{t_I^0}\right)^2 + \left(\frac{t_{II}}{t_{II}^0}\right)^2 + \left(\frac{t_{III}}{t_{III}^0}\right)^2 = 1, & \text{if } t_I > 0 \\ \left(\frac{t_{II}}{t_{II}^0}\right)^2 + \left(\frac{t_{III}}{t_{III}^0}\right)^2 = 1, & \text{if } t_I \leq 0 \end{cases} \quad (2.3)$$

where  $t_I$ ,  $t_{II}$ ,  $t_{III}$  are tractions for Mode I, Mode II and Mode III fracture  $t_I^0$ ,  $t_{II}^0$ ,  $t_{III}^0$  are the damage initiation stresses for the three modes of fracture. However, terms related with Mode II and III in Eq. 2.3 are ignored since there's only Mode I

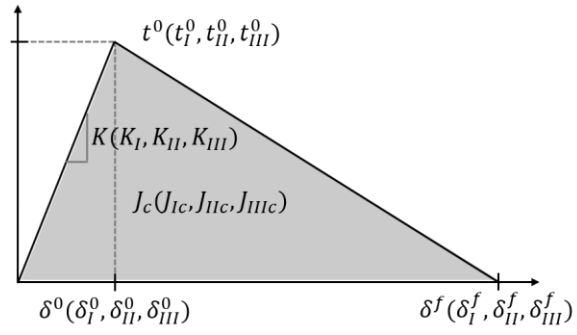


Figure 2. 4 The bilinear traction separation cohesive law.

fracture appearing in the CT testing. Once the damage initiation criterion is met, the degradation of elements occurs according to the traction-separation response. Since the strain energy release rate is solely contributed by Mode I fracture in CT specimens, the fracture criterion can be simplified as

$$\frac{J}{J_{Ic}} = 1 \quad (2.4)$$

$J_{Ic}$  and  $K$  are calculated from the CT and tension testing.  $t^0$  is determined by fitting the load and crack mouth opening displacement (CMOD) curve of numerical models to match the experimental curve. The linear cohesive zone model is decided when  $J_C$ ,  $K$  and  $t^0$  is specified.

The FE model was implemented in the FE code ABAQUS. The loading pins were modeled with the analytical rigid body to create more precise boundary conditions. The first order plane strain (CPE4R) and plane stress (CPS4R) elements were used for the aluminum in the 2D models and the solid element (C3D8R) in the 3D model. The mesh refinement was presented at the crack tip area and the root of the side grooves in the 3D model to obtain an accurate stress calculation as shown in Fig. 2.5. The interaction between the aluminum and the loading pins is assumed to be frictionless. A displacement is applied to one of the loading pins in the X direction to simulate the tensile load while it is restricted in all other five degrees of freedoms (DOFs) and the other pin is restricted in all DOFs.

The load-CMOD curves obtained from plane stress, plane strain, and 3D models are compared with the experimental result of specimen\_1, as shown in Fig. 2.6. The curve of the 3D model is most consistent with the experimental curve and lies between the curves of plane strain and plane stress models. The 3D model takes account into the variation of the state of stress near the crack tip in the through-thickness direction [72]. In the interior of the CT specimen near the crack tip, the higher stress in the through-thickness direction results in a higher triaxiality, which is similar to the plane strain state. On the other hand, the stress triaxiality in the region near the free surface is lower that is more like the plane stress state. Therefore, the 3D model and experiment load-CMOD curves are between the curves of plane stress and plane strain. Due to the advantage of predicting fracture behavior of CT specimens more precisely, the 3D XFEM model is used as the baseline model to investigate the effects of uncertainties on the fracture behavior of CT specimens.

The load-CMOD curves of four specimens calculated from simulations agree well with the experimental data, as shown in Fig. 2.7, except that the load drops faster at the very end of the simulated curves. The rate of the load decrease after the peak load at the curve is determined by the plastic behavior, the fracture toughness and the damage initiation stress in the XFEM model. Especially the dropping rate at the very end of the curve is found to be sensitive

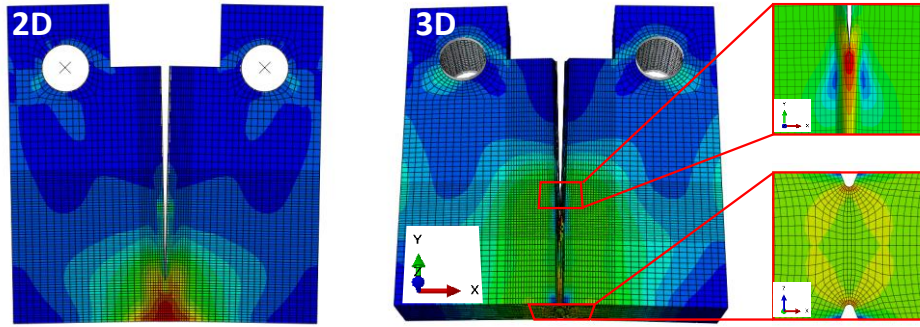


Figure 2. 5 Mesh refinement at the crack tip and the roots of the side grooves in the XFEM model.

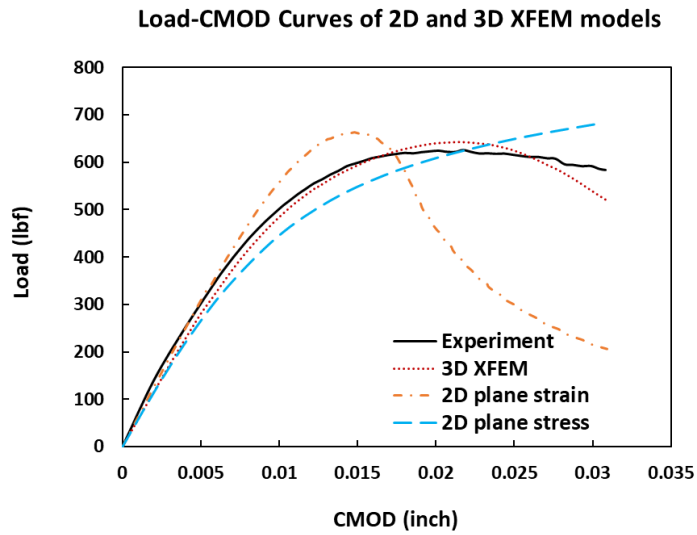


Figure 2. 6 The comparison of load-CMOD curves for specimen\_1 obtained from experiment and different FE models.

to the plastic hardening behavior of the aluminum. The load-CMOD curves were calculated from specimen\_1 with different plastic behavior by varying the exponent  $n$  in the Ludwik-Hollomon equation, as shown in Fig 2.8. It shows the load drops much faster at the end of the curve when decreasing  $n$  to 0.31. Because the strain hardening is enhanced and sequentially results in the unstable crack growth at the end of the simulation. Vice versa, the load drops slower at the end of the curve by increasing  $n$  to 0.37 as the reduced strain hardening causes a more stable crack growth at the end. Therefore, the mismatch at the end of the load-CMOD curves could be a result of variation of the plastic properties of the testing materials. The slight difference of the crack shape between the simulation and testing results is caused by some uncertainties of the experiments. Those uncertainties include the randomly distributed defects and imperfections in the alloy, and the imperfect symmetry of specimen geometry and boundary conditions in the physical testing. It is difficult to take into account those uncertainties into the XFEM model. However, the XFEM models with homogeneous material properties and a perfect symmetric geometry reproduce comparable load-CMOD curves within certain CMOD range and the crack extension against the experiment observation according to Fig. 2.7, 2.9.

To ensure the modeling result does not depend on the mesh size, a mesh convergence study was performed in three directions (X, Y, Z) separately of the

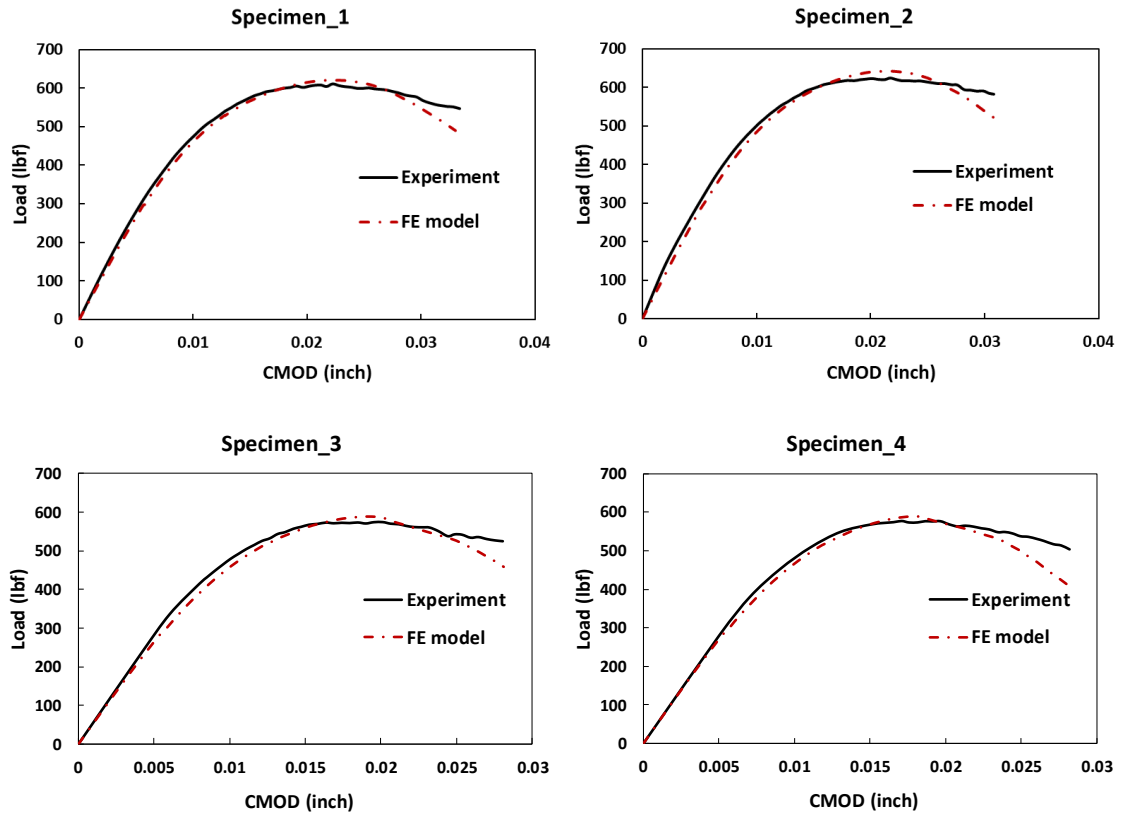


Figure 2. 7 Comparison of load-CMOD curves from experimental and simulation results.

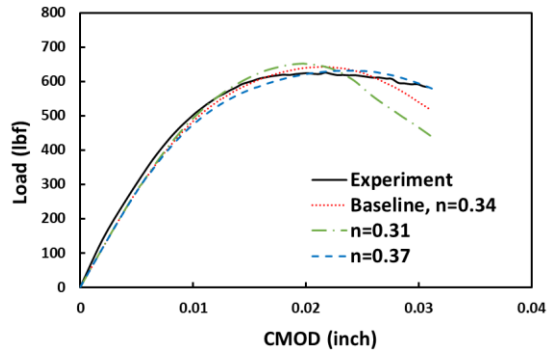


Figure 2. 8 The effect of the  $n$  (plastic behavior) of aluminum on the load-CMOD curves.

3D model. Due to the high nonlinearity of the geometry introduced by the side grooves, it is difficult to obtain a uniform mesh in each direction. Thus, the average length of the element size in each direction is used to perform the mesh convergence study. The average length of the elements in one direction was varied and the average length in the other two directions was fixed when conducting the mesh size study in each direction. Before conducting the mesh convergence study in each direction, the fixed mesh size in the other two directions was selected by searching the converged size of cubelike elements. The load-CMOD curve and the crack extension were defined as the output to determine the converged mesh size. For example, one hundred points were taken from each curve with the same CMOD values and the mean absolute percentage error between every two curves was calculated based on the load values related to those points as presented in the following equation.

$$MAPE_{\varphi,\phi} = \frac{100\%}{100} \sum_{i=1}^{100} \left| \frac{F_{\phi i} - F_{\varphi i}}{F_{\varphi i}} \right| \quad (2.5)$$

where  $MAPE_{\varphi,\phi}$  is the mean absolute percentage error between curve  $\varphi$  and curve  $\phi$ ,  $F_{\phi i}$  and  $F_{\varphi i}$  are the load values of point  $i$  on curve  $\varphi$  and curve  $\phi$ , respectively. The curve is considered as converged when  $MAPE_{\varphi,\phi}$  becomes relatively small and does not change substantially with finer mesh. The  $MAPE_{\varphi,\phi}$  and total CPU time of models with different element size are compared, as shown in Table 2.3. For load-CMOD curves of the model using cubelike elements in Fig. 2.10, the  $MAPE_{\varphi,\phi}$  has a small value of 2.1% and does not have a



significant decrease with smaller mesh size when the element size reaches 0.01 inch. Besides, the total CPU time of the model increase fast without leading to a significant decrease of the  $MAPE_{\varphi,\phi}$  when the element size is smaller than 0.01 inch. The crack extension also converges when the mesh size equals to 0.01 inch, which is detected by the convergence of the maximum CMOD. Figure 2.11 as well indicates the crack extension and the crack shape start to converge when the mesh size equals to 0.01 inch. As a trade-off between the  $MAPE_{\varphi,\phi}$  and the computational cost of the model, this research selected 0.01 inch as the element size when the results of the model with cubelike elements is considered as converged. However, a finer mesh can offer a higher resolution of the image of predicted crack shape which is determined by the size of the element.

The average element length in the X direction varies from 0.005 inch to 0.04 inch and the element length in the Y and Z direction is fixed as 0.01 inch when studying the mesh convergence in the X direction. According to  $MAPE_{\varphi,\phi}$  between the load-CMOD curves in Table 2.3 and the curves in Fig. 2.12, the simulation result is considered to converge when the element size equal to 0.01 inch in the X direction since the  $MAPE_{\varphi,\phi}$  is about 2.1% and rather stable while decreasing the element size. Similarly, the load-CMOD curve starts to converge when the element size equal to 0.01 inch in the Y direction and 0.03 inch in the Z direction. The element size larger than 0.03 inch was not used in the mesh size

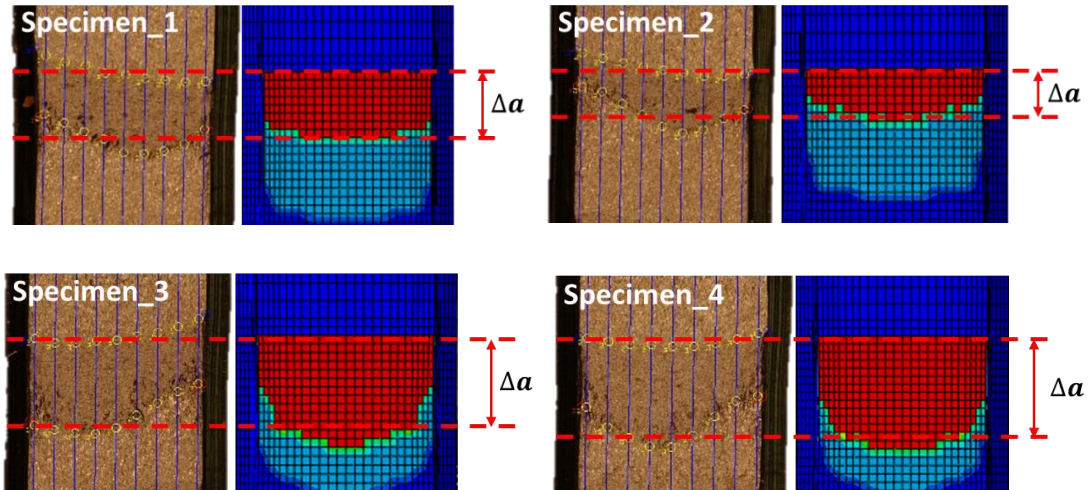


Figure 2. 9 Comparison of the crack extension from experiments and simulations. The red elements in the crack surface of the XFEM model mean the elements are completely cracked. The light blue and green elements are partially cracked. The dark blue elements do not experience any crack.

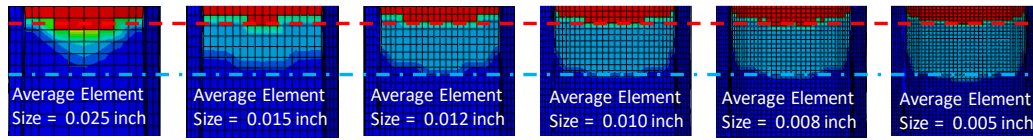


Figure 2. 10 Crack surface of models with different mesh size and fixed aspect ratio of elements. The red elements above the red dash line represent the fully cracked area and the green and light blue elements between the red dash and light blue dash-dot line represent the partially cracked area.

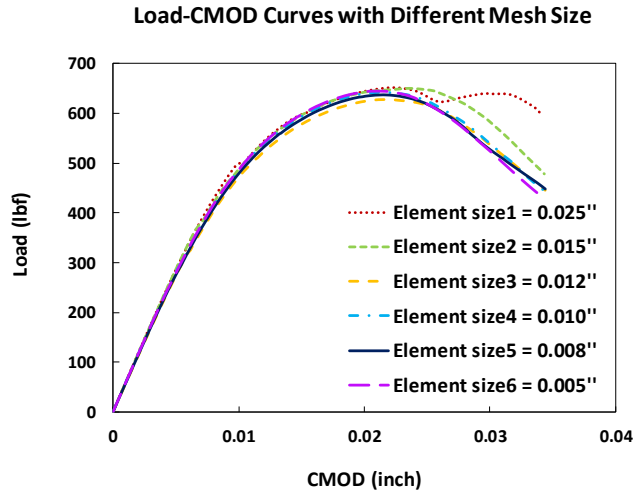


Figure 2. 11 Load-CMOD Curves calculated from models with different size of cubelike elements.

Table 2. 3 Geometry parameters and testing results of different CT specimens, the value of different element size refers to Fig. 2.11 and 2.12.

Element size(k)		Element size1	Element size2	Element size3	Element size4	Element size5	Element size6
Cubelike element	MAPE between element size(k) and (k-1)	N/A	2.8%	4.7%	2.1%	1.1%	1.5%
	Total CPU time (hours)	0.8	2.8	7.0	16.2	57.4	109.0
X direction	MAPE between element size(k) and (k-1)	N/A	0.7%	1.7%	0.2%	0.2%	0.5%
	Total CPU time (hours)	4.6	5.1	7.3	16.2	20.3	42.6
Y direction	MAPE between element size(k) and (k-1)	N/A	18.4%	16.2%	3.9%	1.6%	0.7%
	Total CPU time (hours)	5.1	5.5	8.8	16.2	29.1	61.5
Z direction	MAPE between element size(k) and (k-1)	N/A	0.4%	0.3%	0.4%	0.3%	0.2%
	Total CPU time (hours)	4.6	6.1	11.0	16.2	32.7	100.4

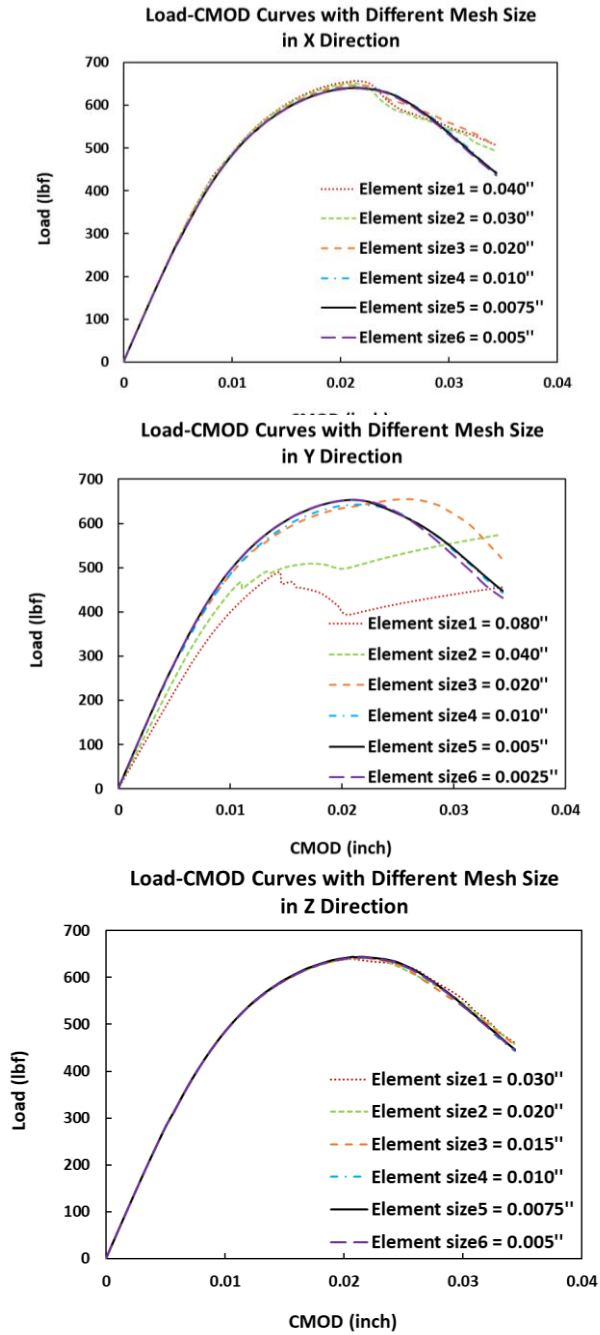


Figure 2. 12 Load-CMOD curves calculated from models varying mesh size in different directions.

study in the Z direction because the larger size can result in a coarse mesh around the area of the root of the side grooves that cannot even describe the geometry correctly. The selected converged mesh size in three directions also exhibits a good trade-off between the  $MAPE_{\varphi,\phi}$  and the total CPU time. Based on the load-CMOD curves with a different mesh size in three directions, it can be concluded that the XFEM model of CT specimens is most sensitive to the mesh size in the Y direction and not sensitive to the mesh size in the Z direction.

## 2.4 Sensitivity Study

Sensitivity analysis is a promising method to explore the influence of uncertainties on the crack behavior of CT specimens and identify the most influential factors. The most commonly used sensitivity analysis method, Sobol indices [73], is used to measure the influence of individual parameters and their interactions through variance calculations within a sample space. Assuming a model is described as the following function,

$$Y = f(\mathbf{X}), \mathbf{X} = \{ X_1, X_2, X_3, \dots, X_m \} \quad (2.5)$$

where  $\mathbf{X}$  is the vector of  $m$  inputs,  $Y$  is the model output, and  $f$  is a square integrable function. The Sobol indices consider an expansion of the function in the following way,

$$f(\mathbf{X}) = f_0 + \sum_{i=1}^m f_i(X_i) + \sum_{i<j}^m f_{ij}(X_i, X_j) + \dots + f_{1,2,\dots,m}(X_1, X_2, \dots, X_m) \quad (2.6)$$

in which  $f_0$  is a constant, other terms are functions of corresponding inputs and each term has a zero mean. Consequently, we can obtain the following equation if squaring both sides of Eq. 2.6.

$$V(Y) = \sum_{i=1}^m V_i + \sum_{i<j}^m V_{ij} + \dots + V_{1,2,\dots,m} \quad (2.7)$$

where  $V(Y)$  is the variance of  $Y$ ,  $V_i$  is the variance of  $f_i(X_i)$  and so on. Dividing both sides by  $V(Y)$  of Eq. 2.7 yields

$$\sum_{i=1}^m S_i + \sum_{i<j}^m S_{ij} + \dots + S_{1,2,\dots,m} = 1 \quad (2.8)$$

where  $S_i$  is the first-order indices,  $S_{ij}$  is the second-order indices and so on.  $S_i$  indicates the influence of  $X_i$  on the variance of output and  $S_{ij}$  shows the influence of interactions between  $X_i$  and  $X_j$  on the variance. Due to the computational intensity of computing all indices, generally only the first-order and total indices are calculated. The total index is the total contribution of one factor to the output variation. For example, the total index of  $X_1$  for a model with three inputs is described as the follow equation

$$S_{T1} = S_1 + S_{12} + S_{13} + S_{123} \quad (2.9)$$

The total indices can be obtained as the following equation

$$S_{Ti} = 1 - \frac{V[E(Y|X_{\sim i})]}{V(Y)} \quad (2.10)$$

where  $E(Y|X_{\sim i})$  is the conditional expectations of the output  $Y$  when the input  $X_i$  is not included. The set of all  $S_i$  and  $S_{Ti}$  allows a fairly good estimation of the model sensitivities at a reasonable cost [73]. This study takes into account the thirteen main inputs including the material properties and the geometry

parameters, as shown in Table 2.4, to study their effects on the maximum load of the CT testing specimen. All the inputs were assigned with reasonable assumed normal distribution because of lacking actual statistics in this work. The mean values of the normal distribution of each input are the same as the values used in the XFEM model of specimen\_1. The effects of the probability distribution on sensitivity analysis was studied by applying three different sets of distributions to the inputs, as shown in Table 2.4. The mean values of each input remain the same in the three sets of normal distributions. For the material properties, Normal\_1 and Normal\_3 have the same set of standard deviations with larger values compared with Normal\_2. Regarding the geometry parameters, Normal\_2 and Normal\_3 are assigned with the same set of standard deviations with larger values compared with Normal\_1. A parametric XFEM model was developed using a python script to efficiently build and analyze models with various combinations of different geometry and material properties.

An accurate estimation of Sobol indices requires a large number of sample data generated from either physical or computational experiments which could be time-consuming and costly. To overcome this issue, this study introduces the surrogate model [74] that is capable of instantly producing thousands of samples. The surrogate model [75] is constructed from a limited number of samples via using simpler mathematic models to mimic the input-

Table 2. 4 The parameters of different assumed normal distributions assigned to the inputs,  $\mu$  is the mean and  $\sigma$  is the standard deviation.

Material properties									
Distribution Parameters		$E$	$\nu$	$t^0$	$J$	$A$	$C$	$n$	
Normal_1, 2, 3	$\mu$	1.0E+07	0.3	8.5E+04	177	2.2E+04	7.2E+04	0.34	
Normal_1		1.0E+06	0.028	8.0E+03	17	2.1E+03	7.0E+03	0.032	Large
Normal_2	$\sigma$	2.5E+05	0.007	2.0E+03	4.2	5.2E+02	1.8E+03	0.008	Small
Normal_3		1.0E+06	0.028	8.0E+03	17	2.1E+03	7.0E+03	0.032	Large
Geometry parameters									
		$W$	$B$	$h$	$\alpha$	$R$	$a_0$		
Normal_1, 2, 3	$\mu$	1	0.25	2.6E-02	$\pi/4$	0.01	0.548		
Normal_1		0.024	0.006	6.0E-04	0.019	2.4E-04	0.013		Small
Normal_2	$\sigma$	0.095	0.024	2.4E-03	0.075	9.5E-04	0.052		Large
Normal_3		0.095	0.024	2.4E-03	0.075	9.5E-04	0.052		Large



output behavior of physical and computational experiments. The Artificial Neural Network (ANN) [76] is selected as the technique to create the surrogate model because of its ability to capture the nonlinear relations between the input and output. The cross-validation measurement [77] is applied to provide a robust validation of the surrogate model by using all the sample data with both training and testing purpose. The number and distribution of the samples are two of the most important factors to develop a high-quality surrogate model. Thus, the Latin Hypercube Sampling (LHS) method is used to generate the samples because its efficiency to better explore the entire sample space with fewer samples. Four hundred samples were generated by LHS and the corresponding outputs were determined by the XFEM models. Additional twenty samples were randomly generated to validate the ability of the surrogate model to predict the unknown samples by comparing the maximum load of the CT testing obtained from the surrogate model with that from the XFEM model. Based on the comparison between the XFEM and surrogate model results, the average absolute percentage error of those samples is about 1%, which shows a good accuracy of the surrogate model to estimate the maximum load. Thus, it is suitable to apply the surrogate model instead of the physical-based XFEM model to produce samples for computing the Sobol indices.

## 2.5 Results and Discussion

The Sobol indices were determined with the maximum load estimated from the surrogate model, as shown in Fig. 2.13. In the case of normal\_1 distribution, there are four most influential parameters which have relatively large values of total indices, the damage initiation stress ( $t^0$ ), the specimen width ( $W$ ), the specimen thickness ( $B$ ) and the initial crack length ( $a_0$ ). Compared with those four inputs, the influence of the other nine inputs are ignorable. With respect to normal\_2 distribution, the Sobol indices shows that  $t^0$  is not a significant important parameter compared with the results of normal\_1. There's no notable difference between the Sobol indices of normal\_2 and normal\_3 distributions. The fact that the Sobol indices vary with different probability distributions assigned to the inputs suggests using appropriate probability distributions is important for determining the most influential inputs. According to the sensitivities in Fig. 2.13, there's no significant difference between the first-order and total indices for most parameters, which means few interactions exist among the inputs. Thus, the OAT technique can be used to investigate the effect of each input on the output and verify the sensitivity information estimated by the Sobol indices.

The normal\_1 distributions are assigned to the inputs and the distribution of the output is calculated as a baseline. The standard deviation of each input is varied to investigate the influence of the probabilistic distribution of an input on

the distribution of the output. For example, regarding the first input listed in Table 2.4,  $E$ , the standard deviation of  $E$  is doubled while keeping the standard deviation of the other twelve inputs the same. The mean values of all the inputs are fixed. Then the distribution of the corresponding output is compared with that of the baseline to decide the influence of  $E$  on the output. This OAT process is repeated to all the other inputs. The result shows the output follows a normal distribution. The probability density function of the output related to the standard deviation change of each input is plotted in Fig. 2.14. The mean value,  $\mu$ , of the output nearly remains the same regardless of the variation of the  $\sigma$  of each input. The  $\sigma$  of the outputs corresponding to the  $\sigma$  change of  $t^0$ ,  $W$ ,  $B$  and  $a_0$  are 94, 115, 81, 99, which increase considerably compared with the baseline  $\sigma$ . The  $\sigma$  change of the other nine inputs do not have a notable effect on the distribution of the output. The difference of the distribution parameters of the output caused by the variation of the probabilistic distribution of each input is summarized in Table. 2.5. This observation agrees well with the Sobol indices analysis, where  $t^0$ ,  $W$ ,  $B$  and  $a_0$  are identified as the most influential parameters with relatively larger total indices and the other nine inputs are considered as noninfluential parameters. As a consequence, the Sobol indices can be used to reduce the number of uncertainties for the uncertainty quantification in the crack propagation modeling.

## 2.6 Conclusion

An integrated approach is proposed to investigate the influence of uncertainties on the prediction of crack propagation. CT specimens are studied as the example problem by performing the experiment testing, numerical modeling and sensitivity analysis. The 3D XFEM model is developed and validated to simulate the fracture behavior of CT specimens. The Sobol indices method is applied with the surrogate model to determine the effects of each parameter and their interactions on the maximum load of CT testing. This study demonstrates the efficiency of the integrated approach to identify the most influential parameters on the crack behavior of CT specimens.

However, selecting the maximum load as the output to perform the sensitivity analysis has certain limitations to identify the most influential parameters. The maximum load is only able to partially describes the crack behavior. As discussed in section 2.3, the crack behavior at the end of the test changes from a stable growth fashion to an unstable growth fashion when enhancing the strain hardening (Fig. 2.8). But the variation of the strain hardening does not result in a significant change of the maximum load. Thus, using the maximum load as the output feature could miss the crack behavior at the end of the test. A more representative output such as the crack extension and final CMOD could be selected to perform the sensitivity analysis to precisely identify the important parameters to the crack growth. This study utilized the maximum load as the

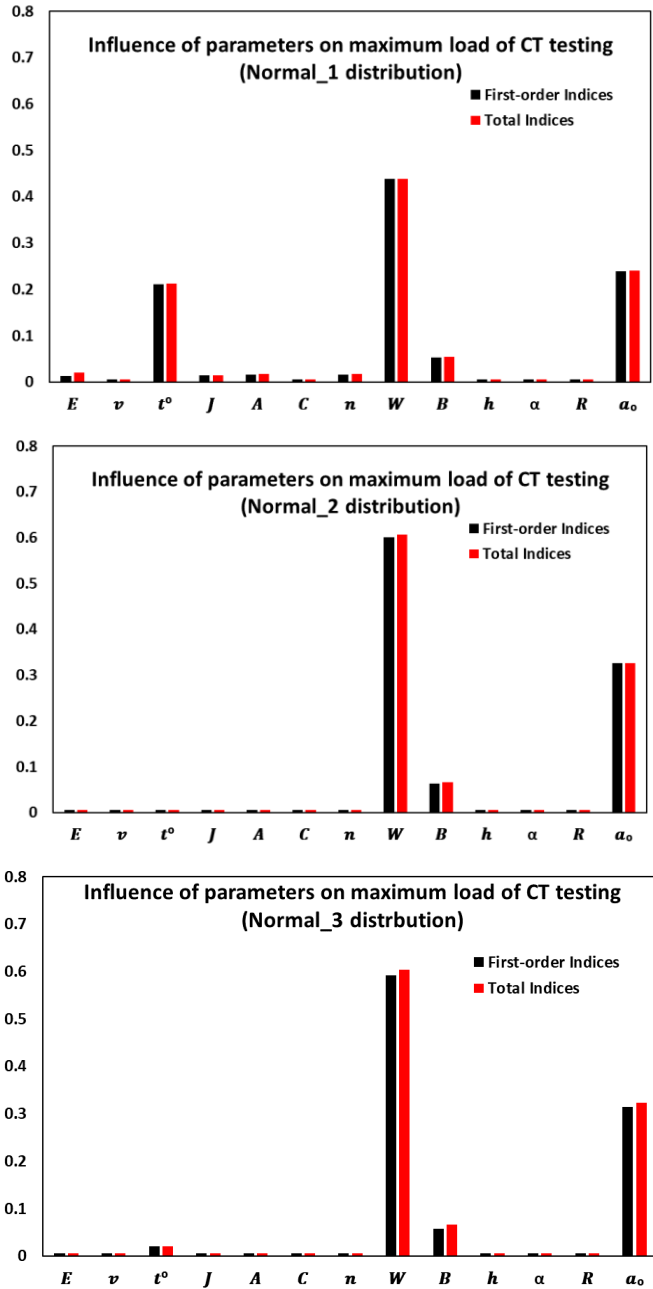


Figure 2. 13 Sobol indices of thirteen parameters including the material properties, geometry parameters, and damage modeling parameters.

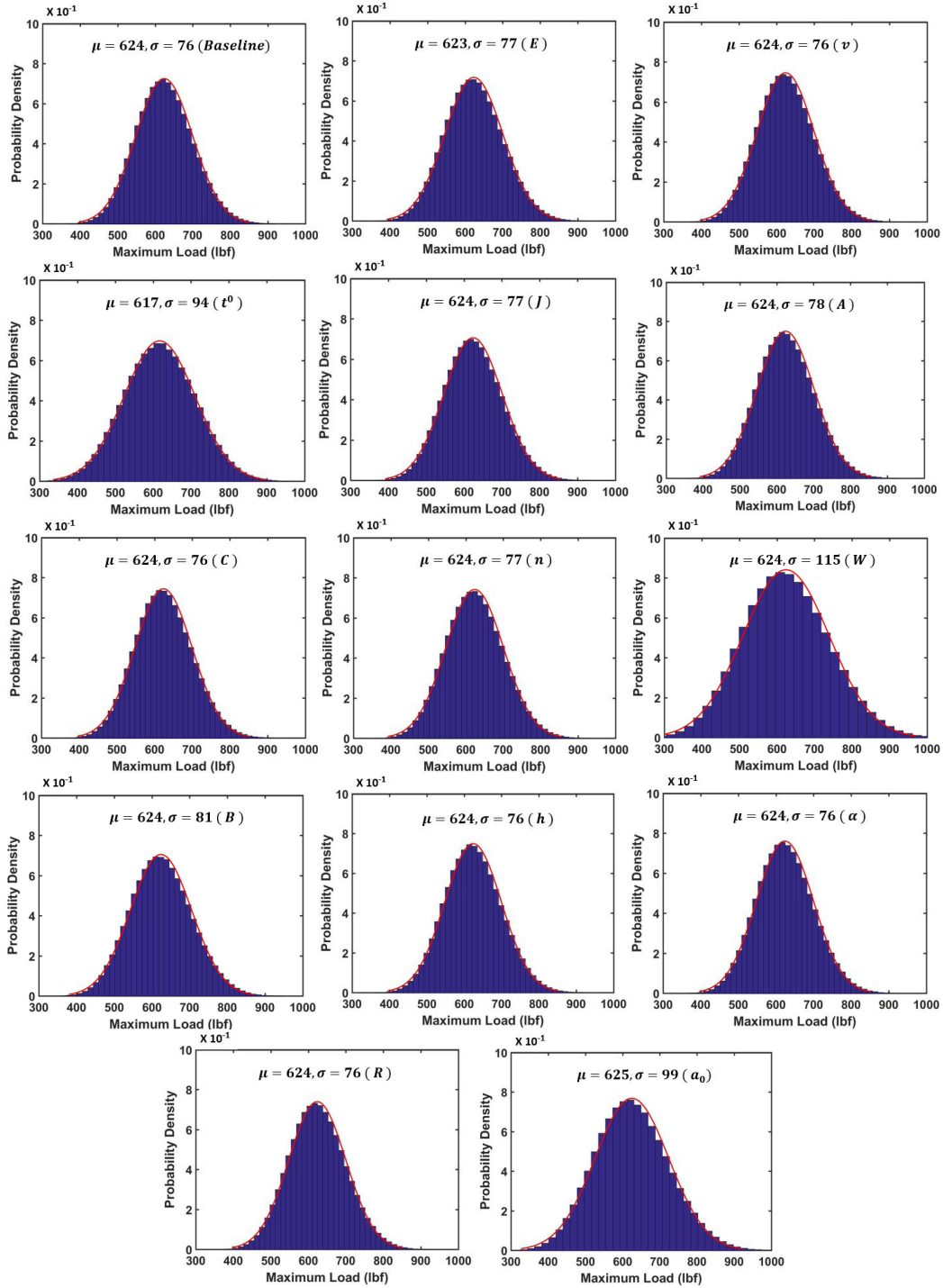


Figure 2. 14 The normal distributions of the maximum load for different inputs distributions.

Table 2. 5 The effect of different parameters on the distribution of the output.

Percentage difference compared with baseline	Material properties						
	<i>E</i>	<i>v</i>	<i>t</i> <sup>o</sup>	<i>J</i>	<i>A</i>	<i>C</i>	<i>n</i>
Difference of $\mu$	0.2%	0.0%	1.1%	0.0%	0.0%	0.0%	0.0%
Difference of $\sigma$	1.3%	0.0%	23.7%	1.3%	2.6%	0.0%	1.3%
	Geometry parameters						
	<i>W</i>	<i>B</i>	<i>h</i>	$\alpha$	<i>R</i>	<i>a</i> <sub>o</sub>	
Difference of $\mu$	0.0%	0.0%	0.0%	0.0%	0.0%	0.2%	
Difference of $\sigma$	51.3%	6.6%	0.0%	0.0%	0.0%	30.3%	

output because the difficulties to construct an accurate surrogate model for the crack extension or final CMOD. A more efficient approach to build the surrogate model is required to obtain a better estimation of the sensitivity information. Additionally, the FE models used to generate the data for constructing the surrogate model are found to have convergence problems with input values having large variation compared with the baseline values. Therefore, improving the robustness of the model is also necessary when exploring a large desired design space of the inputs.

Furthermore, it has been demonstrated that the probabilistic distributions of the inputs have significant effects on the sensitivity analysis results. Therefore, compiling the real statistic information and data of the related inputs is essential to obtain an accurate sensitivity estimation. However, obtaining reliable probabilistic distributions of the inputs usually requires a large amount of data, which could be difficult when only limited data are available. A potential solution to this problem is using probabilistic sensitivity analysis instead of deterministic sensitivity analysis. Unlike the deterministic analysis that assigns a specific distribution to each input, the probabilistic method firstly identifies all the potential probabilistic distributions of each input and the possibility of each distribution based on the available sparse data. Then it assigns the probabilistic distributions with the higher possibility to the inputs and calculates the sensitivity results. The probabilistic approach gives the most influential inputs and the possibility of each



input to be an influential input, which allows the modeler to account for the variability of the statistic information caused by sparse data.

## CHAPTER III PROGRESSIVE DAMAGE IN COMPOSITE

### 3.1 Introduction

The installation of fiber reinforced composite patches is a demonstrated approach to reinforce or repair metallic structures in engineering fields such as aerospace [6-8], marine [3, 9], automotive [10, 11] and infrastructure [12, 13]. Composite patches, bonded to metallic structures by adhesive or co-cured bonding methods [8, 14], effectively reinforce under-designed regions and restore the load carrying capacity to fatigue-cracked or corrosion-damaged parts. Uniform stress transfer, easy installation, customized stiffness, high specific strength, adaptability to the complex substrate, and excellent corrosion resistance [8] make bonded composite repairs an attractive alternative to traditional repair methods such as mechanically fastened metallic patches or structure replacement.

While composite patches offer many advantages, a primary concern when evaluating the damage tolerance of bonded composite patches is non-visible damage. Non-visible damage, located internally and often not identifiable without destructive inspection, can occur when the patch is subjected to general design loads or overloads during service, particularly bending stress [38-40] and low-velocity impact [41]. This non-visible damage can be present as disbond at the

interface between the patch and the metal substrate, delamination within the patch, fiber fracture or local buckling, and matrix cracking. Such damage might initially be minor but then propagate under additional loading and degrade patch performance. There is a considerable amount of prior research on the damage analysis of composite patches that focus on topics such as the fracture behavior of bonded metallic substrates [16, 19, 22-24] and disbond of adhesives [21, 29, 30]. Although progressive damage in composites has been widely investigated [31-37], few studies take into account the progressive failure of the entire hybrid (composite, bond line, and metal) structure, a necessary consideration when evaluating the structural performance of the patched structure. It has been demonstrated that the damage within the composite patch can substantially reduce the efficiency of the reinforcement or repair [42, 43]. Jones [42] also indicated that multiple failure modes, including cracking in the adhesive or at the adhesive-metal interface, fiber fracture, and delamination, should be evaluated when performing damage tolerance assessment. Therefore, it is necessary to consider multiple damage mechanisms, including the progressive failure of the composite patch and the interactions between the damage mechanisms when predicting damage initiation and propagation in the patched structure. To further complicate the investigation of damage tolerance in patched structure, varying boundary conditions and loading types are applied, each activating different combinations of damage mechanisms and in varying degrees. To accurately

predict the performance of composite patches for safe implementation, it is necessary to understand the dependence of damage mechanisms relative to in-situ conditions, capture progressive damage propagation, and identify the design parameters with the most influence on damage tolerance for each service loading requirement.

The objectives of this study are to: (1) develop a systematic approach to evaluate the damage tolerance of structures repaired with composite patches that includes multiple damage mechanisms, (2) develop a validated predictive finite element model, and (3) identify the most influential parameters on the damage tolerance of patched structure. This study encountered three main challenges, as shown in Fig. 3.1. Firstly, given the many choices of potential materials and configurations, the myriad of uncertainties involved, and the various loading conditions, it is not feasible to physically test every potential design. Secondly, a complex, high fidelity model is required to capture all of the interacting damage modes that contribute to energy absorption. Thirdly, the large number of inputs significantly increases the difficulty of identifying the most influential inputs on the damage tolerance of patched structure, as developing a validated surrogate model and performing sensitivity analysis becomes prohibitive.

To overcome these challenges, an integrated approach that combines computational simulation, experimental testing, and sensitivity analysis is

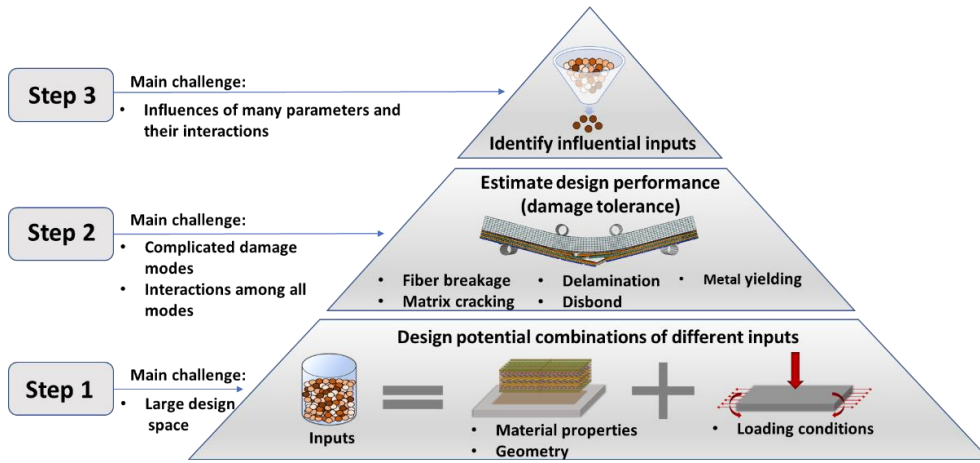


Figure 3. 1 The three main challenges to evaluate the damage tolerance of structures repaired with composite patches and to identify the most influential parameters.

performed, as shown in Fig. 3.2. A validated, high fidelity 3D finite element (FE) model that explicitly models each layer of the composite patch, the metallic substrate, and the interface has been developed to capture the progressive damage in the composite, disbond at the interface, and yielding in the metal. This model is evaluated under varying boundary conditions, material properties, and design configurations to map the damage mechanisms that contribute to patch failure throughout the design space. Sensitivity analysis is performed using computational simulation to identify the most influential design parameters on patch reliability providing essential knowledge critical to an efficient and high-quality patch design. This approach is demonstrated with the experimental, numerical, and sensitivity analysis of 5456 aluminum substrates co-cured to E-glass/epoxy composite patches.

## **3.2 Technical Approach**

### ***3.2.1 Experimental Testing***

Experimental testing is performed to investigate damage propagation under varying loading conditions and to obtain validation data to ensure the computational model is accurately capturing the physical behavior. Digital Imaging Correlation (DIC) is used to obtain high-resolution data on damage propagation and the strain field. Different testing configurations are designed to explore the capabilities of the model to predict different damage modes and their

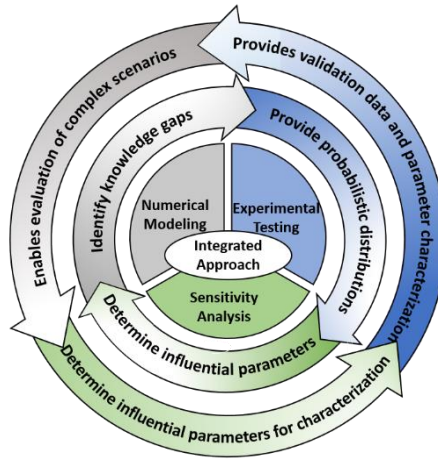
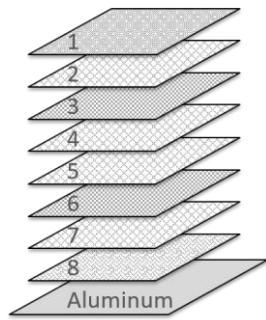


Figure 3. 2 The proposed approach integrates numerical modeling, experimental testing, and sensitivity analysis to produce validated numerical models and identify the most influential inputs based on the given model.

interactions in patched structures loaded in bending, a loading condition that activates multiple damage mechanisms as determined through preliminary testing.

An E-glass/epoxy composite patch is installed on a 0.25-inch thick 5456 aluminum plate using a hand lay-up procedure and vacuum infusion. The metal surface preparation is performed on the bonding side of the aluminum panel, following the application guide for AC-® 130 provided by the distributor, Advanced Chemistry & Technology. To obtain a quasi-isotropic laminate,  $\pm 45^\circ$  (Vectorply E-BX 1200) and  $0^\circ/90^\circ$  (Vectorply E-LT 1800) stitched fabrics are oriented according to the stacking sequence given in Fig. 3.3. A  $0^\circ/90^\circ$  plain weave ply (Hexcel 7500) is set first as the resin rich open ply while a  $0^\circ/90^\circ$  fine harness stain weave ply (Hexcel 7781) is used as the top ply to obtain a quality surface. The entire thickness of the composite patch laminate is 0.16 inch. The epoxy resin (M1002) is mixed with the curing agent, M2046 hardener, and spread on the fabrics layer by layer during the hand lay-up procedure. The composite patch is covered by the vacuum bag, with a P3 perforated film on the top of the composite patch to control the resin bleed rate. The vacuum level is set to 20 inHg for 3 hours and then the patch is cured in the oven at  $140^\circ$  F for 4 hours. Following the curing, the patched structure is cut into four-point bending specimens.



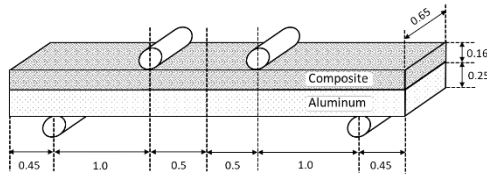


	E-glass Fabric	Fabrication Style
1	Hexcel 7781	0°/90° Satin weave
2	Vectorply E-BX 1200	±45° Stitch
3	Vectorply E-LT 1800	0°/90° Stitch
4	Vectorply E-BX 1200	±45° Stitch
5	Vectorply E-BX 1200	±45° Stitch
6	Vectorply E-LT 1800	0°/90° Stitch
7	Vectorply E-BX 1200	±45° Stitch
8	Hexcel 7500	0°/90° Plain weave

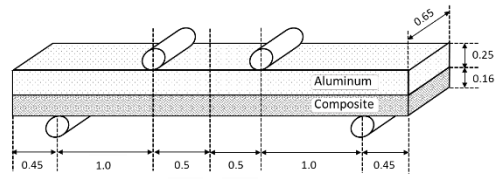
Figure 3. 3 Stacking sequence of E-glass/epoxy composite patch.

Four different specimen configurations, as shown in Fig. 3.4, are designed to investigate all damage modes, including fiber fracture, matrix cracking and delamination between plies in the composite patch, interface disbond, and yielding of aluminum. Three specimens are tested for each configuration. Specimen-A and B evaluate the composite patch under tension and compression respectively. Specimen-C and D with an initial notch in the aluminum substrate or the composite patch respectively, are designed to study the disbond at the interface between the composite patch and the aluminum plate. To avoid damage to the composite patch during the cutting process, a water jet machine is used to cut the specimens from the large patched panel. The notches of specimen-C and D are machined with a CNC machine. The front face of all the specimens is sprayed with a uniform thin white paint and then a black speckle pattern for the DIC measurements.

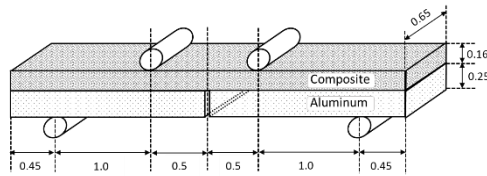
Four-point bending tests are performed on an MTS testing system that measures the loading force and displacement of the loading pins with the DIC system quantifying the real-time strain field of the specimen. The test configurations, as shown in Fig. 3.4, are designed using third point loading where the span of the loading pins on the top of the specimen is one-third of that of support pins at the bottom. The diameter of both the loading and support pins is 0.2 inch. All specimens are 3.9 inch long, 0.65 inch wide, and 0.41 inch thick. The loading rate of the MTS machine is 0.05 inch/min.



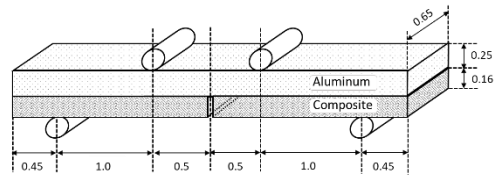
(a) Specimen-A



(b) Specimen-B



(c) Specimen-C



(d) Specimen-D

Figure 3. 4 Four different specimen configurations of the four-point bending test, all dimensions are in inches

### **3.2.2 Finite Element Modeling**

Performing physical experiments to carry out a comprehensive study that includes all variations of all design parameters and potential configurations is prohibitive due to time constraints and cost. Numerical modeling offers an alternative method to efficiently explore designs and investigate the effects of parameters on patch performance after validating a baseline model through experimental testing. Therefore, a high-fidelity 3D FE model, as shown in Fig. 3.5, is developed to capture the damage mechanisms under investigation. Each fabric layer is explicitly modeled, and cohesive elements are included between each layer to capture delamination between plies. The numerical simulations are executed in the FE code ABAQUS [78]. Laminae is individually modeled with continuum shell elements (SC8R), which discretize the entire three-dimension body instead of conventional shell elements to more accurately capture the through-thickness response. The CDM damage model of each laminae is implemented using a VUMAT user subroutine [79, 80]. Cohesive elements with a triangular traction-separation law integrated in ABAQUS are used to detect the interlaminar damage and are also included at the metal/patch interface to capture the patch disbond. The parameters of cohesive elements, including the stiffness, strength, and element size, are selected according to guidelines suggested by Turon [47]. The aluminum substrate is modeled with solid elements (C3D8R). as rigid bodies to create the boundary and loading conditions.

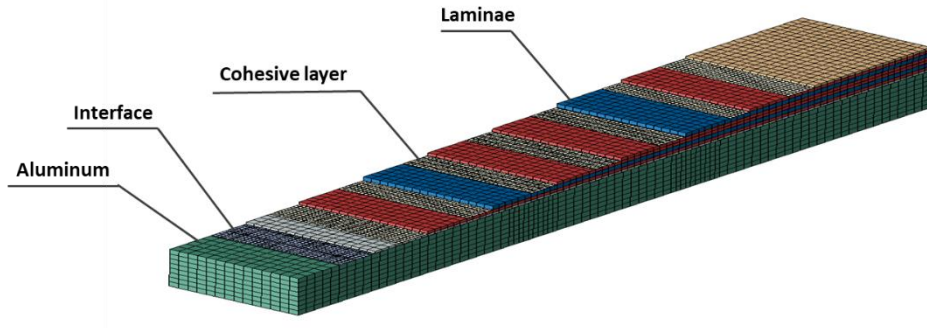


Figure 3. 5 The laminae, the cohesive layers, the interface, and the aluminum are modeled individually in the finite element model of the patched structure.

The load-displacement relations of the loading pins are calculated from the simulation results and compared with experimental data for the model validation. Energy absorption of the specimens measured for each damage mechanism is calculated and used to evaluate the influence of each damage type on patch failure for varying loading conditions and design parameters.

Damage modeling in the patched structure requires the interaction of different methodologies. The Continuum Damage Mechanics (CDM) is used to model the intralaminar damage, fiber fracture, and matrix cracking. The Cohesive Zone Method (CZM) is used to model the interlaminar damage (delamination) and the disbond of the interface between the composite patch and the aluminum. Plasticity is included as the only damage type in the aluminum. A preliminary FE investigation using Johnson-Cook damage modeling indicated zero change in results; therefore, damage modeling in the metal is not included in the study (although cracking in metal is another damage mode that should be included in a general analysis of patched structure). Additionally, no damage was observed in the metal during experimental testing other than plastic deformation.

#### *3.2.2.1 CDM for Intralaminar Damage*

The CDM approach has been extensively studied to predict composite failure modes, especially in investigations of impact damage modeling. The CDM enables an easy integration of stress or strain failure criteria and fracture mechanics. The stress or strain failure criteria predict damage initiation and the

fracture mechanics approach captures damage evolution by correlating the damage variables to fracture energy.

The load carrying capacity of composites progressively degrades due to the accumulation of microfiber/matrix cracks and the plasticity of the matrix prior to ultimate failure. To quantify damage at the macro scale caused by microcracks, the CDM describes the degradation of material properties. The CDM uses the damage variables to gradually reduce the material stiffness. Each laminae is modeled as a homogeneous orthotropic material. The elastic damage model is utilized for fiber dominated tensile or compressive failure while the elastic-plastic damage model is applied for matrix-controlled shear failure.

Constitutive equations for laminae with damage variables in the elastic domain are considered in plane-stress and take the form:

$$\begin{bmatrix} \varepsilon_{11}^e \\ \varepsilon_{22}^e \\ \varepsilon_{12}^e \end{bmatrix} = \begin{bmatrix} \frac{1}{(1-d_{11})E_{11}} & \frac{-\nu_{12}}{E_{11}} & 0 \\ \frac{-\nu_{21}}{E_{22}} & \frac{1}{(1-d_{22})E_{22}} & 0 \\ 0 & 0 & \frac{1}{(1-d_{12})2G_{12}} \end{bmatrix} \begin{bmatrix} \sigma_{11} \\ \sigma_{22} \\ \sigma_{12} \end{bmatrix}, \quad (3.1)$$

$$d_{11}, d_{22}, d_{12} \in [0, 1]$$

where  $d_{11}$  and  $d_{22}$  are damage variables responding to fiber fracture along the 11 and 22 directions,  $d_{12}$  is the damage variable associated with matrix deterioration in shear deformation as shown in Fig. 3.6. To distinguish between tensile and compressive fiber failures,  $d_{11}$  and  $d_{22}$  are defined in the form:

$$d_{11} = d_{11}^t \frac{\langle \sigma_{11} \rangle}{|\sigma_{11}|} + d_{11}^c \frac{\langle -\sigma_{11} \rangle}{|\sigma_{11}|}, \quad d_{22} = d_{22}^t \frac{\langle \sigma_{22} \rangle}{|\sigma_{22}|} + d_{22}^c \frac{\langle -\sigma_{22} \rangle}{|\sigma_{22}|} \quad (3.2)$$

$$\langle x \rangle = \begin{cases} 0, & x < 0 \\ x, & x > 0 \end{cases}$$

where  $d_{11}^t, d_{11}^c$  are components of  $d_{11}$ , related to fiber fracture under tensile and compressive loading, respectively. Though the constitutive equations (Eq. 3.1) based on the stiffness decay model is straightforward to describe the material degradation, the concept of effective stress from the strain equivalence theory is generally applied to present the constitutive model as

$$\begin{bmatrix} \varepsilon_{11} \\ \varepsilon_{22} \\ \varepsilon_{12}^e \end{bmatrix} = \begin{bmatrix} \frac{1}{E_{11}} & \frac{-\nu_{12}}{E_{11}} & 0 \\ \frac{-\nu_{21}}{E_{22}} & \frac{1}{E_{22}} & 0 \\ 0 & 0 & \frac{1}{2G_{12}} \end{bmatrix} \begin{bmatrix} \bar{\sigma}_{11} \\ \bar{\sigma}_{22} \\ \bar{\sigma}_{12} \end{bmatrix}, \quad \begin{bmatrix} \bar{\sigma}_{11} \\ \bar{\sigma}_{22} \\ \bar{\sigma}_{12} \end{bmatrix} = \begin{bmatrix} \frac{\sigma_{11}}{(1-d_{11})} \\ \frac{\sigma_{22}}{(1-d_{11})} \\ \frac{\sigma_{12}}{(1-d_{12})} \end{bmatrix} \quad (3.3)$$

The effective stress,  $\bar{\sigma}$ , is defined as the stress on undamaged material responding to the same strain on damaged material caused by the nominal stress,  $\sigma$ . The effective stress provides a direct approach to define the damage initiation criteria and damage evolution. The damage is initiated once the effective stress reaches the value of material strength (Eq. 3.4).

$$\frac{\bar{\sigma}_{ij}}{X_{ij}} = 1, \quad i, j = 1, 2 \quad (3.4)$$

$X_{11}$  and  $X_{22}$  are the tensile or compressive strength for uniaxial loading along the fiber direction and  $X_{12}$  is the shear strength. After the initiation of damage, the evolution of  $d_{11}$  and  $d_{22}$  is described by the exponential equation (Eq. 3.5)



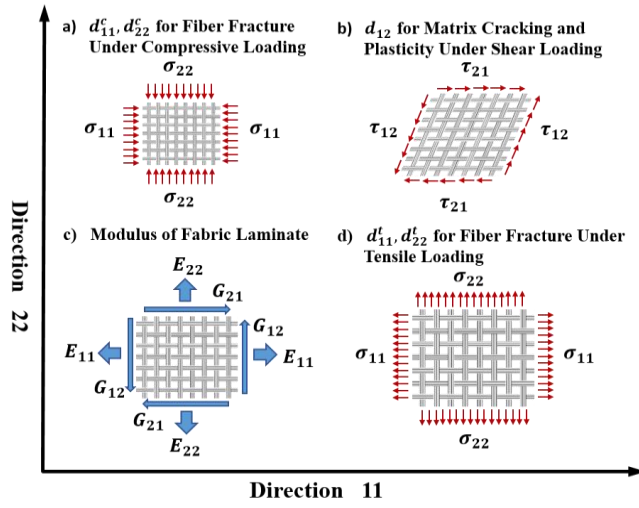


Figure 3. 6 Damage variables used to model degradation of fabric reinforced laminae under different loading.

$$d_{ii} = 1 - \frac{1}{k_{ii}} \exp \left\{ -\frac{2U_0^{ii}L_c}{G_{ii}^f - U_0^{ii}L_c} (k_{ii} - 1) \right\} \quad i = 1,2 \quad (3.5)$$

$$k_{ii} = \frac{\bar{\sigma}_{ii}}{X_{ii}}, \quad U_0^{ii} = \frac{X_{ii}^2}{2E_{ii}}$$

where  $G_{ii}^f$  is the fracture energy of the laminae in the  $ii$  direction,  $U_0^{ii}$  is the elastic energy density when damage is initiated and  $L_c$  is the characteristic length of the element. To ensure the nondecreasing behavior of  $d_{11}$  and  $d_{22}$ ,  $L_c$  needs to satisfy the following requirement (Eq. 3.6).

$$G_{ii}^f - U_0^{ii}L_c > 0 \quad (3.6)$$

Therefore, the element size should be small enough to meet this requirement when implementing the damage evolution (Eq. 3.5) in finite element analysis.

Different from  $d_{11}$  and  $d_{22}$ , the evolution of  $d_{12}$  is described using the equation (Eq. 3.7) linear in  $\ln(k_{12})$ ,

$$d_{12} = \alpha_{12} \ln(k_{12}), \quad k_{12} = \frac{\bar{\sigma}_{12}}{X_{12}} \quad (3.7)$$

where  $\alpha$  is a material constant which is measured by experimental testing and discussed later in the section of determination of material properties.

In addition to the elastic response above, plasticity behavior appears in fabric laminae under shear loading, which is described by the Ludwik-Hollomon [81] equation (Eq. 3.8),

$$\bar{\sigma}_{12} = \tilde{\sigma}_y + C(\varepsilon_{12}^p)^P, \quad \varepsilon_{12}^p = \varepsilon_{12} - \varepsilon_{12}^e \quad (3.8)$$

where  $\tilde{\sigma}_y$  is the effective stress corresponding to the normal stress at the yield point,  $\varepsilon_{12}^p$  is the plastic part of the total strain  $\varepsilon_{12}$ ,  $C$  and  $P$  are material properties. The laminae fails when the plastic strain reaches a maximum value  $\varepsilon_{max}^{pl}$ .

### 3.2.2.2 CZM for Delamination and Disbond

The CDM presented above is for in-plane damage, which is aimed solely at predicting damage within individual laminae of the composite patch such as fiber fracture and matrix cracking. For out-of-plane damage, CZM is applied to model the delamination between plies and the disbond at the composite/metal interface.

The triangular traction-separation law (Fig. 3.8) is selected because of its simple constitutive equations (Eq. 3.9) and widespread use [82]. Results have been demonstrated to be relatively invariant with respect to the shape of the traction-separation curve [41], and the triangular shape was able to accurately predict separation damage for this study.

$$\begin{cases} t = K\delta, & t \leq t^0 \\ t = \frac{t^0(\delta - \delta^f)}{\delta^0 - \delta^f}, & t > t^0 \end{cases} \quad (3.9)$$

where  $t$  is the traction,  $\delta$  is the separation,  $K$  is the interface stiffness relating the traction and corresponding separation before the initiation of the damage,  $t^0$  is damage initiation stress,  $\delta^0$  is the separation where the damage initiates, and  $\delta^f$  is the maximum separation where the element totally fails. The critical fracture energy  $G_c$  has the same value as the shaded area under the triangle in Fig. 7.  $G_c$

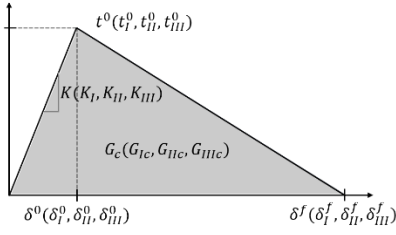


Figure 3. 7 Triangular traction-separation law of the CZM.

is directly measured from experimental results while  $t^0, K$  and  $\delta^f$  are obtained by empirically fitting to the experimental data.

To predict the delamination in the composite patch resulting from mixed

$$\left\{ \frac{t_I}{t_I^0} \right\}^2 + \left\{ \frac{t_{II}}{t_{II}^0} \right\}^2 + \left\{ \frac{t_{III}}{t_{III}^0} \right\}^2 = 1 \quad (3.10)$$

mode fracture, the quadratic stress criterion (Eq. 3.10) is used to determine the damage initiation and evolution,

where  $t_I, t_{II}, t_{III}$  are tractions for Mode I, Mode II and Mode III fracture  $t_I^0, t_{II}^0, t_{III}^0$  are the damage initiation stresses for the three modes of fracture. Damage initiates when the left part of Eq. 3.10 is equal to unity.

The equation proposed by Benzeggagh and Kenane [83], one of the most widely used expressions for the critical energy release rate of a mixed-mode loading situation, is used as the mixed mode fracture criterion (Eq. 3.11).

$$G_c = G_{Ic} + (G_{IIc} - G_{Ic}) \left( \frac{G_{II} + G_{III}}{G_I + G_{II} + G_{III}} \right)^\eta \quad (3.11)$$

where  $G_{Ic}$  and  $G_{IIc}$  are the critical energy release rates for Mode I and Mode II fracture,  $G_I, G_{II}$  and  $G_{III}$  are energy release rate for the three modes of fracture,  $\eta$  is a material property measured by experimental testing, and  $G_c$  is the critical energy release rate for mixed-mode fracture.

### 3.2.3 Sensitivity Analysis

Although numerical modeling accelerates patch design by enabling exploration of varying material selections and configurations in a feasible amount

of time, the large number of design parameters required for optimization of a composite patch structure remains challenging even when using high-performance computing (HPC). Sensitivity analysis provides a screening method to limit the design space by identifying and eliminating the non-influential parameters on patch performance. Design optimization is then performed using only the parameters that are determined to be influential on structural performance. Additionally, sensitivity analysis results inform the quality of data needed for each of the parameters. Highly influential parameters should be fully characterized and held to tight tolerances while parameters with little effect on performance can be defined with average values.

#### *3.2.3.1 Data Quality of the Input Parameters*

The input parameter values are obtained from different data sources and have varying data quality. Some data was obtained from comprehensive test programs while other parameter data was approximated using literature values for similar materials. In some cases, data were sparse for a given parameter, and data may have been collected from disparate sources. Rather than unnecessarily performing comprehensive and potentially costly and time-consuming experimental testing for every parameter, the results of the sensitivity analysis inform focused characterization of the most influential parameters. If a parameter is highly influential and based on low-quality data, it should be fully characterized and specified with tight tolerances. As shown in Table 1, the

parameter values in this study are obtained from four different types of data sources: experimental testing, manufacturer data, estimation from similar materials in the literature, and empirically fitting data. The properties measured from experimental testing are considered as high-quality data. The properties estimated from the manufacturer datasheet and literature are considered as neutral quality data. The properties obtained from empirically fitting the modeling results to the experimental observations are taken as bad quality data. The parameters defined using data classified as bad or neutral quality are candidates for more rigorous characterization if the sensitivity analysis identifies the parameter as highly influential. A detailed description of the material models and parameter definitions are now discussed, and the parameter values are given in Table 3.2.

The elastic-plastic properties of the aluminum are determined from cylindrical tensile testing, as shown in Table 1. The Ludwik-Hollomon [81] equation (Eq. 3.17) is used to describe the strain hardening phenomenon,

$$\sigma = \sigma_y + K(\varepsilon_p)^n \quad (3.17)$$

where  $\sigma$  is the stress,  $\sigma_y$  is the yield stress,  $\varepsilon_p$  is the plastic strain,  $K$  and  $n$  are material properties.

The properties of each type of laminae (each reinforced with a different fabric type) are either obtained from experimental test results, provided by the manufacturer, or estimated from properties of similar materials in the literature.

Due to the lack of shear property data, four laminae layers consisting of different fabric types are assigned the same shear properties. The assumption is made based on the fact that the four different laminae have the same matrix which dominates the laminae shear properties.

DCB and ENF tests on Hexcel 7500 reinforced epoxy laminates are used to determine the interlaminar properties (tests are performed by the Carderock Division of Naval Surface Warfare Center in accordance with ASTM D5528, and ASTM D7905). The intralaminar fracture toughness of Hexcel laminae is estimated from the stress intensity factor of a similar E-glass/Epoxy weave fabric, which is measured by Mandell et al. [84] using a double edge notched specimen. The intralaminar fracture toughness of E-BX/E-LT is estimated from a double edge notched fracture test [85] of the [90/0]<sub>s</sub> E-glass/epoxy composite. Using the technique and procedure employed by Johnson [79], the shear properties are derived from the glass/Epoxy cyclic stress-strain curves from Johnson's [79] 45° tension test.

### *3.2.3.2 Parameter Evaluation*

The elementary effects method (EEM) was chosen as a viable method for the sensitivity analysis, given the number of parameters and computational time (about 60 total CPU hours per analysis). Although other methods such as the variance-based method (VBM) can generally provide better measurements for prioritizing parameters and screening out negligible inputs, the computational



cost of this method was infeasible for the present study. For example, in this investigation the number of design parameters was limited to 41, if only 3 values are considered (low, mean, and high) for each parameter then  $3^{41}$  high fidelity FE models must be analyzed equating to  $3^{44}$  computing hours to sample the design space. Given the variation in damage tolerance due to the rapidly varying contributions of the multiple damage mechanisms, this limited sampling is not adequate to capture damage tolerance behavior between sample points and a much more heavily populated sample set is needed for VBM. The computational burden to populate this sample set was found to be infeasible even when employing sampling methods such as Latin Hypercube or Latin Stratified sampling methods [86, 87].

The EEM is an effective alternative to reduce the computational burden while providing reasonable results. The EEM [88] is a derivative-based approach, similar to the One-Factor-at-a-time (OFAT) method [89]. However, the EEM overcomes the OFAT's limitations by averaging local measures from a minimal number of properly distributed sample points. The reduced number of required sample points makes the EEM more feasible than the VBM in this case, where simulations are computationally expensive and the investigation of a large number of parameters is required. Although the EEM is not able to estimate the effects of interactions between certain parameters as with the VBM, the EEM can

Table 3. 1 The data quality of the main parameters included in the FE model

Material	Material Properties from Different Data Source		
	High Quality	Neutral Quality	Poor Quality
Aluminum	$E, \nu, \sigma_y, K, n$	--	--
E-LT 1800 laminae	--	$E_{1800}, \nu_{1800}, X_{T1800}$	$G_{1800}^f$
Hexcel 7781 laminae	--	$E_{7781}, \nu_{7781}, X_{T7781}, G_{7781}^f$	--
Interlaminar	$E_{coh}, X_{Tcoh}, X_{Scoh}, G_{Icoh}^f, G_{IIcoh}^f, BK_{coh}$	--	--
E-BX 1200 laminae	--	$E_{1200}, \nu_{1200}, X_{T1200}$	$G_{1200}^f$
Hexcel 7500 laminae	$E_{7500}, \nu_{7500}, X_{T7500}$	$G_{7500}^f$	--
Laminar shear	--	$G_{12}, X_{12}, \alpha_{12}, d_{12}, \bar{\sigma}_y, C, P$	$\epsilon_{max}^{pl}$
Composite / Al interface	$E_{int}$	$X_{Tint}, X_{Sint}, G_{Iint}^f, G_{IIint}^f, BK_{int}$	N/A

Table 3. 2 The values of the FE model parameters considered in the sensitivity analysis

$E = 1.1E + 07$	$\nu = 0.29$	$\sigma_y = 3E + 04$	$K = 1E + 04$
$n = 0.607$	$E_{1800} = 2.8E + 06$	$\nu_{1800} = 0.15$	$X_{T1800} = 5.3E + 04$
$G_{1800}^f = 150$	$E_{7781} = 4.4E + 06$	$\nu_{7781} = 0.15$	$X_{T7781} = 7.0E + 04$
$G_{7781}^f = 100$	$E_{1200} = 2.8E + 06$	$\nu_{1200} = 0.15$	$X_{T1200} = 5.3E + 04$
$G_{1200}^f = 150$	$E_{7500} = 2.8E + 06$	$\nu_{7500} = 0.15$	$X_{T7500} = 4.7E + 04$
$G_{7500}^f = 100$	$E_{coh} = 6.2E + 05$	$X_{Tcoh} = 7.6E + 03$	$X_{Scoh} = 4.9E + 03$
$G_{Icoh}^f = 7.6$	$G_{IIcoh}^f = 16.6$	$BK_{coh} = 2.6$	$G_{12} = 8.0E + 05$
$X_{12} = 5.2E + 03$	$\alpha_{12} = 0.28$	$d_{12} = 0.72$	$\bar{\sigma}_y = 5.2E + 03$
$C = 6.5E + 05$	$P = 0.729$	$\epsilon_{max}^{pl} = 0.02$	$E_{int} = 6.2E + 05$
$X_{Tint} = 1.5E + 04$	$X_{Sint} = 9.8E + 03$	$G_{Iint}^f = 7.6$	$G_{IIint}^f = 16.6$
$BK_{int} = 2.6$			

provide similar sensitivity information (overall effects and interactions) as the first order and total indices that are generally estimated in VBM. To calculate the elementary effect of a model with  $k$  inputs, the inputs are normalized as (Eq. 3.12)

$$X_i = \frac{X_i - X_{imin}}{X_{imax} - X_{imin}}, \quad i = 1, 2, 3 \dots, k \quad (3.12)$$

where  $X_{imin}$  and  $X_{imax}$  are the minimum and maximum of the  $i$ th input. Each unit input is discretized into a  $p$ -level grid producing  $(p - 1)^k$  points as the sample source. Then the elementary effect of the  $i$ th input parameter at  $\mathbf{X} =$

$(X_1, X_2, \dots, X_{i-1}, X_i, \dots, X_k)$  is defined as (Eq. 13)

$$EE_i = \frac{Y(X_1, X_2, \dots, X_{i-1}, X_i + \Delta, \dots, X_k) - Y(X_1, X_2, \dots, X_{i-1}, X_i, \dots, X_k)}{\Delta}, \quad \Delta \in \left\{ \frac{1}{p-1}, \dots, 1 - \frac{1}{p-1} \right\} \quad (3.13)$$

where  $\mathbf{X}$  is any selected sample point within the parameters space and  $Y$  the corresponding output. Morris [88] proposed to calculate the  $EE_i$  values at well-designed sample points and estimate the sensitivity information with the mean,  $\mu$ , and standard deviation,  $\sigma$ , of the  $EE_i$  values. A high  $\mu$  value generally means a large overall effect of the input on the output. A high  $\sigma$  value indicates a high nonlinearity or many interactions with other inputs. Morris also recommended an efficient sample points design with the trajectory concept. A trajectory contains  $k + 1$  sample points. The first point  $\mathbf{X}^1$  is randomly selected from the sample source. The second point  $\mathbf{X}^2$  is generated based on the first one by increasing or decreasing the  $i$ th component of  $\mathbf{X}^1$  by  $\Delta$  where  $i$  is randomly chosen from the set  $\{1, 2, \dots, k\}$ . The third point  $\mathbf{X}^3$  is generated based on the second one by

increasing or decreasing the  $j$ th component of  $X^2$  by  $\Delta$  where  $j$  is randomly chosen from the set  $\{1, 2, \dots, k\}$  and  $j \neq i$ . Likewise, until the  $(k + 1)$ th point. The trajectory of  $k + 1$  points can produce one elementary effect for each input. The  $\mu$  and  $\sigma$  can be calculated from  $r$  trajectories as (Eq. 3.14,3.15)

$$\mu_i = \frac{1}{r} \sum_{j=1}^r EE_i^j \quad (3.14)$$

$$\sigma_i = \sqrt{\frac{1}{r-1} \sum_{j=1}^r (EE_i^j - \mu_i)^2} \quad (3.15)$$

where  $EE_i^j$  is the elementary effect of the  $i$ th input estimated from the  $j$ th trajectory. Campolongo et al. [90] replaced the usage of  $\mu$  with  $\mu^*$  (Eq. 3.16), which is the mean of the absolute values of  $EE_i$ .

$$\mu_i^* = \frac{1}{r} \sum_{j=1}^r |EE_i^j| \quad (3.16)$$

Because the mean,  $\mu$ , could potentially be a small value resulting from the cancellation of large positive and negative  $EE_i$  values, the use of  $\mu^*$  can avoid this misrepresentation of highly influential parameters and better identify the most influential inputs. In this study, all three measurements  $\mu$ ,  $\mu^*$  and  $\sigma$  are estimated as the calculation of both  $\mu$  and  $\mu^*$  comes at no extra computational cost. The comparison between  $\mu$  and  $\mu^*$  can also provide additional sensitivity information as discussed in the following section. Following Campolongo and Saltelli [91, 92], ten trajectories are used for the sensitivity analysis.

### **3.3 Results and Discussions**

#### ***3.3.1 Comparison Between Experimental Results and Computational Simulation***

The four different types of specimens presented multiple damage mechanisms contributing to varying degrees to the total energy absorbed by the patched structure. Fig. 3.8 shows representative examples of damage progression for each of the four configurations, including the sequential strain fields of the intact specimens, damage initiation, damage evolution, and failure as well as the simulation results at failure. The load-displacement curves calculated from FE models are also compared with the experimentally obtained results in Fig. 3.9 for the four different specimen configurations. The simulation results quantitatively and qualitatively capture the experimental results reasonably well.

Damage in specimen-A initiates at the site having the maximum shear force and moment in the form of interlaminar delamination. Due to the symmetry of the geometry, the damage should theoretically initiate simultaneously at both sites under the loading pins. However, microstructure variation due to inherent variability between specimens such as air voids, inclusions, and mechanical properties at the two sites causes initiation at one site to dominate failure. For the specimen shown in Fig. 3.8(a), the damage initiates on the left side and then propagates to a failure-inducing interlaminar delamination in the composite patch rather than a disbond at the interface between composite and aluminum. To

initiate damage in the FE analysis, a small area at the initiation site on one side is assigned with lower strength cohesive elements to simulate the material asymmetry. Fig. 3.9(a) shows that the simulation correctly predicts load drop due to the delamination and the maximum load compared with the experimental results.

Specimen-B shows large areas of intralaminar damage and interlaminar delamination. The top layer of the composite patch (layer 1 in Fig. 3.3) fails first in the form of fiber fracture and delamination due to the presence of maximum tensile stress. Then the fracture and delamination of other layers in the composite patch followed one-by-one, as shown in Fig. 3.8(b). For the load-displacement curve of specimen-B in Fig. 3.9(b), the model captures the progressive damage behavior of the composite patch. The first load peak  $P_1$  is related to the intralaminar fracture delamination of the first layer (Layer 1). As shown in the visualization of the simulation result, the shear failure of the two  $\pm 45^\circ$  oriented E-BX 1200 laminae (Layer 4 and 5) causes the sudden drop of the load after the second load peak  $P_2$ , which indicates that the load carrying capacity between  $P_1$  and  $P_2$  mainly depends on the shear properties of the laminae which is governed by the resin.

Interlaminar delamination is again observed in specimen-C at the same layer as in specimen-A. When comparing the picture of specimen-C in Fig.3.8, it is clear that specimen-C exhibits minimal plastic deformation, because the

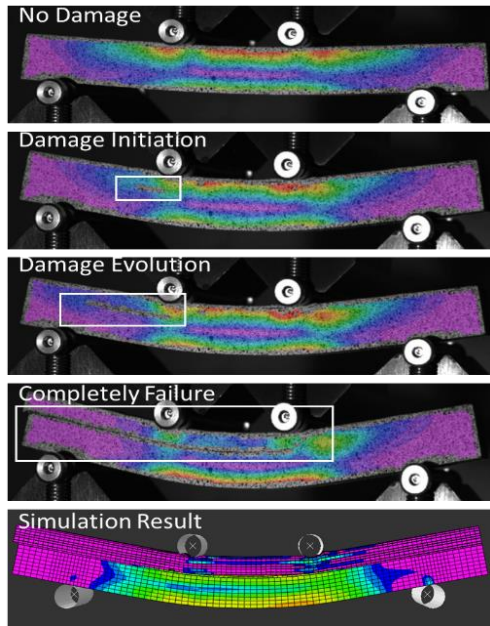
composite patch, which presents a more brittle nature, becomes the main load-bearing component. The damage area in specimen-C is much smaller than that in specimen-A since the notch in aluminum reduces the flexural stiffness of the patched structure and subsequently the stress of the specimen.

Interface disbond dominates in specimen-D while there's no disbond appearing specimen-C, as shown in Fig. 3.8. Specimen-D is able to produce a higher disbond stress as the unnotched part in specimen-D (aluminum) is much tougher than that in specimen-C (composite).

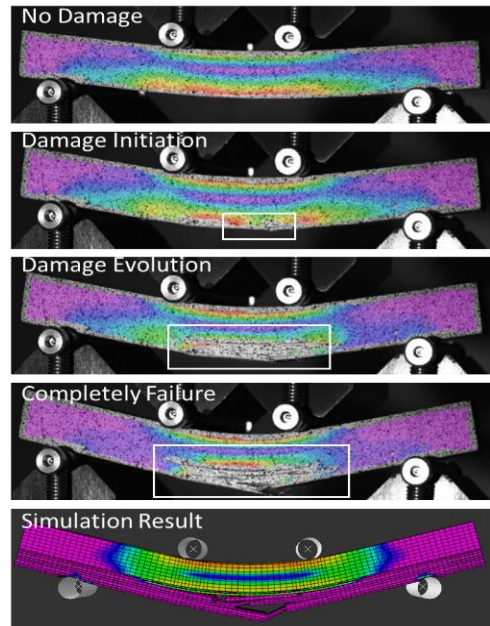
The simulated load-CMOD curves of specimen-A, B exhibit better quantitative comparison with the experimental results than that of specimen-C, D. This might be caused by the fact the stress concentration area of specimen-C, D is near the composite/aluminum interface and the interfacial properties used in the FE model are not of high quality. Moreover, the CNC machined initial notches in specimen-C, D can potentially result in some damage in the composite and interface near the machining area and that damage is not considered in the FE models.

### ***3.3.2 Distribution of the Energy Absorption***

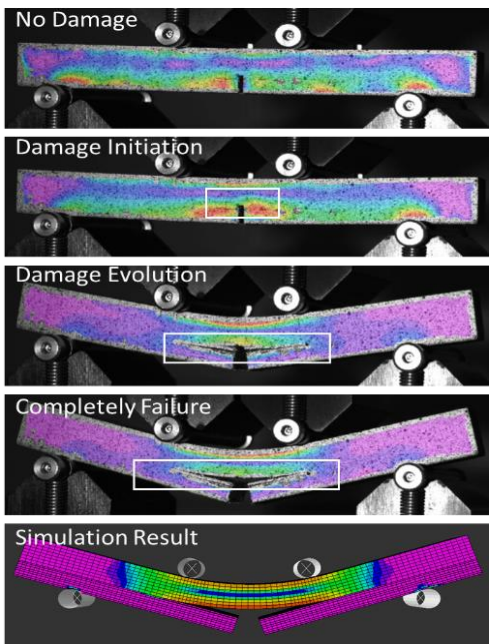
The energy absorbed by the patched structure is calculated from the FE results. The mechanisms capable of absorbing energy include the plastic deformation in aluminum, shear plasticity in laminae, the intralaminar fracture of



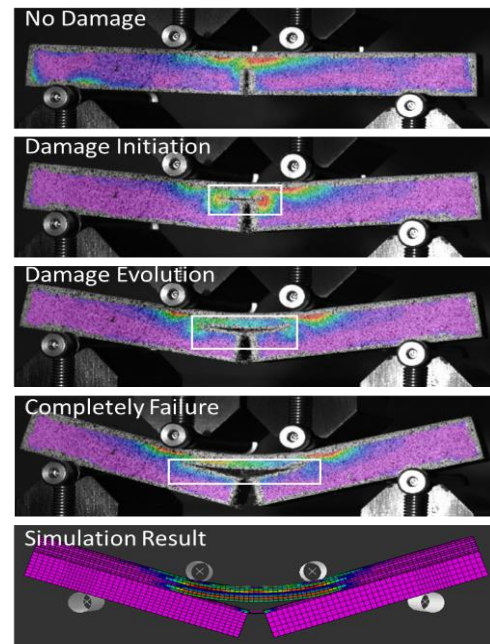
(a) Specimen-A



(b) Specimen-B



(c) Specimen-C



(d) Specimen-D

Figure 3. 8 Damage propagation of four-point bending specimens recorded with DIC, the white box indicates damage area and the corresponding simulation results at failure



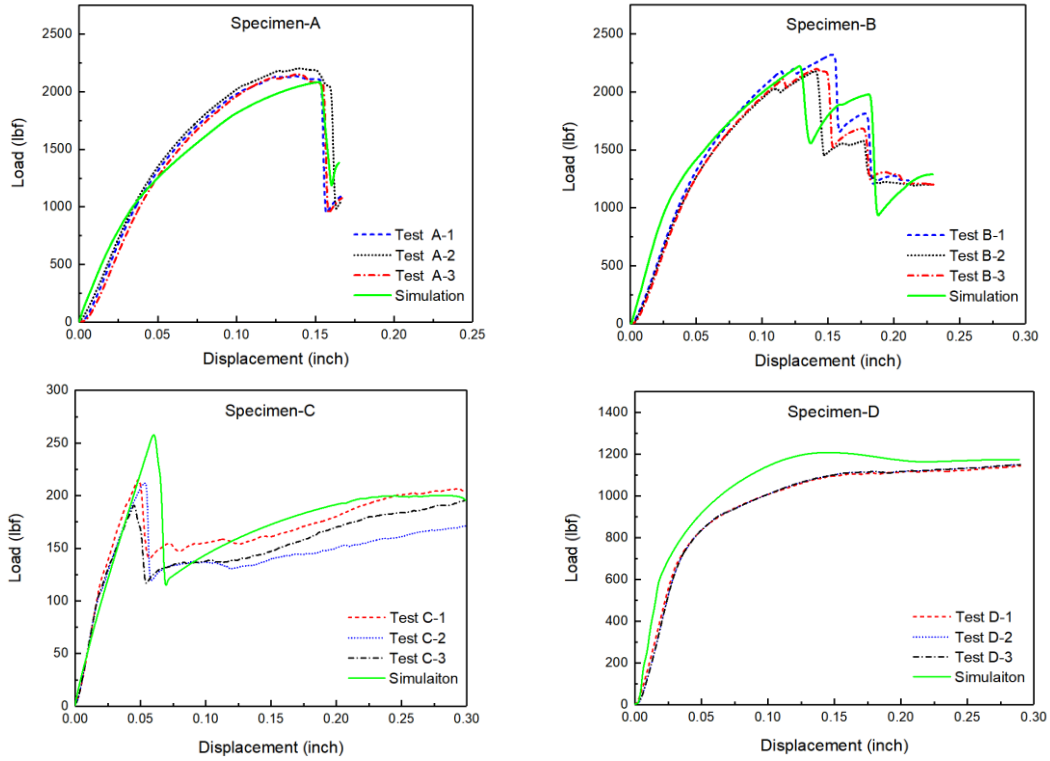


Figure 3. 9 Comparison between the displacement-load curve from simulation and experimental test for different specimen configurations.

the laminae, delamination within the patch and disbond at the interface. The contributions of the different damage mechanisms to the final energy absorption are calculated, as shown in Fig. 3.10. As per the design of experiments, the different specimen configurations exhibit significant differences in the energy absorption distributions. The pie chart of specimen-A shows more than two-thirds of the total absorbed energy is from the plasticity in the aluminum and the rest is from the delamination and plasticity in the laminae. Specimen-B shows a similar distribution as specimen-A except for presenting a small amount of energy from the fracture of the laminae. Since specimen-A, B are essentially the same type of specimen, it can be concluded that different loading conditions can initiate different damage mechanisms.

For specimen-C, the loading condition is the same as specimen-A, but the energy is only absorbed by the composite patch compared against specimen-A. The notch in the aluminum makes the composite patch the main bearing component. Likewise, the notch in the composite makes the aluminum the main bearing component in specimen-D and most of the energy is absorbed by the aluminum. The difference between specimen-A and C or specimen-B and D shows the preexisting damage in the patched structure significantly changes the energy absorption distribution. According to the pie charts of specimen-A and B, although the composite patch is much more brittle than the aluminum, it contributes about one-third of the total energy absorbed. As depicted in Fig.

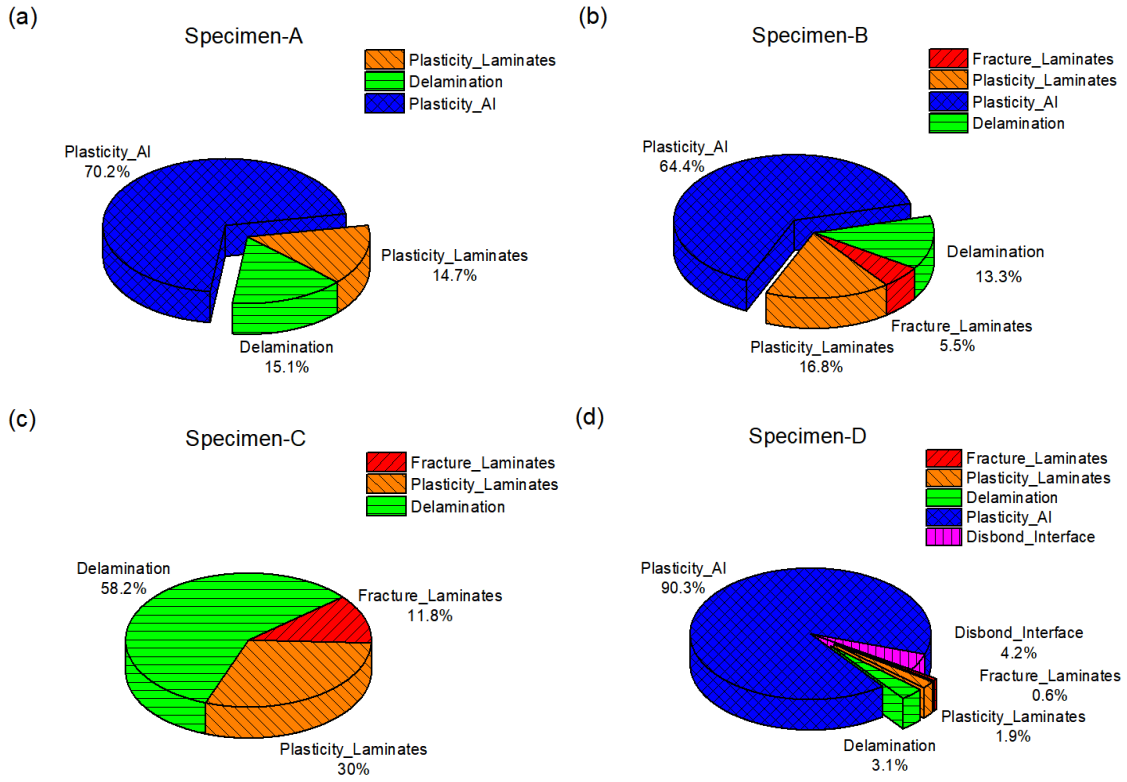


Figure 3. 10 The final energy absorption distribution calculated from the models of different specimens for different mechanisms.

3.10, the shear plasticity of laminae and interlaminar delamination are the two main mechanisms in the patch that absorb the highest amount of energy. These mechanisms are governed by the matrix properties of the composite. Hence, the selection of the matrix material is an important criterion when designing patched structure to maximize energy absorption.

### **3.3.3 Sensitivity Analysis Results**

Because specimen-B exhibits the most damage mechanisms when compared with the other three specimen types, this configuration is used to demonstrate the sensitivity analysis to select the most influential parameters on the energy absorption of the patched structure. The total energy absorption is used as an output for sensitivity analysis, as well as the energy absorption of each of the individual damage mechanisms. Although there is no disbond in the baseline evaluation of specimen-B, varying the material properties does initiate disbond in some of the FE models.

Generally,  $\mu^* - \sigma$  and  $\mu^* - \mu$  plots are presented to depict the sensitivity information obtained with the EEM. In the  $\mu^* - \sigma$  plot, the ranking provided by  $\mu^*$  shows the overall influence of the inputs on the output and the ranking provided by  $\sigma$  along indicates the ensemble of the input's higher order effects such as nonlinearity and interactions within other inputs. Although  $\mu^*$  offers a more reliable ranking compared with  $\mu$ , it loses the information relative to the sign of the effect. Therefore, a  $\mu^* - \mu$  plot with two reference lines ( $\mu^* = \pm\mu$ ) is displayed

to show the sign of the inputs' influence on the output. The sign of the effects can be estimated based on the distance between the input and the reference lines. If the input is on the line  $\mu^* = \mu$ , the effect of the input is monotonically increasing. If input is on  $\mu^* = -\mu$ , the effect of the input is monotonically decreasing. Inputs near the  $\mu^* = -\mu$  suggest the sign of the effects are mostly negative. Likewise, inputs near the line  $\mu^* = \mu$  are mostly positive.

Investigations begin by evaluating the total energy absorbed by the patch, the metal, and the entire hybrid system. The  $\mu^* - \sigma$  plot for the damage within the patch in Fig. 3.11(a) shows there is no clear-cut boundary to define which inputs are most influential, as the inputs are widely spread along the  $\mu^*$  axis, especially the inputs with  $\mu^*$  smaller than nine. However, the ten most important and ten least important inputs are identified and can be used as a preliminary parameter set when performing design and model optimization. Three of the ten most influential inputs are the material properties of the first layer of the composite patch,  $G_{7781}^f, E_{7781}, \nu_{7781}$  indicating that the integrity of this Hexcel 7781 laminae is essential to allow the patch to undergo plastic damage which plays an important role in energy absorption as shown in Fig. 3.10(b). The ten least important inputs have smaller  $\mu^*$  values and can be set as constant parameter values using reasonable estimations. Figure. 3.11(a) also shows that most inputs with high  $\mu^*$  values have large  $\sigma$  values which implies the inputs have high nonlinearity or many interactions with other inputs. The ten most influential inputs

determined by  $\mu^*$  are labeled in the  $\mu^* - \mu$  plot as shown in Fig. 3.11(b). In this plot, the inputs  $\alpha_{12}$  and  $v_{7781}$  near the dashed line suggest the sign of the effects are mostly negative. Likewise,  $X_{12}$  near the solid line is mostly positive. The input  $G_{7781}^f$  is estimated to present a large  $\mu^*$  and a  $\mu$  close to zero, which means the effects with opposite signs cancel each other out when calculating  $\mu$ . The  $\mu^* - \mu$  plot shows the advantage of using  $\mu^*$  since some of the important inputs could be missed such as  $\alpha_{12}$  and  $v_{7781}$  when only investigating  $\mu$ .

For the plasticity absorption in the aluminum, as expected, the most important inputs are the aluminum's properties as depicted in Fig. 3.11(c). The Young's modulus  $E$  and the yield strength  $\sigma_y$  of the aluminum are determined to have larger  $\mu^*$  values compared against the other inputs. Among the ten most important inputs for the plasticity in the aluminum, three inputs are related to the shear properties of the laminae  $G_{12}$ ,  $\alpha_{12}$  and  $P$ . This suggests the shear plasticity in the patch contributes significantly to reinforce the energy absorption capability of the aluminum. Figure 3.11(d) shows the most influential inputs  $E$  and  $\sigma_y$  have  $\mu$  values close to zero, which further demonstrates the benefit of evaluating parameter sensitivity based on  $\mu^*$ .

The sensitivity measures of the energy absorption due to all the damage mechanisms are depicted in Fig. 3.11(e)(f). As summarized in Table 3.3, the ten most important inputs include the two most important  $E$  and  $\sigma_y$  for the plastic energy absorption in the aluminum and eight of the most influential for the plastic

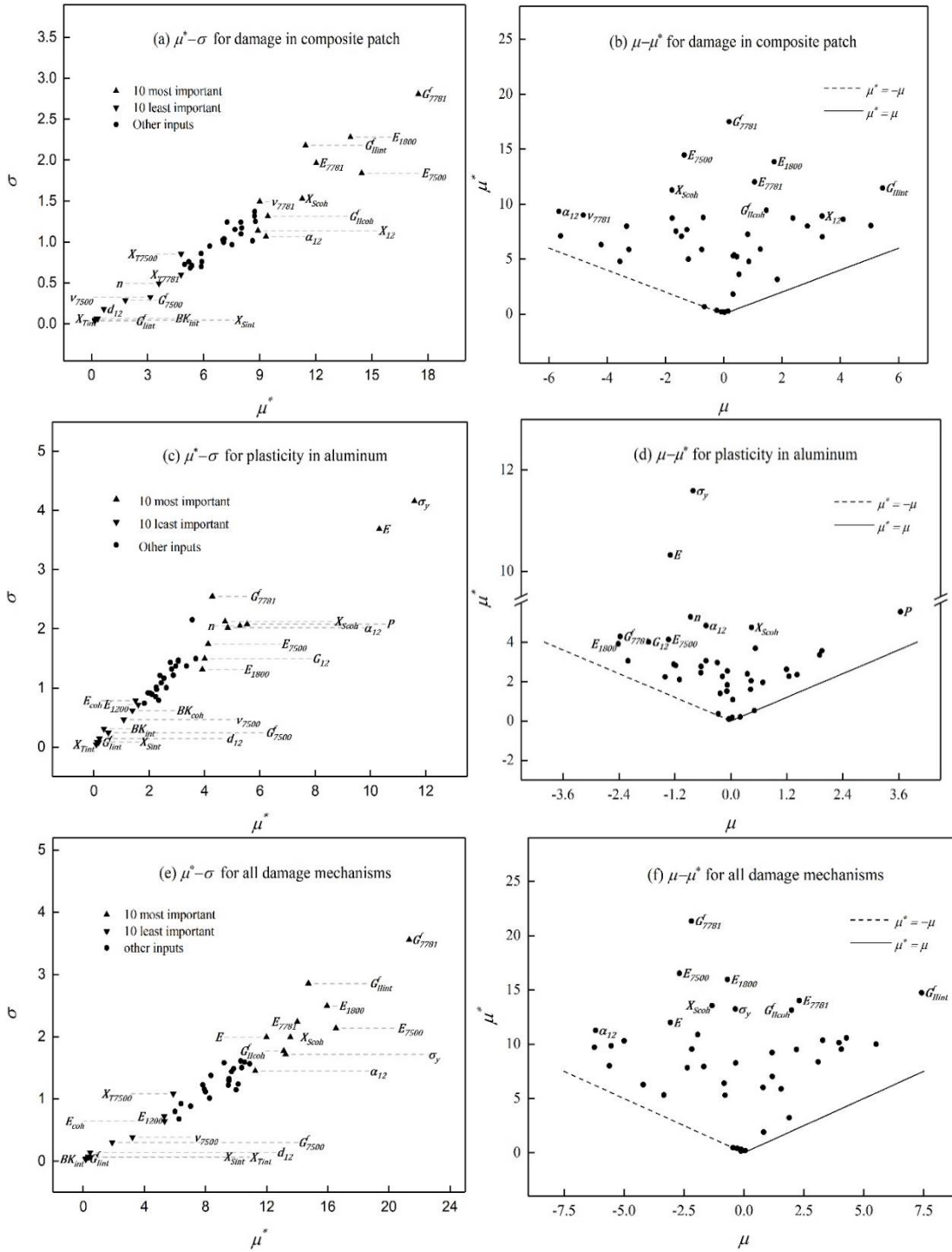


Figure 3. 11 The  $\mu^* - \sigma$  and  $\mu^* - \mu$  plot for the damage in the patch, aluminum and the whole structure.

Table 3. 3 The ten most influential parameters for different damage mechanisms

Damage mechanisms	Ten most influential parameters
Plasticity in laminae	$E_{1800}, E_{7500}, P, \alpha_{12}, G_{1800}^f, E_{7781}, X_{Scoh}, G_{7781}^f, X_{12}, \nu_{7781}$
Intralaminar fracture	$E_{1800}, E_{7781}, E_{7500}, X_{12}, G_{7781}^f, \nu_{7781}, G_{1800}^f, BK_{coh}, \nu, E_{1200}$
Delamination	$P, G_{7781}^f, X_{12}, X_{Scoh}, C, G_{12}, G_{IIint}^f, \varepsilon_{max}^{pl}, \nu, \nu_{7781}$
Disbond at interface	$E, \nu, \sigma_y, K, n, E_{1200}, \nu_{1200}, X_{T1200}, G_{1200}^f, E_{1800}$
Damage in composite patch	$G_{7781}^f, E_{7500}, E_{1800}, E_{7781}, G_{IIint}^f, X_{Scoh}, G_{IIcoh}^f, \alpha_{12}, \nu_{7781}, X_{12}$
Plasticity in aluminum	$\sigma_y, E, P, n, \alpha_{12}, X_{Scoh}, G_{7781}^f, E_{7500}, G_{12}, E_{1800}$
All damage mechanisms	$G_{7781}^f, E_{7500}, E_{1800}, E_{7781}, X_{Scoh}, G_{IIint}^f, \sigma_y, G_{IIcoh}^f, E, \alpha_{12}$



energy absorption in the laminae. As shown in in Fig. 3.11(f), the ten most important inputs for all the damage exhibit similar behavior of the sign of the effects as Fig. 3.11(b)(d). The consistency between the sensitivity information evaluated from separate components and the whole demonstrates the effectiveness of the EEM in consistently identifying the most influential parameters.

Next, the individual damage mechanisms within the patch are investigated. The  $\mu^* - \sigma$  plots of the energy absorption for each these damage mechanisms are presented in Fig. 3.12, and the ten most influential inputs on energy absorption are labeled on the plots. For plasticity and fracture in the laminae, the ten most influential inputs for both include the Young's modulus of the E-LT 1800, Hexcel 7500, and Hexcel 7781 layers ( $E_{1800}$ ,  $E_{7500}$ , and  $E_{7781}$ ) as shown in Fig. 3.12(a)(b), because most of the damage area of the patch is between the two loading pins and under pure bending. The tensile stress resulting from the pure bending is mainly distributed into the  $0^\circ/90^\circ$  layers. As depicted in Fig. 3.12(c), the delamination is affected by several laminae shear properties ( $P$ ,  $X_{12}$ ,  $C$  and  $G_{12}$ ) in addition to the interlaminar properties such as  $X_{Scoh}$ . This result is explained by the fact that the delamination is primarily a result of the shear stress transferred between different layers. According to Fig. 3.12(d), the Young's modulus and Poisson ratio of the aluminum ( $E$  and  $\nu$ ) and E-BX 1200 layers ( $E_{1200}$  and  $\nu_{1200}$ ) have a large effect on disbond. Similar to the

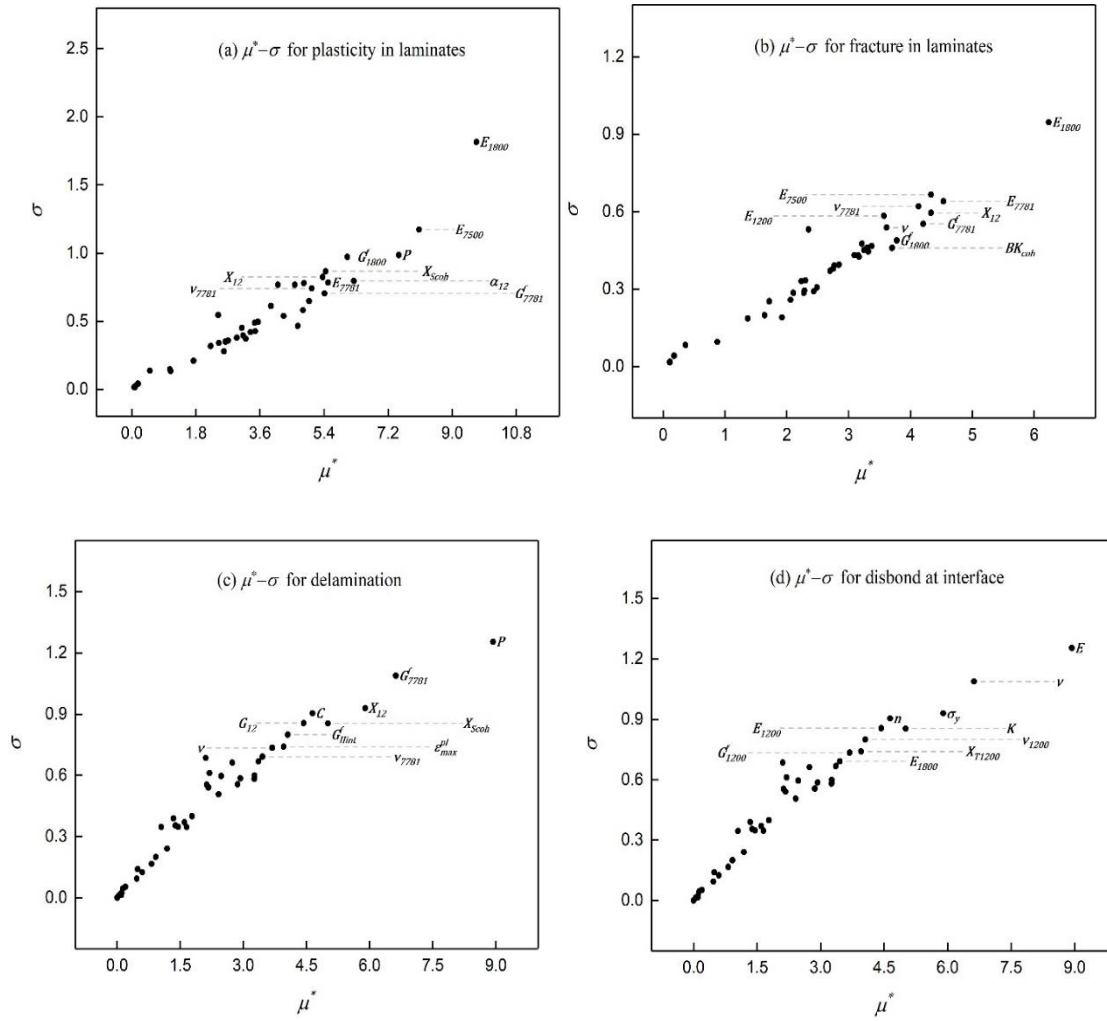


Figure 3. 12 The  $\mu^* - \sigma$  and  $\mu^* - \mu$  plot for the laminar plasticity, intralaminar fracture, delamination, and debond at the interface.

delamination, the disbond is caused by the shear fracture of the resin. As half of the laminae consist of E-BX 1200, it is not surprising that  $E_{1200}$  and  $\nu_{1200}$  of the laminae consist of E-BX 1200, it is not surprising that  $E_{1200}$  and  $\nu_{1200}$  significantly affect the overall shear behavior of the patch and consequently the disbond.

In addition to reducing the design space, the sensitivity analysis results can also be utilized to improve the FE model when compared with the data quality information. If influential parameters are from bad quality data, it reduces the confidence of the model. Full characterization of these parameters should be performed to enhance the performance of the model. As illustrated in Fig. 3.11, the ten most important inputs are all from good and neutral quality data. Regarding the data quality of influential parameters for individual damage mechanism in the composite patch, Fig. 3.12, shows each mechanism includes one bad quality input. The experimental characterization of those inputs is essential to allow a more precise simulation of corresponding damage, which is especially desirable for the nonvisible damage. For example,  $G_{1800}^f$  and  $G_{1200}^f$  were approximated from bad quality data and improving the data quality of such inputs could also potentially increase the model accuracy especially given the importance of shear properties on energy absorption of the patched structure.

### **3.4 Summary and Conclusion**

This study demonstrates an integrated approach (experimental testing, numerical modeling, and sensitivity analysis) to investigate and predict the damage tolerance in aluminum structure repaired with a co-cured composite patch. The four different testing specimen configurations designed in this study successfully initiate the potential damage mechanisms in the patched structure, including the intralaminar fracture, delamination, disbond at the interface, and failure in the metal. The validated high-fidelity 3D FE model is able to simulate the progressive damage in different failure modes. The FE simulation results show different loading conditions and initial damage locations initiate different damage mechanisms and affect their interactions in the patched structures. The sensitivity analysis using EEM is applied to one of the four-point bending specimens as an example to identify the most and least influential parameters for the optimization of the composite/metal hybrid structure with regard to the energy absorption. This knowledge can provide effective and practical guidelines to engineers when optimizing the design of patched structures. The sensitivity analysis results indicate that some of the parameter values estimated from neutral and bad quality data are important to the patch performance and may be affecting the predictive capability of the FE model. A full experimental characterization of those parameters should be included in future work to improve the FE model.

# CHAPTER IV    CRACK PROPAGATION IN PATCHED STRUCTURE

## 4.1 Introduction

The high strength aluminum alloy applied in marine structures suffers from cracking during the service life. The composite patch has been demonstrated as a promising repair method to restore the damage tolerance of the cracked marine structures. Many research work [3, 4, 9, 15, 93-100] studied the crack behavior of composite patch repaired aluminum. However, most of the investigations only consider pure Mode I fracture. There are a few papers looked at the mixed mode fracture caused by the mixed loading conditions. Besides the mixed loading conditions, mixed mode crack can be also initiated with purely Mode I far-field stresses. Prior research work [101, 102] shows the crack in aluminum alloy with high ductility might change the growing direction from the Mode I direction because of the effects of multiaxial stresses, high loads, microstructures and environmental effects.

This chapter presented proof and documentation of the mixed mode crack initiated by the Mode I far-field load stress in the eccentrically loaded single edge crack specimen (ESEC) of Al 5456 and the effect of the composite patch on the mixed mode crack behavior. The objectives of the ESEC fracture testing are to 1)

measure the load capability of the aluminum specimen with and without the composite patch repair, 2) observe the damage behavior of the aluminum specimen and the composite patch and document the observations.

## 4.2 Experimental Procedure

### 4.2.1 Materials

The aluminum alloy 5456 plate (from McMaster-Carr) used to fabricate the specimen has a thickness of 0.25 inch. The elastic-plastic properties of the alloy measured from tensile testing are summarized in Table 4.1, where the plastic behavior is described by the Ludwik-Hollomon hardening law as shown in Eq. 4.1,

$$\bar{\sigma} = A + C \bar{\epsilon}^n \quad (4.1)$$

where  $\bar{\sigma}$  is the equivalent plastic stress,  $\bar{\epsilon}$  is the equivalent plastic strain,  $A$ ,  $C$ ,  $n$  are material properties obtained via fitting the tested stress-strain curve. The strain rate and temperature effects have been neglected since both the tensile testing and fracture testing are quasi static processes with negligible temperature variation.

The epoxy resin (M1002) and the hardener (237) used to form the composite patch matrix and the bond line were from Pro-Set. The patch was reinforced by E-Glass fabric obtained from commercial sources, including the 8.8 oz/yd<sup>2</sup> Hexcel 7781 style 8 harness satin weave fabric, the 12 oz/yd<sup>2</sup> biaxial stitch

bonded  $\pm 45^\circ$  fabric, the 18 oz/yd<sup>2</sup> biaxial stitch bonded 0<sup>o</sup>/90<sup>o</sup> fabric and the 9.6 oz/yd<sup>2</sup> Hexel 7500 style plain weave fabric.

#### **4.2.2 Testing Specimens**

Both the unrepaired single edge crack specimens (Fig. 4.1) and the composite patch repaired single edge crack specimens (Fig. 4.2) were studied by fracture testing, with the aim to investigate the capacity of the composite patch in restoring damage tolerance of Al 5456 plate.

The specimens were fabricated from the 0.25-inch thick aluminum alloy 5456 plate. The specimens were cut in such a way where the initial notch of the specimen is perpendicular to the longitude direction on the aluminum plate. The initial notch of 0.06-inch width and 0.85-inch length was cut in the middle of the specimen edge by electrical discharge machining. Then a sharp fatigue pre-crack tip was generated by cyclic loading in a fatigue test machine. The maximum load was set as 400 lbf with a 10:1 tension-tension load amplitude ratio in the fatigue machine. The expected fatigue pre-crack was acquired running the cyclic loading for 2 hours with a load frequency of 5 Hz.

The patch was built on the unrepaired single edge crack specimens (Fig. 4.1) to make the composite patch repaired specimens (Fig. 4.2). Unlike the co-cure process where the composite patch and bond line are fabricated simultaneously onto a large Al plate followed by machining to obtain the

Table 4. 1 Elastic and plastic properties of Al5456 (provided by the United States Naval Academy)

$E / Psi$	$\sigma_Y / Psi$	$\nu$	$A$	$C$	$n$
1.0 E+07	2.2 E+04	0.3	2.2 E+04	7.2 E+04	0.34

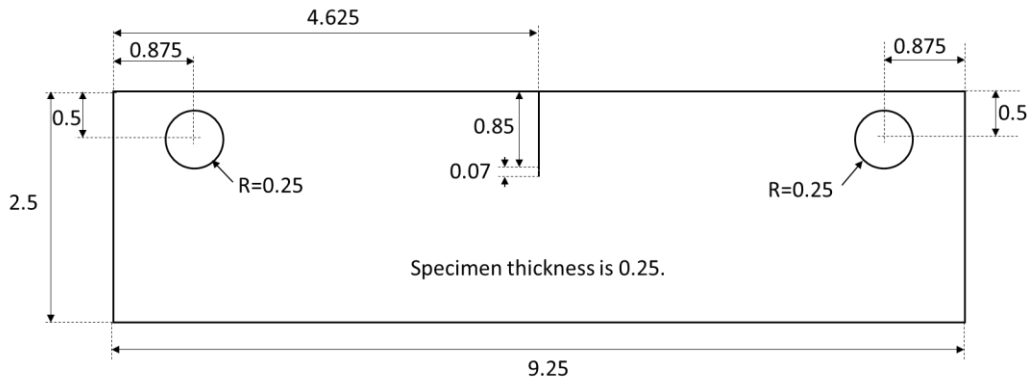


Figure 4. 1 Configuration of the eccentrically loaded single edge specimen, all in inches.

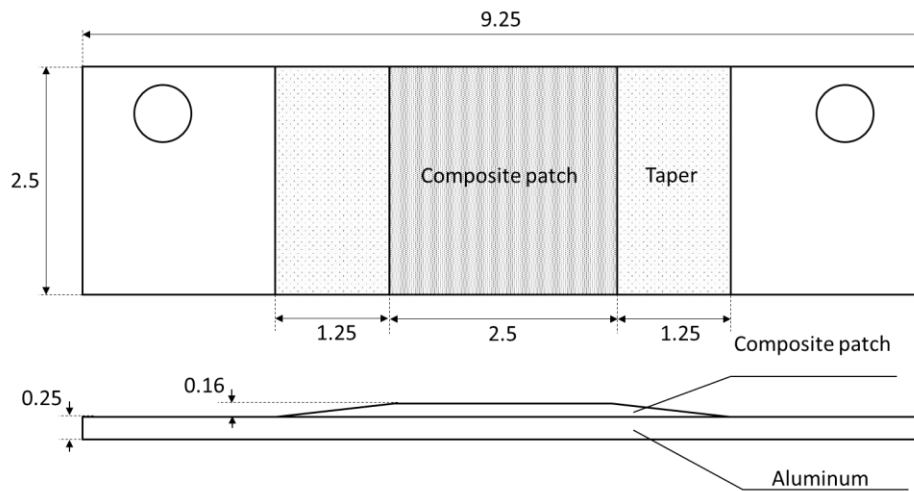


Figure 4. 2 Configuration of the eccentrically loaded single edge specimen repaired with the composite patch, all in inches.



specimen of the desired geometry, the preparation of the patch-repaired specimens was divided into two steps, where the composite laminate was first fabricated and then bonded to the aluminum plate specimen of specific geometry. This approach has the advantage of easy processing for Al plate of small size. In the first step, a quasi-isotropic E-glass/epoxy composite laminate (2.0 ft x 2.0 ft) was prepared by the vacuum-bagging method. Four different types of fabrics are stacked on a glass panel in the sequence given in Fig. 4.3. The 0°/90° fine harness stain weave ply Hexcel 7781 is used as the top ply to obtain a quality surface, and a layer of peel ply was placed after the bottom layer of the patch in order to achieve the same bond line mechanical properties between the patch and the aluminum plate as those prepared in the co-cure process. The epoxy resin (M1002) and the curing agent (M2046 hardener) was mixed in the ratio 4:1 by volume and spread onto the fabrics layer by layer during the hand layup process. The composite laminate was placed in the vacuum bag overnight under 23 inHg and then cured in the oven at 140° F for 4 hours. The setup of the vacuum bagging is illustrated in Fig. 4.4. The total thickness of the patch is 0.16 inch and the mechanical properties of the composite patch is shown in Table 4.2. Prior to bonding to the aluminum plate, the composite patch was cut by a water jet machine into small rectangular pieces (2.5 inch x 5 inch). Then the taper at both sides was machined to avoid large peeling strength, as shown in Fig. 4.2.

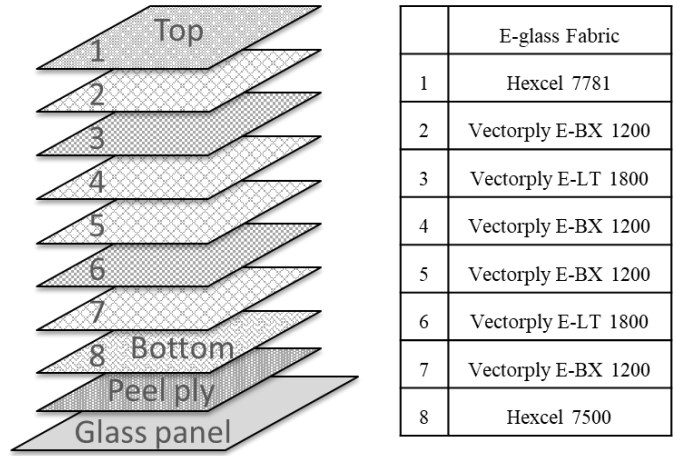


Figure 4. 3 Layup of the composite patch.

Table 4. 2 Mechanical properties of the E-glass/epoxy composite patch

$E_{11}$	1.7E+06	$G_{12}$	6.3E+05	$\nu_{12}$	0.27
$E_{22}$	1.7E+06	$G_{13}$	2.8E+05	$\nu_{13}$	0.25
$E_{33}$	7.7E+05	$G_{23}$	2.8E+05	$\nu_{23}$	0.25

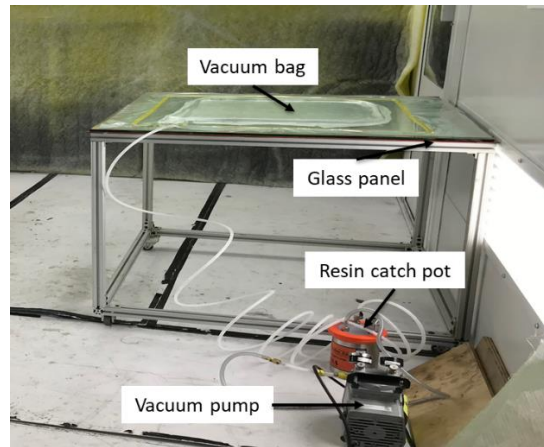


Figure 4. 4 The setup of the vacuum bagging system to fabricate the composite patch.

Before bonding the patch and the metal, the metal surface on the bonding side of the specimens was degreased with acetone, deoxidized with 180 grit sandpaper, and sprayed by the AC-130 solution. The epoxy (M1002) and hardener (M2046) again with the same mixing ratio (4:1 by volume) were used to bond the patch and aluminum. But the resin was mixed with extra glass beads with a 0.004-inch diameter to control the thickness of the bond line. 2 grams of the glass beads are used with every 3 oz. of mixed resin. The bonded specimens were covered with vacuum bag under 23 inHg in a 140° F oven for 4 hours to squeeze out the extra resin at the bond line and cure the resin.

#### **4.2.3 Testing Procedure**

The fracture test was performed on an MTS testing machine following the ASTM E1820 procedure, with the experimental setup shown in Fig. 4.5 and 4.6. The test was operated with displacement control under the loading rate of 0.04 inch per minute. The crack extension on the outside of the specimen was monitored by a high-resolution camera (Canon, EOS Rebel T5i with 18-55 mm lens), with the video recorded at 1920 X 1280 pixels.

### **4.3 Results and Discussions**

Six specimens were made and tested under the same conditions. Among the six repeating, the fatigue pre-crack in the unrepaired specimen was relatively straight and perpendicular to the loading direction (Fig. 4.7a). However, the

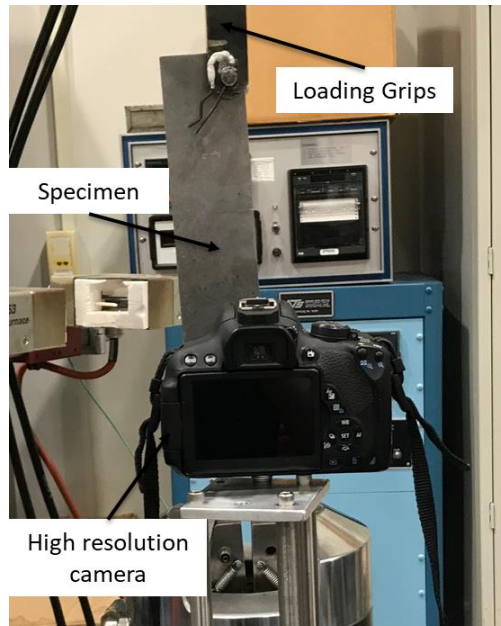


Figure 4. 5 The experimental setup for the cracking test of unrepaired specimen.

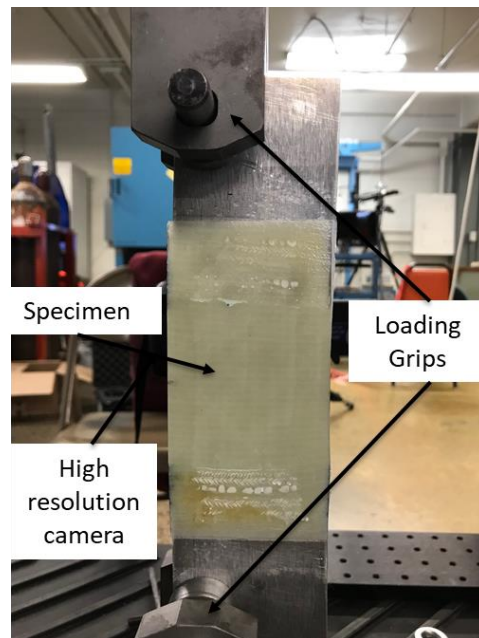


Figure 4. 6 The experimental setup for the cracking test of the unrepaired specimen.

severe material deformation results in intense shear strain in the plastic zone around the crack tip (Fig 4.7b), leading to the presence of shear band localization and the subsequent initiation of inclined crack (Fig. 4.7c). The mixed Mode I and II crack continue to propagate as a straight line along the direction of the initial inclined crack. The crack angle, defined as the angle between the crack line on the outside surface of the specimen and the fatigue pre-crack line, retains to be about  $135^\circ$  (Fig. 4.8) throughout the cracking process. The edge of the initial cutting slot has the same direction as the pre-fatigue crack and is easier to identify so that the edge is used to show the crack angle in Fig. 4.8.

Figure 4.9 shows the fracture surface of the crack in the unrepaired specimen. The pre-fatigue crack with a smooth fracture surface is followed by a flat to slant crack transition region. The flat crack surface was formed because of the high stress triaxiality in the interior of the specimen, and slant fracture surface was initiated because of the low stress triaxiality near the free surface. Then the crack propagated as a double slant crack all the way until the specimen fully failed.

The crack behavior in the repaired specimen is shown in Fig. 4.10. A sudden disbond with a large area at the bond line was observed during the test and no damage was found in the composite patch. There's no crack initiation detected right before the disbond as depicted in Fig. 4.10(a). Only a small plastic

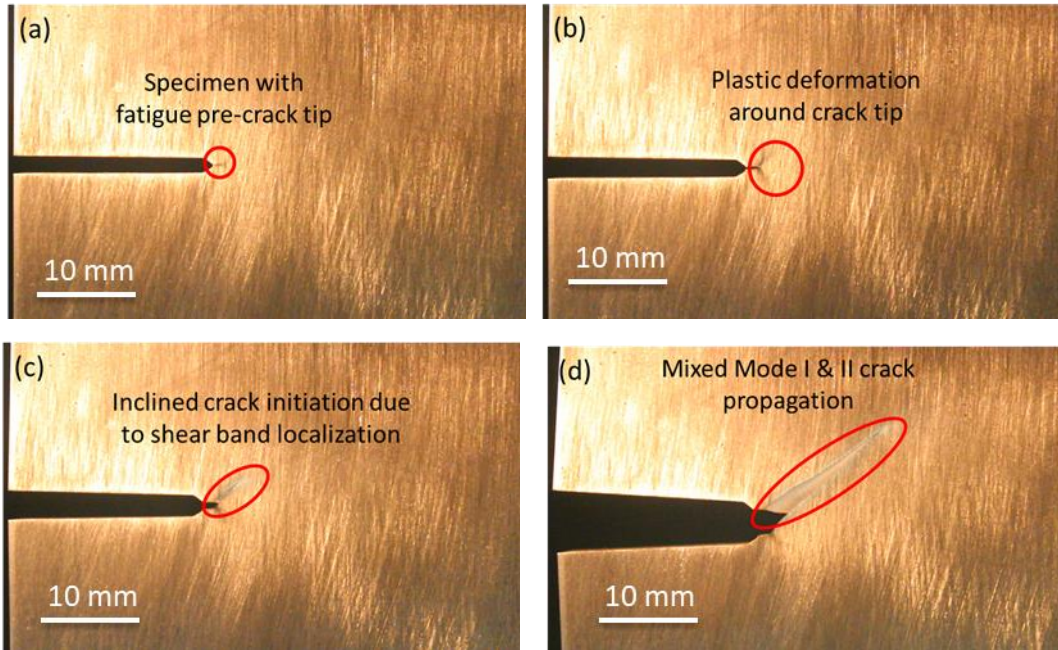


Figure 4. 7 Crack initiation and propagation of the single edge crack specimen

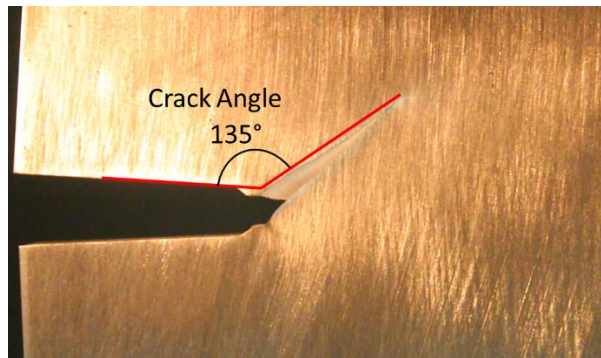


Figure 4. 8 The definition of the crack angle.

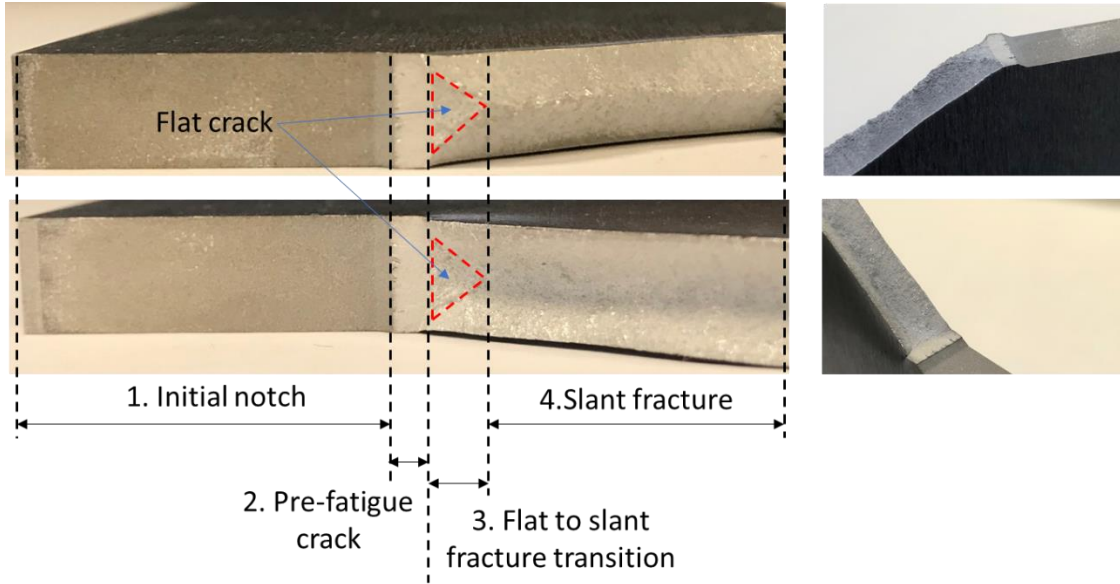


Figure 4. 9 Fracture surface of the unrepaired specimen.



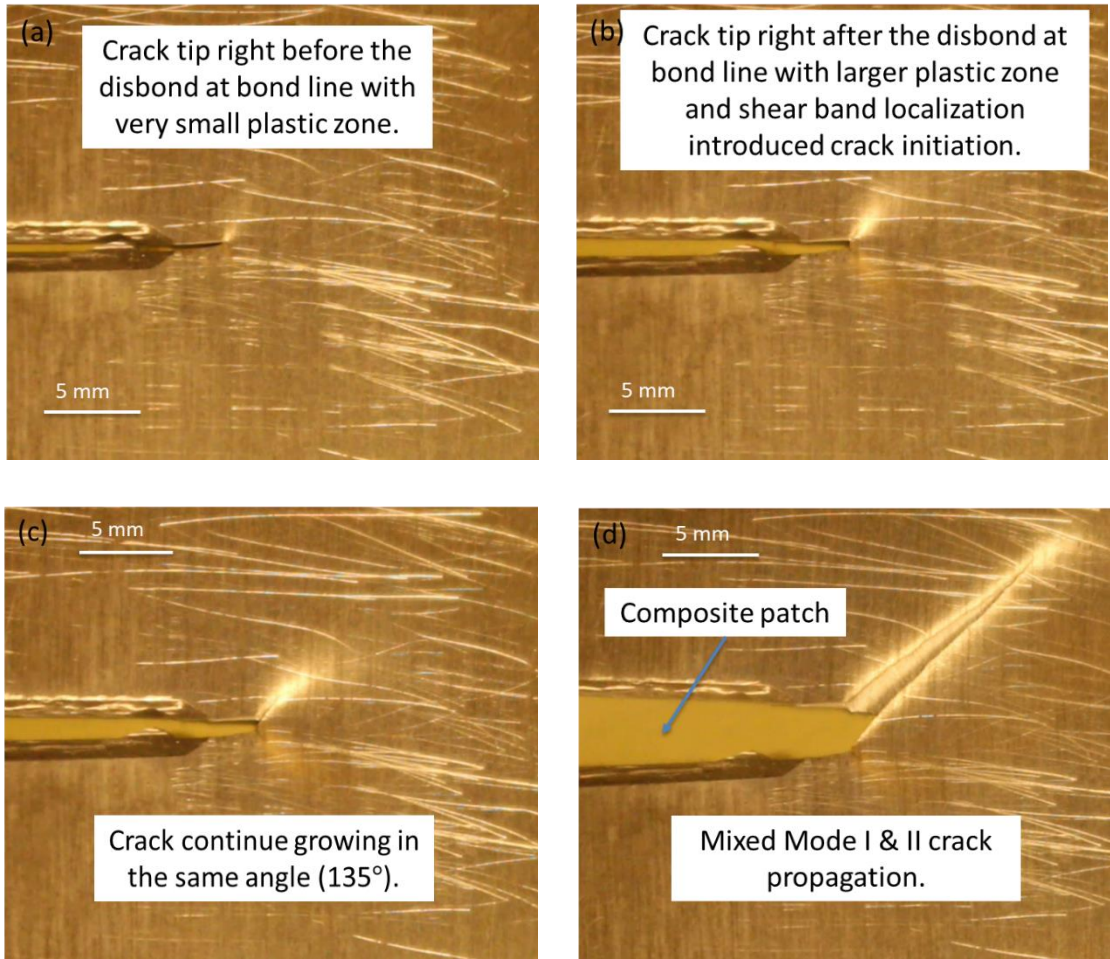


Figure 4. 10 Crack initiation and growth in composite patch repaired specimen.



zone appeared around the tip of the pre-fatigue crack. The sudden disbond of the bond line caused the detachment of half of the composite patch from the aluminum. Unlike the unrepaired specimen, the crack in the repaired specimen initiated immediately with a large crack opening, as shown in Fig. 4.11(b), instead of initiating and propagating gradually. The crack then propagated with the same crack angle as the unrepaired specimen, as illustrated in Fig. 4.10(d). The resin remains on the aluminum surface when the disbond happened, as shown in Fig. 4.12.

Figure 4.13 compares the load-displacement curve of the repaired specimen with that of the unrepaired specimen. The composite patch changes the maximum load of the specimen from 4900 lbf to 6300 lbf, with a 29% increase. The sudden drop of the load after the first peak load in the repaired specimen is caused by the large disbond of the bond line. Then the curve follows the same trend as that of the unrepaired specimen. The repaired specimen shows the same peak load after the disbond, which indicates the remaining patch bonded to the aluminum has an ignorable effect on the crack behavior of the specimen.

#### **4.4 Conclusions**

The fracture testing of the unrepaired ESEC specimen shows the initiation and growth of the localized shear band introduced mix mode crack under pure Mode I far-field stress. The repaired ESEC specimen demonstrated the ability of

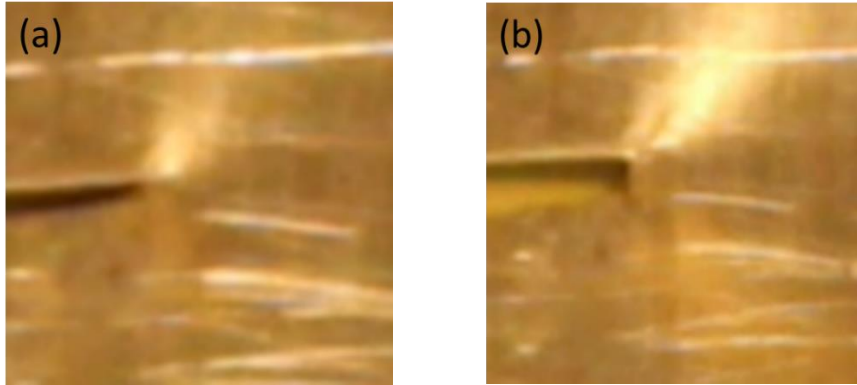


Figure 4. 11 Zoom in pictures of the crack tips in repaired specimen right before (a) and after (b) the disbond at the bond line.

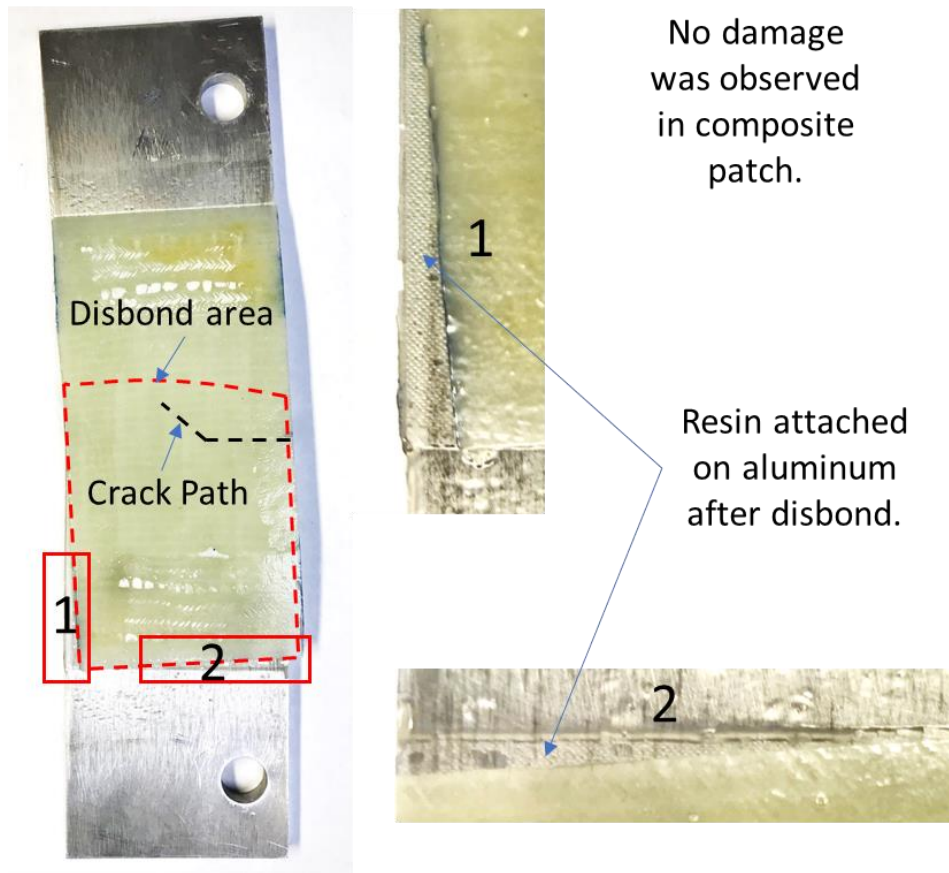


Figure 4. 12 The schematic diagram of the disbond area and the crack path.

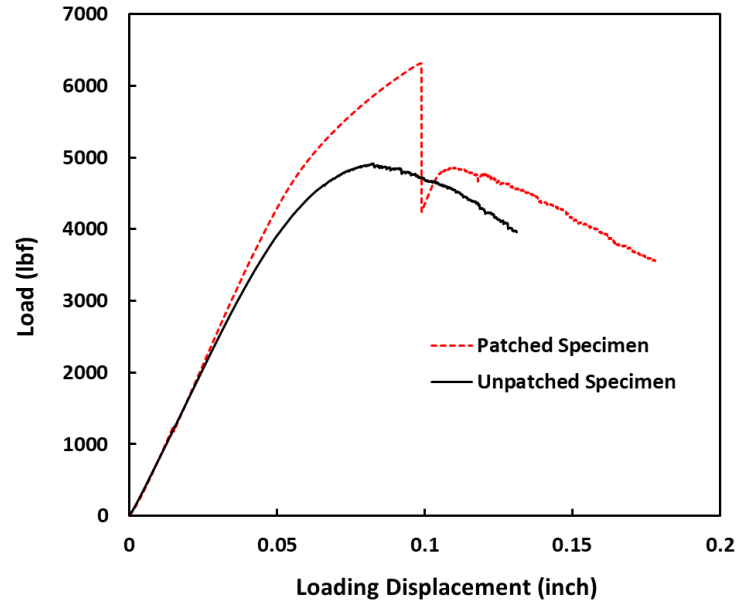


Figure 4. 13 Comparison of the load-displacement curves of patched and unpatched specimens.

the composite patch to retard the crack initiation and propagation. The bond line plays an important role in the performance of the composite patch on the ESEC specimen. Further investigation is required to identify the factors affecting the disbond.

## CHAPTER V CONCLUSIONS AND FUTURE WORK

### 5.1 Conclusions

This dissertation aims to study the damage behavior of composite patch repaired or reinforced the marine aluminum structure and provide practical guidelines to improve the design efficiency of the composite patch. All the damage modes and their interactions involved in the repaired structure are investigated, including the yielding and cracking in aluminum, fiber breakage, matrix cracking and delamination in the composite patch, and disbond of bond line.

Chapter II addresses an integrated approach that combines experimental testing, computational simulation, and sensitivity analysis to improve the accuracy and efficiency of the numerical prediction of crack propagation in engineering structures. This approach is demonstrated by compact tension testing of aluminum 5456 specimens with side grooves. The 2D and 3D cohesive theory based extended finite element methods are developed and the 3D model shows a more consistent prediction of crack behavior compared with the experimental observations. The surrogate model constructed from well sampled FE models is introduced to generate data for the sensitivity analysis to investigate the effects of uncertainties on crack growth. The variance-based (Sobol indices) results suggest the influences of the uncertainties might depend on the probability distribution of the uncertainties. This study shows that the

proposed integrated approach is promising to improve the engineering fracture design by determining the effects of uncertainties in crack prediction.

In Chapter III, an integrated framework is demonstrated to predict the damage tolerance of an aluminum plate repaired with a co-cured bonded quasi-isotropic E-glass/epoxy composite patch. The framework encompasses computational simulation, experimental testing, and sensitivity analysis to evaluate the damage tolerance of metal/composite structure and to identify the most influential design parameters on structural performance. To simulate the complex progressive damage in the repaired structure, a high fidelity three-dimensional finite element model is developed and validated using four-point bend testing under varying loading conditions to engage all potential damage mechanisms. A sensitivity study using the Elementary Effects method then identifies the most and least influential design properties on the energy absorption capability of the patched structure. The resulting investigation correlating the data quality of the numerical model input parameters with the sensitivity analysis results provides practical guidelines for model improvement and the design optimization of the patched structure. This study indicates that the shear plasticity of the composite patch is the most important contributor to damage tolerance under four-point bending.

Chapter IV investigated the shear band caused mixed mode crack in the Al 5456 ESEC specimen and the performance of the composite patch on

restoring the damage tolerance. The composite patch can significantly enhance the load capability of the cracked aluminum. The large disbond area results in the total failure of the patch and the repaired specimen show a similar crack behavior after the patch failure compared with the unrepaired specimen.

## **5.2 Future Work**

A couple of original works are presented in this dissertation on the damage analysis of composite patch repaired aluminum structures. Although many perceptive findings are achieved, certain limitations do exist, and the corresponding future work is discussed here.

1. Chapter II investigates the prediction of crack propagation in aluminum with a side-grooved Mode I CT specimen which significantly reduces the low stress triaxiality resulting from the free surface effect. However, the mixed mode fracture and the free surface effect do appear in the marine aluminum structure and can affect the crack behavior. The mixed mode fracture and the influence of the free surface effect can be studied to obtain a more comprehensive understanding of the prediction of the crack growth.
2. The four-point bending and fracture specimens are used to study the damage tolerance of patches structures in Chapter III and IV, respectively. The four-point bending specimen initiates all the potential damages in the composite patch without the cracking in aluminum. The

fracture specimen introduces the cracking in aluminum and disbond at bond line while does not engage the progressive damage in the composite patch. The composite patch used to repair the cracked aluminum structure can experience nonvisible damage during service under bending or impact loading. It is useful to design a specimen that can initiate both the crack in aluminum and the damage in the composite patch.

3. The bond line plays an important role in the performance of the composite patch. According to previous study, the mechanical properties highly depend on the microstructure such as the surface roughness of the bonded aluminum surfaces and the air voids in the resin. Peridynamics is an effective approach to investigate the bond line behavior at the micro level, especially the fracture behavior.



## **LIST OF REFERENCES**

1. Conner, B. "Aluminum and Shipbuilding-Advantages of Aluminum in Marine Application," 2008.
2. Lamb, T., Beavers, N., Ingram, T., and Schmieman, A. "The Benefits and Cost Impact of Aluminum Naval Ship Structure," *Journal of Ship Production and Design* Vol. 27, No. 1, 2011, pp. 35-49.
3. Grabovac, I., and Whittaker, D. "Application of bonded composites in the repair of ships structures—A 15-year service experience," *Composites Part A: Applied Science and Manufacturing* Vol. 40, No. 9, 2009, pp. 1381-1398.
4. Golumbfskie, W. J. "Aluminum Sensitization and the Navy." TMS Annual Meeting and Exhibition, 2014.
5. Schwarting, R., Ebel, G., and Dorsch, T. "Manufacturing techniques and process challenged with CG47 class ship aluminum superstructures modernization and repairs," *Fleet Maintenance & Modernization Symposium 2001: Assessing Current & Future Maintenance Strategies*. 2011, pp. P1-17.
6. Baker, A. "Repair of cracked or defective metallic aircraft components with advanced fibre composites—an overview of Australian work," *Composite Structures* Vol. 2, No. 2, 1984, pp. 153-181.
7. Baker, A. A. "A Proposed Approach for Certification of Bonded Composite Repairs to Flight-Critical Airframe Structure," *Applied Composite Materials* Vol. 18, No. 4, 2011, pp. 337-369.  
doi: 10.1007/s10443-010-9161-z
8. Baker, A. A., Rose, L. F., and Jones, R. "Advances in the bonded composite repair of metallic aircraft structure." Elsevier, 2003.
9. McGeorge, D., Echtermeyer, A., Leong, K., Melve, B., Robinson, M., and Fischer, K. "Repair of floating offshore units using bonded fibre composite materials," *Composites Part A: Applied science and manufacturing* Vol. 40, No. 9, 2009, pp. 1364-1380.
10. Khan, S., Sarang, S. K., and Hiratsuka, I. "Study of Bending Strength for Aluminum Reinforced with Epoxy Composite," 2016.  
doi: 10.4271/2016-01-0516
11. Kim, H. S., and Lee, D. G. "Optimal design of the press fit joint for a hybrid aluminum/composite drive shaft," *Composite Structures* Vol. 70, No. 1, 2005, pp. 33-47.  
doi: <http://dx.doi.org/10.1016/j.compstruct.2004.08.010>
12. Buyukozturk, O., Gunes, O., and Karaca, E. "Progress on understanding debonding problems in reinforced concrete and steel members

- strengthened using FRP composites," *Construction and Building Materials* Vol. 18, No. 1, 2004, pp. 9-19.
13. Zhao, X.-L., and Zhang, L. "State-of-the-art review on FRP strengthened steel structures," *Engineering Structures* Vol. 29, No. 8, 2007, pp. 1808-1823.
  14. Handbook–Airframe, A. M. T. "Vol. 1 (FAA-H-8083-31)," *US Department of Transportation, Federal Aviation Administration, 2012.*
  15. Weitzenboeck, J. R., and McGeorge, D. "A cold repair method for FPSOs," *Offshore Technology Conference*. Offshore Technology Conference, 2012.
  16. Mall, S., and Conley, D. "Modeling and validation of composite patch repair to cracked thick and thin metallic panels," *Composites Part A: Applied Science and Manufacturing* Vol. 40, No. 9, 2009, pp. 1331-1339.
  17. Bouiadjra, B. B., Belhouari, M., and Serier, B. "Computation of the stress intensity factors for repaired cracks with bonded composite patch in mode I and mixed mode," *Composite Structures* Vol. 56, No. 4, 2002, pp. 401-406.
  18. Chung, K. H., and Yang, W. H. "Mixed mode fatigue crack growth in aluminum plates with composite patches," *International journal of fatigue* Vol. 25, No. 4, 2003, pp. 325-333.
  19. Ouinas, D., Bachir Bouiadjra, B., Himouri, S., and Benderdouche, N. "Progressive edge cracked aluminium plate repaired with adhesively bonded composite patch under full width disbond," *Composites Part B: Engineering* Vol. 43, No. 2, 2012, pp. 805-811.  
doi: <http://dx.doi.org/10.1016/j.compositesb.2011.08.022>
  20. Bouiadjra, B. B., Ouinas, D., Serier, B., and Benderdouche, N. "Disbond effects on bonded boron/epoxy composite repair to aluminium plates," *Computational Materials Science* Vol. 42, No. 2, 2008, pp. 220-227.  
doi: <https://doi.org/10.1016/j.commatsci.2007.07.008>
  21. Benyahia, F., Aminallah, L., Albedah, A., Bachir Bouiadjra, B., and Achour, T. "Experimental and numerical analysis of bonded composite patch repair in aluminum alloy 7075 T6," *Materials & Design* Vol. 73, 2015, pp. 67-73.  
doi: <http://dx.doi.org/10.1016/j.matdes.2015.02.009>
  22. Ramji, M., Srilakshmi, R., and Bhanu Prakash, M. "Towards optimization of patch shape on the performance of bonded composite repair using FEM," *Composites Part B: Engineering* Vol. 45, No. 1, 2013, pp. 710-720.  
doi: <http://dx.doi.org/10.1016/j.compositesb.2012.07.049>

23. Bachir Bouiadjra, B., Fari Bouanani, M., Albedah, A., Benyahia, F., and Es-Saheb, M. "Comparison between rectangular and trapezoidal bonded composite repairs in aircraft structures: A numerical analysis," *Materials & Design* Vol. 32, No. 6, 2011, pp. 3161-3166.  
doi: <http://dx.doi.org/10.1016/j.matdes.2011.02.053>
24. Hosseini-Toudeshky, H., Mohammadi, B., Sadeghi, G., and Daghyani, H. "Numerical and experimental fatigue crack growth analysis in mode-I for repaired aluminum panels using composite material," *Composites Part A: applied science and manufacturing* Vol. 38, No. 4, 2007, pp. 1141-1148.
25. Saltelli, A., and Annoni, P. "How to avoid a perfunctory sensitivity analysis," *Environmental Modelling & Software* Vol. 25, No. 12, 2010, pp. 1508-1517.  
doi: <https://doi.org/10.1016/j.envsoft.2010.04.012>
26. Iooss, B., and Lemaître, P. "A review on global sensitivity analysis methods," *Uncertainty Management in Simulation-Optimization of Complex Systems*. Springer, 2015, pp. 101-122.
27. Saltelli, A., Annoni, P., Azzini, I., Campolongo, F., Ratto, M., and Tarantola, S. "Variance based sensitivity analysis of model output. Design and estimator for the total sensitivity index," *Computer Physics Communications* Vol. 181, No. 2, 2010, pp. 259-270.  
doi: <https://doi.org/10.1016/j.cpc.2009.09.018>
28. Garcia Sanchez, D., Lacarrière, B., Musy, M., and Bourges, B. "Application of sensitivity analysis in building energy simulations: Combining first- and second-order elementary effects methods," *Energy and Buildings* Vol. 68, 2014, pp. 741-750.  
doi: <https://doi.org/10.1016/j.enbuild.2012.08.048>
29. Ouinas, D., Bouiadjra, B. B., and Serier, B. "The effects of disbonds on the stress intensity factor of aluminium panels repaired using composite materials," *Composite Structures* Vol. 78, No. 2, 2007, pp. 278-284.  
doi: <http://dx.doi.org/10.1016/j.compstruct.2005.10.012>
30. Denney, J. J., and Mall, S. "Characterization of disbond effects on fatigue crack growth behavior in aluminum plate with bonded composite patch," *Engineering Fracture Mechanics* Vol. 57, No. 5, 1997, pp. 507-525.  
doi: [http://dx.doi.org/10.1016/S0013-7944\(97\)00050-7](http://dx.doi.org/10.1016/S0013-7944(97)00050-7)
31. Chang, F.-K., and Chang, K.-Y. "A progressive damage model for laminated composites containing stress concentrations," *Journal of composite materials* Vol. 21, No. 9, 1987, pp. 834-855.
32. Perugini, P., Riccio, A., and Scaramuzzino, F. "Three-dimensional progressive damage analysis of composite joints," *Proceedings of the eighth international conference on The application of artificial intelligence to*

- civil and structural engineering computing*. Civil-Comp Press, 2001, pp. 155-156.
33. Donadon, M. V., Iannucci, L., Falzon, B. G., Hodgkinson, J. M., and de Almeida, S. F. M. "A progressive failure model for composite laminates subjected to low velocity impact damage," *Computers & Structures* Vol. 86, No. 11, 2008, pp. 1232-1252.  
doi: <http://dx.doi.org/10.1016/j.compstruc.2007.11.004>
  34. Bednarczyk, B. A., Aboudi, J., and Arnold, S. M. "Micromechanics modeling of composites subjected to multiaxial progressive damage in the constituents," *AIAA Journal* Vol. 48, No. 7, 2010, pp. 1367-1378.
  35. Kashfuddoja, M., and Ramji, M. "An experimental and numerical investigation of progressive damage analysis in bonded patch repaired CFRP laminates," *Journal of Composite Materials* Vol. 49, No. 4, 2015, pp. 439-456.  
doi: 10.1177/0021998314521058
  36. Akterskaia, M., Jansen, E., and Rolfes, R. "Progressive Failure Analysis of Stiffened Composite Panels Using a Two-Way Loose Coupling Approach Including Intralaminar Failure and Debonding," *2018 AIAA/ASCE/AHS/ASC Structures, Structural Dynamics, and Materials Conference*. 2018, p. 0735.
  37. Sápi, Z., Butler, R., and Rhead, A. T. "Numerical Prediction of Failure in Composite T-Joints Using Progressive Damage Modelling," *2018 AIAA/ASCE/AHS/ASC Structures, Structural Dynamics, and Materials Conference*. 2018, p. 0221.
  38. Wang, C. H., Rose, L. R. F., and Callinan, R. "Analysis of out-of-plane bending in one-sided bonded repair," *International Journal of Solids and Structures* Vol. 35, No. 14, 1998, pp. 1653-1675.
  39. Lee, J., Cho, M., and Kim, H. S. "Bending analysis of a laminated composite patch considering the free-edge effect using a stress-based equivalent single-layer composite model," *International Journal of Mechanical Sciences* Vol. 53, No. 8, 2011, pp. 606-616.  
doi: <https://doi.org/10.1016/j.ijmecsci.2011.05.007>
  40. Clark, R. J., and Romilly, D. P. "Bending of bonded composite repairs for aluminum aircraft structures: A design study," *Journal of Aircraft* Vol. 44, No. 6, 2007, pp. 2012-2025.
  41. Goodmiller, G. R., and TerMaath, S. C. "Investigation of composite patch performance under low-velocity impact loading," *55th AIAA/ASMe/ASCE/AHS/SC Structures, Structural Dynamics, and Materials Conference*. 2014, p. 0692.

42. Jones, R., Chiu, W. K., and Smith, R. "Airworthiness of composite repairs: Failure mechanisms," *Engineering Failure Analysis* Vol. 2, No. 2, 1995, pp. 117-128.  
doi: [http://dx.doi.org/10.1016/1350-6307\(95\)00011-E](http://dx.doi.org/10.1016/1350-6307(95)00011-E)
43. Papanikos, P., Tserpes, K. I., Labeas, G., and Pantelakis, S. "Progressive damage modelling of bonded composite repairs," *Theoretical and Applied Fracture Mechanics* Vol. 43, No. 2, 2005, pp. 189-198.  
doi: <https://doi.org/10.1016/j.tafmec.2005.01.004>
44. Elices, M., Guinea, G. V., Gómez, J., and Planas, J. "The cohesive zone model: advantages, limitations and challenges," *Engineering Fracture Mechanics* Vol. 69, No. 2, 2002, pp. 137-163.  
doi: [http://dx.doi.org/10.1016/S0013-7944\(01\)00083-2](http://dx.doi.org/10.1016/S0013-7944(01)00083-2)
45. Roy, Y. A., and Dodds, R. H. "Simulation of ductile crack growth in thin aluminum panels using 3-D surface cohesive elements," *International Journal of Fracture* Vol. 110, No. 1, 2001, pp. 21-45.
46. Chen, C. R., Kolednik, O., Heerens, J., and Fischer, F. D. "Three-dimensional modeling of ductile crack growth: Cohesive zone parameters and crack tip triaxiality," *Engineering Fracture Mechanics* Vol. 72, No. 13, 2005, pp. 2072-2094.  
doi: <http://dx.doi.org/10.1016/j.engfracmech.2005.01.008>
47. Turon, A., Dávila, C. G., Camanho, P. P., and Costa, J. "An engineering solution for mesh size effects in the simulation of delamination using cohesive zone models," *Engineering Fracture Mechanics* Vol. 74, No. 10, 2007, pp. 1665-1682.  
doi: <http://dx.doi.org/10.1016/j.engfracmech.2006.08.025>
48. Moës, N., and Belytschko, T. "Extended finite element method for cohesive crack growth," *Engineering Fracture Mechanics* Vol. 69, No. 7, 2002, pp. 813-833.  
doi: [https://doi.org/10.1016/S0013-7944\(01\)00128-X](https://doi.org/10.1016/S0013-7944(01)00128-X)
49. Goangseup, Z., and Ted, B. "New crack-tip elements for XFEM and applications to cohesive cracks," *International Journal for Numerical Methods in Engineering* Vol. 57, No. 15, 2003, pp. 2221-2240.  
doi: [doi:10.1002/nme.849](https://doi.org/10.1002/nme.849)
50. Cox, J. V. "An extended finite element method with analytical enrichment for cohesive crack modeling," *International Journal for Numerical Methods in Engineering* Vol. 78, No. 1, 2009, pp. 48-83.
51. Khoei, A., and Bahmani, B. "Application of an enriched FEM technique in thermo-mechanical contact problems," *Computational Mechanics*, 2018, pp. 1-28.

52. Li, S., and Liu, W. K. "Meshfree and particle methods and their applications," *Applied Mechanics Reviews* Vol. 55, No. 1, 2002, pp. 1-34.  
doi: 10.1115/1.1431547
53. Silling, S. "-Dynamic fracture modeling with a meshfree peridynamic code," *Computational Fluid and Solid Mechanics 2003*. Elsevier, 2003, pp. 641-644.
54. Warren, T. L., Silling, S. A., Askari, A., Weckner, O., Epton, M. A., and Xu, J. "A non-ordinary state-based peridynamic method to model solid material deformation and fracture," *International Journal of Solids and Structures* Vol. 46, No. 5, 2009, pp. 1186-1195.
55. Ha, Y. D., and Bobaru, F. "Characteristics of dynamic brittle fracture captured with peridynamics," *Engineering Fracture Mechanics* Vol. 78, No. 6, 2011, pp. 1156-1168.
56. Sankararaman, S. "Significance, interpretation, and quantification of uncertainty in prognostics and remaining useful life prediction," *Mechanical Systems and Signal Processing* Vol. 52-53, 2015, pp. 228-247.  
doi: <https://doi.org/10.1016/j.ymssp.2014.05.029>
57. Wang, L., Wang, X., Su, H., and Lin, G. "Reliability estimation of fatigue crack growth prediction via limited measured data," *International Journal of Mechanical Sciences* Vol. 121, 2017, pp. 44-57.
58. Besterfield, G. H., Liu, W. K., Lawrence, M. A., and Belytschko, T. "Fatigue crack growth reliability by probabilistic finite elements," *Computer Methods in Applied Mechanics and Engineering* Vol. 86, No. 3, 1991, pp. 297-320.  
doi: [https://doi.org/10.1016/0045-7825\(91\)90225-U](https://doi.org/10.1016/0045-7825(91)90225-U)
59. Rahman, S. "Probabilistic fracture mechanics: J-estimation and finite element methods," *Engineering Fracture Mechanics* Vol. 68, No. 1, 2001, pp. 107-125.  
doi: [https://doi.org/10.1016/S0013-7944\(00\)00092-8](https://doi.org/10.1016/S0013-7944(00)00092-8)
60. Rahman, S., and Rao, B. N. "Probabilistic fracture mechanics by Galerkin meshless methods – part II: reliability analysis," *Computational Mechanics* Vol. 28, No. 5, 2002, pp. 365-374.  
doi: 10.1007/s00466-002-0300-8
61. Newman, J. C., Brot, A., and Matias, C. "Crack-growth calculations in 7075-T7351 aluminum alloy under various load spectra using an improved crack-closure model," *Engineering Fracture Mechanics* Vol. 71, No. 16, 2004, pp. 2347-2363.  
doi: <https://doi.org/10.1016/j.engfracmech.2004.01.004>

62. Pierce, S. G., Worden, K., and Bezazi, A. "Uncertainty analysis of a neural network used for fatigue lifetime prediction," *Mechanical Systems and Signal Processing* Vol. 22, No. 6, 2008, pp. 1395-1411.  
doi: <https://doi.org/10.1016/j.ymssp.2007.12.004>
63. Sankararaman, S., Ling, Y., and Mahadevan, S. "Uncertainty quantification and model validation of fatigue crack growth prediction," *Engineering Fracture Mechanics* Vol. 78, No. 7, 2011, pp. 1487-1504.  
doi: <https://doi.org/10.1016/j.engfracmech.2011.02.017>
64. Leonel, E. D., Chateaufneuf, A., and Venturini, W. S. "Probabilistic crack growth analyses using a boundary element model: applications in linear elastic fracture and fatigue problems," *Engineering Analysis with Boundary Elements* Vol. 36, No. 6, 2012, pp. 944-959.
65. Kikuchi, M., Atluri, S. N., and Miyamoto, H. "Studies on size effects and crack growth of side-grooved CT specimens," *Fracture Mechanics: Sixteenth Symposium*. ASTM International, 1985.
66. Shih, C., Lorenzi, H., and Andrews, W. "Elastic compliances and stress-intensity factors for side-grooved compact specimens," *International Journal of Fracture* Vol. 13, No. 4, 1977, pp. 544-548.
67. Delorenzi, H., and Shih, C. "3-D Elastic-plastic investigation of fracture parameters in side-grooved compact specimen," *International Journal of Fracture* Vol. 21, No. 3, 1983, pp. 195-220.
68. CEN, G. F. A. S.-S., Lucon, E., and Scibetta, M. "Influence of side-groove root radius on the ductile fracture toughness of miniature C (T) specimens," 2009.
69. Ono, H., Kasada, R., and Kimura, A. "Specimen size effects on fracture toughness of JLF-1 reduced-activation ferritic steel," *Journal of nuclear materials* Vol. 329, 2004, pp. 1117-1121.
70. Plaza, L. "The Determination of Uncertainties in Plane Strain Fracture Toughness (KIC) Testing," 2000.
71. İriç, S., and Ayhan, A. "Dependence of Fracture Toughness on Rolling Direction in Aluminium 7075 Alloys," *Acta Physica Polonica A* Vol. 132, No. 3, 2017, pp. 892-895.
72. Anderson, T. L., and Anderson, T. *Fracture mechanics: fundamentals and applications*: CRC press, 2005.



73. Saltelli, A., Ratto, M., Andres, T., Campolongo, F., Cariboni, J., Gatelli, D., Saisana, M., and Tarantola, S. *Global sensitivity analysis: the primer*. John Wiley & Sons, 2008.
74. Forrester, A., and Keane, A. *Engineering design via surrogate modelling: a practical guide*: John Wiley & Sons, 2008.
75. Gorissen, D., Couckuyt, I., Demeester, P., Dhaene, T., and Crombecq, K. "A surrogate modeling and adaptive sampling toolbox for computer based design," *Journal of Machine Learning Research* Vol. 11, No. Jul, 2010, pp. 2051-2055.
76. Koziel, S., and Yang, X.-S. *Computational optimization, methods and algorithms*: Springer, 2011.
77. Browne, M. W. "Cross-Validation Methods," *Journal of Mathematical Psychology* Vol. 44, No. 1, 2000, pp. 108-132.  
doi: <https://doi.org/10.1006/jmps.1999.1279>
78. Abaqus, V. "6.14 Documentation," *Dassault Systemes Simulia Corporation* Vol. 651, 2014.
79. Johnson, A. F. "Modelling fabric reinforced composites under impact loads," *Composites Part A: Applied Science and Manufacturing* Vol. 32, No. 9, 2001, pp. 1197-1206.  
doi: [http://dx.doi.org/10.1016/S1359-835X\(00\)00186-X](http://dx.doi.org/10.1016/S1359-835X(00)00186-X)
80. Johnson, A. F., Pickett, A. K., and Rozycki, P. "Computational methods for predicting impact damage in composite structures," *Composites Science and Technology* Vol. 61, No. 15, 2001, pp. 2183-2192.  
doi: [http://dx.doi.org/10.1016/S0266-3538\(01\)00111-7](http://dx.doi.org/10.1016/S0266-3538(01)00111-7)
81. Kleemola, H. J., and Nieminen, M. A. "On the strain-hardening parameters of metals," *Metallurgical Transactions* Vol. 5, No. 8, 1974, pp. 1863-1866.  
doi: 10.1007/bf02644152
82. Turon, A., Camanho, P. P., Costa, J., and Dávila, C. "A damage model for the simulation of delamination in advanced composites under variable-mode loading," *Mechanics of Materials* Vol. 38, No. 11, 2006, pp. 1072-1089.
83. Benzeggagh, M., and Kenane, M. "Measurement of mixed-mode delamination fracture toughness of unidirectional glass/epoxy composites with mixed-mode bending apparatus," *Composites science and technology* Vol. 56, No. 4, 1996, pp. 439-449.
84. Mandell, J. F., Wang, S.-S., and McGarry, F. J. "The extension of crack tip damage zones in fiber reinforced plastic laminates," *Journal of Composite Materials* Vol. 9, No. 3, 1975, pp. 266-287.

85. Hallett, S. R., and Wisnom, M. R. "Experimental investigation of progressive damage and the effect of layup in notched tensile tests," *Journal of Composite Materials* Vol. 40, No. 2, 2006, pp. 119-141.
86. Shields, M. D., and Zhang, J. "The generalization of Latin hypercube sampling," *Reliability Engineering & System Safety* Vol. 148, 2016, pp. 96-108.
87. Stein, M. "Large sample properties of simulations using Latin hypercube sampling," *Technometrics* Vol. 29, No. 2, 1987, pp. 143-151.
88. Morris, M. D. "Factorial Sampling Plans for Preliminary Computational Experiments," *Technometrics* Vol. 33, No. 2, 1991, pp. 161-174.  
doi: 10.1080/00401706.1991.10484804
89. Weigand, J. P., and TerMaath, S. C. "Sensitivity Analysis of Out-of-Plane Composite Lamina Properties Relative to Configuration and Constitutive Properties," *55th AIAA/ASME/ASCE/AHS/SC Structures, Structural Dynamics, and Materials Conference*. 2014, p. 1373.
90. Campolongo, F., Cariboni, J., and Saltelli, A. "An effective screening design for sensitivity analysis of large models," *Environmental Modelling & Software* Vol. 22, No. 10, 2007, pp. 1509-1518.  
doi: <https://doi.org/10.1016/j.envsoft.2006.10.004>
91. Campolongo, F., and Saltelli, A. "Sensitivity analysis of an environmental model: an application of different analysis methods," *Reliability Engineering & System Safety* Vol. 57, No. 1, 1997, pp. 49-69.
92. Saltelli, A., Tarantola, S., and Campolongo, F. "Sensitivity analysis as an ingredient of modeling," *Statistical Science* Vol. 15, No. 4, 2000, pp. 377-395.
93. Allan, R., Bird, J., and Clarke, J. "Use of adhesives in repair of cracks in ship structures," *Materials Science and Technology* Vol. 4, No. 10, 1988, pp. 853-859.
94. Grabovac, I., Bartholomeusz, R., and Baker, A. "Composite reinforcement of a ship superstructure—project overview," *Composites* Vol. 24, No. 6, 1993, pp. 501-509.
95. Grabovac, I. "Bonded composite solution to ship reinforcement," *Composites Part A: Applied Science and Manufacturing* Vol. 34, No. 9, 2003, pp. 847-854.

96. Grabovac, I. "Composite Reinforcement for Naval Ships: Concept Design, Analysis and Demonstration," 2005.
97. Turton, T., Dalzel-Job, J., and Livingstone, F. "Oil platforms, destroyers and frigates—case studies of QinetiQ's marine composite patch repairs," *Composites Part A: Applied Science and Manufacturing* Vol. 36, No. 8, 2005, pp. 1066-1072.
98. Avgoulas, E., Karatzas, V., Zilakos, I., and Tsouvalis, N. "Numerical analysis of cracked marine structures repaired with composite patches," *Tree Biotechnology*, 2014, p. 367.
99. Karatzas, V. A., Kotsidis, E. A., and Tsouvalis, N. G. "Experimental Fatigue Study of Composite Patch Repaired Steel Plates with Cracks," *Applied Composite Materials* Vol. 22, No. 5, 2015, pp. 507-523.
100. Kwon, Y., and Hall, B. "Analyses of cracks in thick stiffened plates repaired with single-sided composite patch," *Composite Structures* Vol. 119, 2015, pp. 727-737.
101. Meggiolaro, M. A., Miranda, A. C. O., Castro, J. T. P., and Martha, L. F. "Stress intensity factor equations for branched crack growth," *Engineering Fracture Mechanics* Vol. 72, No. 17, 2005, pp. 2647-2671.  
doi: <https://doi.org/10.1016/j.engfracmech.2005.05.004>
102. Zhang, W., and Cai, L. "In-situ SEM and optical microscopy testing for investigation of fatigue crack growth mechanism under overload," *MATEC Web of Conferences*. Vol. 165, EDP Sciences, 2018, p. 13013.

## VITA

Bozhi Heng comes from Jiangsu, China. He received his bachelor's degree in aircraft design and engineering in 2012, and his master's degree in engineering mechanics in 2015 from Nanjing University of Aeronautics and Astronautics, China. He joined the computational mechanics group at University of Tennessee, Knoxville to pursue his Ph.D. degree in August 2015. His Ph.D. research work include structural mechanics, fracture mechanics, finite element methods, peridynamics and sensitivity analysis.